Simulation of the Backplane Response of Composite Helmet Materials Under Ballistic Impact

A report prepared for

Defence Research Establishment Valcartier

and

Biokinetics and Associates Ltd.

by

J. van Hoof, M.J. Worswick, P.V. Straznicky

Department of Mechanical and Aerospace Engineering

Carleton University, Ottawa, Canada

October 25, 1999

submitted to
Dr. Kevin Williams
Defence Research Establishment Valcartier (DREV)
2459 Pie-XI Blvd. North, Val-Belair, Quebec, Canada

Contract Serial No.: W7701-5-1203/001/XSK

Preface

This report summarises the findings obtained during the DREV-funded project entitled "Exploration of the Response of the Helmeted Head to Ballistic Impact", contract number W7701-5-1203/01-XSK. This project concerns the numerical simulation of a generic protective helmet subjected to ballistic impact. The goals of this project are to develop accurate models of the penetration process and the subsequent delaminated backplane motion.

Abstract

Even though delamination is generally acknowledged as one of the main damage mechanisms in ballistically impacted laminates, information on the evolution of delaminations under ballistic conditions is scarce. The research presented in this report focuses on the deformation response of materials used in ballistic helmets, for which the impact of the delaminated backplane with the head is considered to be a possible cause of skull fracture and underlying brain damage.

A numerical model was developed as part of this research to gain insight into the parameters governing the penetration and deformation response of laminated composites subjected to ballistic impact. The effects of the various model parameters on the predicted ballistic response were evaluated extensively. Both instantaneous and post-failure approaches were used. It was found that the use of a post-failure approach led to a more realistic and numerically more stable response than when an instantaneous failure model was used. The through-thickness shear properties used in the numerical model were found to have a large effect on the predicted ballistic response.

102-00861/

A number of ballistic impact tests on woven laminated Kevlar-29 composite panels were performed to evaluate the accuracy and limitations of the numerical model. Different types of projectiles with a range of impact velocities were used. The initial quasi-static material properties for the numerical model, obtained from the literature, were "calibrated" for one specific impact condition to obtain close agreement between simulations and measurements. The "calibrated" numerical material properties were then held constant in simulations of the other ballistic impact tests.

For the panels impacted by the four types of projectiles considered in this study, the model predicted the measured maximum backplane displacement accurately. Comparing the measured and predicted responses for all projectiles used in this study, it was found that the maximum backplane displacement increased nearly linearly with increased impact energy, at least within the range of impact energies used in this research.

Contents

1 Introduction 1

1.1 Motivation 1

1.2 Objective and Strategy 3

1.3 Penetration Mechanisms 5

1.4 Delamination Mechanisms 8

1.4.1 Drop Weight Impact 8

1.4.2 Ballistic Impact 14

1.5 Delamination Initiation and Growth Criteria 17

1.5.1 Strength of Materials Approach 17

1.5.2 Fracture Mechanics Approach 22

1.5.3 Continuum Damage Mechanics Approach 28

1.6 Numerical Modelling of Delamination 40

1.6.1 Delamination Initiation 40

1.6.2 Delamination Growth 40

1.7 Outline 44

2 Numerical Model 46

2.1 Constitutive Model 47

2.2 Intralaminar Failure 48

2.2.1 Instantaneous Failure Model 48

2.2.2 Post-Failure Model 50

2.3 Interlaminar Failure 54

2.3.1 Discrete Delamination Interface 54

2.4 Model Description 57

2.5 Material Properties 61

2.5.1 Kevlar laminates 61

2.5.2 Projectiles 65

2.6 Effects of Model Parameters on the Ballistic Response of the Panel Model 66

2.6.1 Instantaneous vs. Post-Failure Model Response 66

2.6.2 Effect of Material Parameters 70

2.6.3 Effect of Damage Parameters 79

2.6.4 Effect of Hourglass Control 85

2.6.5 Mesh Sensitivity 89

2.7 Summary of Findings 94

3 Ballistic Impact Testing 95

3.1 Experimental Set-up 95

3.2 Measurement Techniques 97

3.2.1 ELVS Measuring System 97

3.2.2 IMAX System 99
3.2.3 VISAR System 99
3.3 TNO Series 100
3.3.1 1.1 g FSP 102
3.3.2 2.8 g FSP 106
3.4 UBC Series 110
3.4.1 Flat-Nose Cylindro-Conical Projectiles 111
3.4.2 Sharp-Nose Cylindro-Conical Projectiles 116

4 Simulation of Ballistic Impact Tests **119**
4.1 Model Description 119
4.1.1 Mesh 119
4.1.2 Material Properties 122
4.2 Simulation of TNO Series 124
4.2.1 1.1 g FSP 124
4.2.2 2.8 g FSP 129
4.3 Simulation of UBC Series 134
4.3.1 Flat-Nose Projectiles 134
4.3.2 Sharp-Nose Projectiles 143

5 Discussion **149**
5.1 Numerical Parameters 150
5.2 Simulation of Ballistic Impact Tests 151
5.3 Trends in Measurements and Predictions 152
5.4 Current Limitations of the Model 156

6 Conclusions 158

7 Recommendations 160

References 163

Appendices 178

A TNO Series IMAX Images 178

A.1 1.1 g FSP 178

A.2 2.8 g FSP 179

List of Tables

2.1 Elastic properties for Kevlar fibres 62

2.2 Elastic properties for woven Kevlar laminates 63

2.3 Strength properties for woven Kevlar laminates 64

2.4 Elastic properties adopted for woven Kevlar in numerical model . . . 64

2.5 Strength properties adopted for woven Kevlar in numerical model . . 65

2.6 Material properties adopted for projectiles 65

2.7 Effects of mesh definition on simulation 90

3.1 Summary of TNO Series 101

3.2 Summary of UBC Series 110

4.1 Elastic properties adopted for woven Kevlar in numerical model . . . 123

4.2 Strength properties adopted for woven Kevlar in numerical model . . 123

5.1 Projectile Characteristics 153

List of Figures

1.1 Penetration damage mechanisms and order in which they occur during penetration process as proposed by Langlie and Cheng (1989). . . 5

1.2 Typical matrix cracking and delamination damage in an impacted composite laminate (Fuoss, 1996). 10

1.3 Staircase delamination pattern through bottom 12 plies of a $[-45/0/45/90]_{3s}$ laminate. The impacted surface is at ply 1 (Gosse and Mori, 1988). . 11

1.4 Typical shape of delamination damage at an interface of an impacted composite laminate (Fuoss, 1996). 12

1.5 Delamination mechanism in ballistically impacted laminates as proposed by Zhu *et al.* (1992a). 15

1.6 Short-Beam Shear test set-up (ASTM D 2344-84, 1997). 21

1.7 Interlaminar fracture modes. 23

1.8 Double Cantilever Beam specimen (ASTM D 5528-94a, 1997). 25

1.9 End Notch Flexure specimen (Martin, 1996). 26

1.10 Mixed Mode Bending test specimen (Martin, 1996). 27

1.11 Progressive damage represented by decreasing unloading stiffness. . . 37

1.12 Effect of damage exponent m on post-failure behaviour. 37

1.13 Laminate modelled at meso-scale as stacking of layers connected by interfaces Daudeville *et al.* (1995). 38
1.14 Interface coordinate system (Daudeville *et al.*, 1995). 39
1.15 Finite element crack growth model (Majeed, 1995). 42

2.1 Penalty method visualised by interface springs between contacting nodes and element faces. 54
2.2 Finite element model of the woven Kevlar-29 laminated panel 58
2.3 .22 calibre FSP dimensions (inches) 59
2.4 .22 calibre FSP finite element mesh 59
2.5 .30 calibre FSP dimensions (inches) 59
2.6 .30 calibre FSP finite element mesh 59
2.7 Cylindro-conical projectile dimensions (mm) 60
2.8 Cylindro-conical projectile finite element meshes 60
2.9 Sequence of deformed mesh plots using the instantaneous failure model. 67
2.10 Sequence of deformed mesh plots using the post-failure model with the standard material properties. 68
2.11 Differences in response between instantaneous and post-failure models. 69
2.12 Comparison between the instantaneous and post-failure model of the effects of the in-plane tensile stiffnesses. 70
2.13 Comparison between the instantaneous and post-failure model of the effects of the in-plane strength properties. 71
2.14 Comparison between the instantaneous and post-failure model of the combined effects of the in-plane stiffness and strength properties. . . . 72

2.15 Comparison between the instantaneous and post-failure model of the effects of the through-thickness compression stiffness. 73
2.16 Comparison between the instantaneous and post-failure model of the effects of the through-thickness shear stiffness. 74
2.17 Comparison between the instantaneous and post-failure model of the effects of the through-thickness compression strength. 75
2.18 Comparison between the instantaneous and post-failure model of the effects of the through-thickness shear strengths. 76
2.19 Comparison between the instantaneous and post-failure model of the combined effects of the through-thickness compression stiffness and strength. 77
2.20 Comparison between the instantaneous and post-failure model of the combined effects of the through-thickness shear stiffness and strength. 78
2.21 Effects of the damage exponents m_i for the instantaneous failure model. 79
2.22 Effects of the damage exponents m_i for the post-failure model. 80
2.23 Effects of the delamination strength for the instantaneous failure model. 81
2.24 Effects of the delamination strength for the post-failure model. 82
2.25 Effects of the discrete delamination release mechanism for the instantaneous failure model. 83
2.26 Effects of the discrete delamination release mechanism for the post-failure model. 84
2.27 Element definition. 85
2.28 Comparison between the instantaneous and post-failure model of the effects of the stiffness hourglassing control. 88

2.29 Effects of the through-thickness mesh definition for the instantaneous failure model. 91
2.30 Effects of the through-thickness mesh definition for the post-failure model. 92
2.31 Effects of the in-plane mesh definition for the instantaneous failure model. 93
2.32 Effects of the in-plane mesh definition for the post-failure model. . . . 94

3.1 Target support fixture (dimensions in mm). 96
3.2 ELVS schematic (Cepuš *et al.*, 1999). 98
3.3 IMAX image of a Kevlar panel impacted by a 1.1 g FSP at 586 m/s. . 102
3.4 Measured backplane response of Kevlar panels impacted by 1.1 g FSPs.103
3.5 Maximum backplane displacement versus impact velocities for Kevlar panels impacted by 1.1 g FSPs. 104
3.6 Pictures of Kevlar panel after being impacted by a 1.1 g FSP at 586 m/s.105
3.7 IMAX image of a Kevlar panel impacted by a 2.8 g FSP at 511 m/s. . 106
3.8 Measured backplane response of Kevlar panels impacted by 2.8 g FSPs.107
3.9 Maximum backplane displacement versus impact velocities for Kevlar panels impacted by 2.8 g FSPs. 108
3.10 Pictures of Kevlar panel after being impacted by a 2.8 g FSP at 511 m/s.109
3.11 Measured response of flat-nose cylindro-conical projectiles impacting Kevlar panels: perforating shots. 112
3.12 Measured response of flat-nose cylindro-conical projectiles impacting Kevlar panels: non-perforating shots. 114

3.13 Pictures of Kevlar panel after being impacted by a flat-nose cylindro-conical projectile at 251 m/s. 115

3.14 Measured response of sharp-nose cylindro-conical projectiles impacting Kevlar panels: perforating shots. 117

3.15 Pictures of Kevlar panel after being impacted by a sharp-nose cylindro-conical projectile at 236 m/s. 118

4.1 Finite element model of woven Kevlar-29 laminated panel used in simulations of UBC and TNO series. 120

4.2 Close-up of the impact area and FSPs used in simulations of the TNO series. 121

4.3 Close-up of the impact area and FSPs used in simulations of the UBC series. 121

4.4 Sequence of deformed mesh plots of a 1.1 g FSP impacting a Kevlar panel at 586 m/s. 125

4.5 Simulated and measured backplane displacement-time histories for Kevlar panels impacted by a 1.1 g FSPs. 127

4.6 Simulated and measured maximum backplane displacement versus impact velocities for Kevlar panels impacted by 1.1 g FSPs. 128

4.7 Sequence of deformed mesh plots of a 2.8 g FSP impacting a Kevlar panel at 511 m/s. 130

4.8 Simulated and measured backplane displacement-time histories for Kevlar panels impacted by 2.8 g FSPs. 132

4.9 Simulated and measured maximum backplane displacement versus impact velocities for Kevlar panels impacted by 2.8 g FSPs. 133

4.10 Simulated and measured response of flat-nose cylindro-conical projectiles impacting Kevlar panels: perforating shots. 135

4.11 Simulated and measured exit velocities versus impact velocities for flat-nose cylindro-conical projectiles impacting Kevlar panels. 136

4.12 Sequence of deformed mesh plots for a flat-nose cylindro-conical projectile impacting a Kevlar panel at 251 m/s. 138

4.13 Simulated and measured response of flat-nose cylindro-conical projectiles impacting Kevlar panels: non-perforating shots. 140

4.14 Simulated and measured response of flat-nose cylindro-conical projectiles impacting Kevlar panels: non-perforating shots. 141

4.15 Predicted maximum backplane displacement versus impact velocity for flat-nose cylindro-conical projectiles impacting Kevlar panels. . . . 142

4.16 Simulated and measured response of sharp-nose cylindro-conical projectiles impacting Kevlar panels: perforating shots. 144

4.17 Simulated and measured exit velocities versus impact velocities for sharp-nose cylindro-conical projectiles impacting Kevlar panels. . . . 145

4.18 Sequence of deformed mesh plots from the simulation of a sharp-nose cylindro-conical projectile impacting a Kevlar panel at 155 m/s. . . . 147

4.19 Simulated and measured response of sharp-nose cylindro-conical projectiles impacting Kevlar panels: non-perforating shots. 148

5.1 Measured and predicted maximum backplane displacement as function of incident energy for a range of projectiles. 153

7.1 Helmet model developed at Carleton University together with ESI Head Model. 162

A.1 IMAX image of a Kevlar panel impacted by a 1.1 g FSP at 560 m/s. . 178

A.2 IMAX image of a Kevlar panel impacted by a 1.1 g FSP at 545 m/s. . 179

A.3 IMAX image of a Kevlar panel impacted by a 1.1 g FSP at 4835 m/s. 179

A.4 IMAX image of a Kevlar panel impacted by a 2.8 g FSP at 461 m/s. . 180

A.5 IMAX image of a Kevlar panel impacted by a 2.8 g FSP at 446 m/s. . 180

A.6 IMAX image of a Kevlar panel impacted by a 2.8 g FSP at 398 m/s. . 181

A.7 IMAX image of a Kevlar panel impacted by a 2.8 g FSP at 386 m/s. . 181

A.8 IMAX image of a Kevlar panel impacted by a 2.8 g FSP at 321 m/s. . 182

Nomenclature

angle-ply	laminae are oriented at $+\theta$ and $-\theta$ from each other
areal density	weight per unit area
ballistic limit	critical level of projectile impact velocity or kinetic energy below which no target perforation occurs
delamination	separation of individual plies which constitute a laminate
denier	weight in grams of 9000 meters of textile strand
interply layer	thin layer of matrix material between each ply
meso-scale	scale at which constitutive equations are written; order of 1 mm^3 for composites
self-similar	scale invariant
tenacity	breaking strength (grams) divided by denier of strand
V_{50}	projectile impact velocity for which 50 % of targets are perforated

Chapter 1

Introduction

1.1 Motivation

Fibre-reinforced laminate composite materials are increasingly used in a wide range of applications due to their low weight, high specific strength, and tailorability. One of the restrictions of wider application of laminated composites is their complex failure process: various damage modes can occur and these modes often interact, leading to ultimate failure. It is therefore of great importance that the damage modes of laminated composites and the ramifications of their existence in a structure are understood in order to be accounted for in the design.

Damage modes in impacted laminates include fibre failure, matrix cracking, punching failure, and delamination. Of these modes, delamination is generally acknowledged as the most predominant and most severe damage mode (Sela and Ishai, 1989; Whitney, 1989; Wang *et al.*, 1995; Martin, 1996). Delamination is the separation of the individual plies which constitute a laminated composite structure. Separation occurs in a thin layer of matrix material which exists between each ply

and is referred to as the interply layer (O'Brien, 1982).

The resistance against the initiation and growth of delaminations is generally low (Briscoe and Williams, 1993). In addition, delaminations have been found to reduce the failure stress of composite laminates to well below that predicted by in-plane failure criteria (Gosse and Mori, 1988; Sela and Ishai, 1989; Lagace and Bhat, 1993; Poon *et al.*, 1993; Hung *et al.*, 1995). Delaminations can initiate and grow due to a variety of loading conditions (Poon *et al.*, 1993; Bolotin, 1996). This report focuses on delaminations induced by impact loading, since the main emphasis of the presented work was on the ballistic impact response of laminated composites.

Personal protective items designed to reduce injury due to ballistic impact, such as vests and helmets, are usually fabricated from high-performance polymeric fibres, e.g., aramid or polyethylene. Research into the ballistic impact response of laminated composites is still mainly empirical in nature. The foremost concern in personal armour design is the prevention of projectile penetration (Lee *et al.*, 1994).

Different measures have been used to measure the ballistic performance of composite laminates. Due to the complexity of the ballistic impact response of composite materials, these methods can give completely different results for identical materials (Frissen *et al.*, 1995). The ballistic limit and the V_{50} are the most commonly used methods to assess the ballistic performance of composite laminates. The ballistic limit is the critical level of the projectile impact velocity or kinetic energy below which no perforation of the laminate occurs (Lee *et al.*, 1994). The V_{50} is the projectile impact velocity for which 50 % of the laminates tested are completely perforated (Frissen *et al.*, 1995). None of the currently available ballistic performance criteria for laminated structures considers the damage mechanisms involved in the penetration process and the deformation of the composite.

The current consensus from research on the ballistic impact response of laminated helmets is that delamination may be a possible cause of head injuries at impact velocities close to the ballistic limit. At these impact velocities, complete perforation of the helmet might be prevented, but the projectile's kinetic energy might be sufficient to separate the underlying, non-perforated laminate layers from the remainder of the helmet. This separation of the helmet interior is a delamination process and the delaminated layers are generally referred to as the backplane. The impact of the delaminated backplane with the head is thought to be a potential cause of skull fracture and underlying brain damage. Therefore, even if complete perforation of the helmet is prevented, its wearer may still suffer severe head injuries.

1.2 Objective and Strategy

In order to support further optimisation of the ballistic performance of composite laminates, a more thorough understanding of the mechanisms causing backplane deformation is required. The complex response of composite laminates together with the high costs and limited reproducibility of ballistic impact tests renders completely experimental approaches expensive and time consuming. Numerical modelling can provide a partial solution to this problem, since it allows a fast and relatively inexpensive means of gaining insight into the parameters governing the response of composite laminates to ballistic impact.

While numerous physical and numerical models of the penetration and perforation of isotropic materials have been published, corresponding models for composite materials are much more limited (Zhu *et al.*, 1992a). The few available models focus mainly on the ballistic limit of the laminate or the final velocity of the projectile. Less attention is paid to predicting the damage and deformation of the laminate.

This report presents a numerical model that simulates the penetration and backplane deformation of ballistically impacted laminates. The ultimate goal of the model is to predict the formation of the backplane in laminated helmets and its subsequent impact with the head.

A prerequisite for such a numerical model is a basic understanding of the mechanisms involved in the penetration and backplane deformation. As was mentioned previously, a reasonable amount of data is available on the penetration/perforation of ballistically impacted laminated composites, since the main emphasis of research in this area is the determination of the ballistic limit velocity, but little data is available on the delamination and backplane deformation.

On the other hand, there is a vast amount of information on delaminations related to drop weight impacts. Drop weight impacts involve much higher impactor masses and much lower impact speeds than ballistic impacts and, in general, little or no penetration results. Consequently, the loading characteristics differ substantially between ballistic and drop weight impacts. However, for the current research, the basic mechanisms involved in the initiation and growth of delaminations observed in drop weight impacts are considered to be applicable to ballistic impact scenarios. The rationale for this presupposition will be outlined in Section 1.4.2.

The remainder of this chapter gives an overview of the current understanding of the penetration and delamination behaviour of impacted laminated composites. Theoretical, experimental and numerical approaches are reviewed. Information on the penetration behaviour is obtained from research on ballistic impacts, whereas the delamination response is reviewed mainly from work related to drop weight impacts. This chapter closes with a section outlining how the information found in the literature was applied in the development of the numerical model that is presented and verified in the remainder of this report.

1.3 Penetration Mechanisms

As was mentioned before, research into the ballistic response of composite laminates is still mainly empirical, with the main emphasis on the determination of the perforation resistance. Consequently, the majority of the data available in this area is related to the penetration response of laminates to a variety of projectile types and calibres. The following gives an overview of the current understanding of the damage mechanisms involved in the penetration of laminated composites.

Punching failure, fibre failure, matrix cracking, and delamination are generally considered to be the principal damage mechanisms in ballistically impacted laminates (Critescu *et al.*, 1975; Langlie and Cheng, 1989; Zhu *et al.*, 1992a,b; Lee and Sun, 1993; Zee and Shieh, 1993; Lee *et al.*, 1994; Wu *et al.*, 1994; Wu and Chang, 1995; Goldsmith *et al.*, 1995). In general, these damage modes interact and many of them are strongly dependent on the impact conditions (Peijs *et al.*, 1994). Langlie and Cheng (1989) argued that these damage modes occur in a sequential order during the impact process (Figure 1.1). According to Langlie and Cheng (1989), the relative thickness of each damage stage depends on the overall laminate thickness.

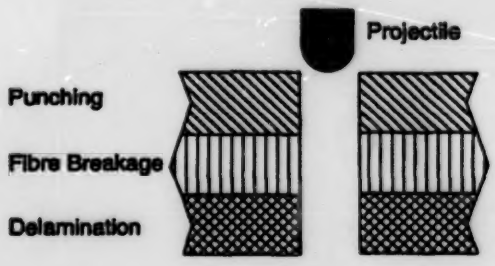

Figure 1.1: Penetration damage mechanisms and order in which they occur during penetration process as proposed by Langlie and Cheng (1989).

In general, the damage response of ballistically impacted laminates depends on the laminate properties, environmental effects, and impact conditions (Peijs *et al.*, 1994). Lin and Bhatnagar (1992) observed that the energy absorption in ballistically impacted Spectra (polyethylene) laminates depended on the areal density of the laminate and the size of the projectile. Segal (1991) surveyed the ballistic performance of various types of fibres and composites and concluded that the ballistic performance of a composite depends mainly upon the energy absorbing characteristics of the fibre and is less dependent upon the type of resinous binder. Segal found that a high areal density and fibre volume resulted in optimum ballistic performance.

Lin and Bhatnagar (1992), Zhu *et al.* (1992b) and Lee *et al.* (1994) reported differences between the ballistic response of unidirectional and woven laminated composites. Zhu *et al.* (1992b) found that the ballistic limit of woven Kevlar-29 laminates varied linearly with laminate thickness, but found that neither lay-up nor matrix volume fraction changes resulted in significant differences in the response of fully perforated specimens. Wu and Chang (1995) observed that the amount of fibre breakage depended on the impact velocity of the projectile. Lee *et al.* (1994) reported that the resin stiffness played an important role in the ballistic impact resistance of Spectra laminated composites.

Several researchers have compared the response of composite laminates to ballistic impact with quasi-static penetration to check whether quasi-static penetration tests could be used to characterise the damage response of ballistically impacted laminates. Quasi-static penetration tests are cheaper, much easier to perform, and better reproducible than ballistic impact tests. Zhu *et al.* (1992b) and Wu *et al.* (1994) observed significant differences in the damage patterns resulting from these tests, whereas Lee and Sun (1993) found that the damage pattern in ballistically impacted laminates resembled that observed in quasi-static punch tests.

The differences in the observations by the various researchers given above are most likely related to the applied projectile shape and impact velocity. Quasi-static penetration tests can probably be used to gain insight in the damage mechanisms involved in ballistic impact tests close to the ballistic limit, since the deformation of the laminate seems to be similar under both loading conditions. However, quasi-static tests cannot be used to characterise ballistic impact tests at velocities considerably above the ballistic limit.

A number of models have been proposed to predict the response of laminated composites to ballistic impact (Langlie and Cheng, 1989; Lin and Bhatnagar, 1992; Zhu *et al.*, 1992a; Lee and Sun, 1993; Lee *et al.*, 1994; Goldsmith *et al.*, 1995; Vinson and Walker, 1995). As a result of the emphasis on the penetration process in this research area, most models focus on the ballistic limit of the laminate or the final velocity of the projectile after penetration. Most of these models are analytical and can, therefore, only determine the global behaviour of the laminate and the projectile. Such analytical models do not provide the ability to perform detailed, local analyses as do finite element models. Langlie and Cheng (1989) have been amongst the few researchers who developed a finite element model to predict the response of laminated composites to ballistic impact. However, their model mainly focussed on penetration behaviour and paid little attention to the deformation of the laminate.

1.4 Delamination Mechanisms

Even though delamination is generally acknowledged as one of the major damage mechanisms in ballistically impacted laminates, information on the extent of delaminations and the mechanisms involved in their evolution under ballistic impact is scarce. The vast majority of research into impact induced delaminations has been focussed on high mass/low velocity impacts, mainly due to their detrimental effects in aerospace applications (e.g., tool drops on aircraft structures). This section gives an overview of the current understanding of the delamination mechanisms in high mass/low velocity impacts, followed by a discussion outlining how these findings can be applied to the prediction of delaminations under ballistic conditions.

1.4.1 Drop Weight Impact

Low velocity impact damage in composites is especially insidious because the surface damage is often minor and difficult to detect, while the internal hidden damage may be extensive (Gosse and Mori, 1988; O'Brien and Elber, 1993). Although no standard exists, high mass/low velocity impacts are generally simulated by drop weight tests on composite coupons. Drop weight impact tests on composite laminates are reasonably well characterised and the damage modes occurring in these impacts are fairly well understood and documented.

Drop weight impact damage is commonly denoted by the Characteristic Damage State, CDS (Gosse *et al.*, 1988), which refers to the three mutually orthogonal modes of damage typically found in thin composite laminates subjected to drop weight impact. These modes are matrix cracking, delamination, and fibre breakage and generally occur in the order listed with increasing impact energy (Srinivasan *et al.*, 1992). The CDS is a function of the structural geometry, loading condi-

tions, material organisation (tape, fabric, etc.), boundary conditions, and material properties (Gosse *et al.*, 1988).

Matrix cracking has been widely reported as the first major damage mode in laminated composites under low velocity impact (Joshi and Sun, 1987; Choi *et al.*, 1991a,b). The location of the initial intralaminar matrix cracks seems to depend on the stacking sequence (Majeed, 1995; Fuoss, 1996). The propagation of matrix cracks is, in general, strongly influenced by the orientation of the fibre reinforcement with respect to the loading direction and the stacking sequence (Poon *et al.*, 1993). The reinforcing fibres influence the pattern of crack propagation by acting as crack stoppers. This crack-arresting capability of the fibres not only prohibits the dominance of a single crack but also encourages similar cracks to form throughout the laminate at increased loading levels.

Delaminations are known to initiate at the intersection of matrix cracks and ply interfaces (Joshi and Sun, 1987; Lin and Lee, 1990; Choi *et al.*, 1991a; Salpekar and O'Brien, 1991; Hull and Shi, 1993; O'Brien and Elber, 1993; Lammerant and Verpoest, 1996). A matrix crack that extends all the way to a ply interface is generally referred to as a critical matrix crack. Based on their experiments, Choi *et al.* (1991b) claimed there existed an impact energy threshold associated with the energy required to initiate the first critical matrix crack. Lin and Lee (1990) found that the critical matrix cracks first initiated at the lowest ply and that those cracks caused delamination to subsequently initiate at the lowest ply interface. The tendency of impacted laminates to form multiple similar matrix cracks throughout the laminate rather than a dominant single crack, creates a multitude of possible delamination nucleation sites.

Delamination growth is generally considered to be an extension of the intralaminar matrix crack into the ply interface and the growth direction is usually away from the impact area (Joshi and Sun, 1987). The intralaminar and interlaminar matrix cracks often interact to form a complex network of matrix damage which affects structural performance. Several researchers (Dost *et al.*, 1988; Gosse and Mori, 1988; Lagace, 1993; Vietinghoff, 1993) determined a spatial relationship between matrix cracks and delaminations by observing that the transverse matrix cracks connected delaminations, forming circular sublaminates that repeat with ply stacking sequence through the laminate thickness. The sublaminates were found to form wedge-shaped damage areas spiraling through the thickness at each ply interface (Joshi and Sun, 1987; Daniel and Wooh, 1990; Srinivasan *et al.*, 1992).

Figure 1.2 depicts the typical matrix cracking and delamination damage found in an impacted composite specimen. The delamination area is generally narrow below the impact zone and expands as it moves away from the impact centre. O'Brien and Elber (1993) argued that this conical shape of matrix cracks and subsequent delaminations was created by the high transverse shear stresses induced during the impact.

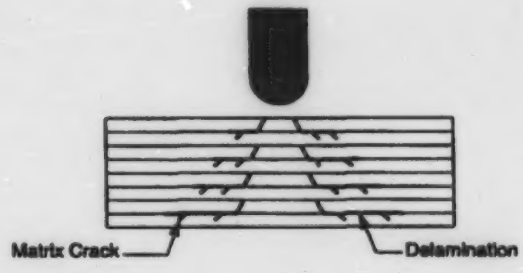

Figure 1.2: Typical matrix cracking and delamination damage in an impacted composite laminate (Fuoss, 1996).

Gosse and Mori (1988) observed a stair-case type progression in the conical delamination pattern depicted in Figure 1.2. This staircase-type pattern in shown in Figure 1.3.

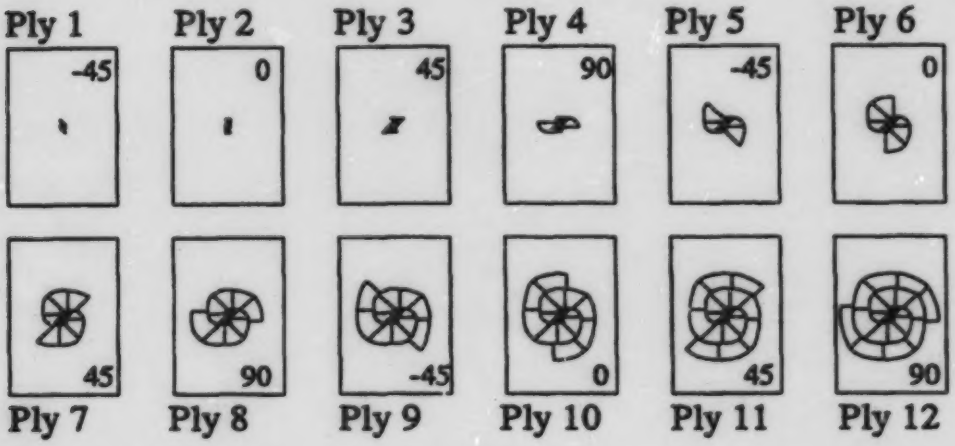

Figure 1.3: Staircase delamination pattern through bottom 12 plies of a $[-45/0/45/90]_{3s}$ laminate. The impacted surface is at ply 1 (Gosse and Mori, 1988).

The shape of a delamination at the ply interface depends on the stacking sequence. A commonly observed shape is an elongated ellipse ("peanut") with a section that narrows at the impact point (Figure 1.4). The elongated portion of the delamination is closely aligned with the fibre direction of the bottom ply of the interface (Lu and Liu, 1991; Hung *et al.*, 1995). This anisotropic growth of delaminations has been hypothesised to be a result of a mismatch in bending stiffness between adjacent anisotropic laminae (Hong and Liu, 1989).

Hong and Liu (1989) and Abrate (1991) reported on the existence of a damage threshold above which the projected delamination area was found to increase linearly with the kinetic energy of the impactor. Poon *et al.* (1991) found that

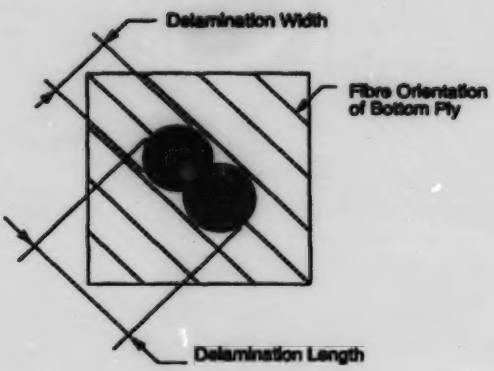

Figure 1.4: Typical shape of delamination damage at an interface of an impacted composite laminate (Fuoss, 1996).

the delamination area increased with impact energy up to a critical level and then remained constant.

The complex network of intra- and interlaminar (delamination) matrix damage affects structural performance, which is manifested in stiffness loss and in the development of local stress concentrations in the load-carrying plies which lead to a redistribution of loads within the laminated structure. The load redistribution is often responsible for the failure of fibres in the major load-carrying plies, which, in turn, precipitates premature structural failure (Poon *et al.*, 1993).

At sufficiently high impact energies, Vietinghoff (1993) noted the occurrence of fibre micro-buckling in the vicinity of the local contact zone. The micro-buckling failures of the fibres on the upper surface area are likely due to the interaction of local compression by the impactor and bending compression of the entire plate.

At high impact energy levels, fibre breakage occurs on the back face (tension side) of the laminate (Poon *et al.*, 1991). Matrix cracking is also associated with this back face damage (Vietinghoff, 1993; Sjöblom *et al.*, 1988). This damage is

a localised effect due to the impactor pushing out the composite material directly underneath it. At a sufficiently high impact energy level, complete penetration of the specimen occurs, corresponding to the effective upper energy level limit for this kind of impact testing (Poon *et al.*, 1991).

The evolution of drop weight impact damage in thin composite laminates with increasing impact energy levels can be summarised as follows (Majeed, 1995):

i) At low impact energies, minor damage in the form of a small plastic indentation is formed on the impact surface;

ii) At low to moderate impact energies, matrix cracking initiates in the lowest ply of the laminate. As the impact energy increases, delamination forms at the first ply interface. Matrix cracking and delamination damage subsequently spread upwards through the laminate;

iii) At higher impact energies, fibre micro-buckling occurs on the impact face near the contact zone. Fibre breakage and matrix cracking damage begins to occur on the back face of the specimen directly below the impactor;

iv) At a well-defined threshold value of impact energy, complete penetration of the specimen occurs. This is the upper energy limit for drop weight impact testing.

1.4.2 Ballistic Impact

This section discusses how information obtained from drop weight impacts can be used to predict delaminations under ballistic conditions. Drop weight impacts involve higher masses, lower impact velocities, and larger contact surface areas than ballistic impacts. Consequently, the loading conditions differ considerably between these two types of impact. In drop weight impacts, the damage is distributed over a large area, well beyond the point of impact, and the laminate deflects considerably. The damage in laminates impacted well above their ballistic limit is confined to the crater area and hardly any deformation is observed. However, at ballistic impacts close to the ballistic limit, the delamination and deformation response of the laminate resembles that observed in drop weight impacts.

Zhu *et al.* (1992a) observed in ballistic experiments that the maximum delamination was generally found to occur on the back side of the specimen. This is in agreement with the delamination pattern observed in drop weight tests, as was shown in Figure 1.2. Zhu *et al.* (1992a) argued that the reflection of the pressure wave created by the projectile impact generates a tensile wave which produces delamination at the bottom of the laminate.

Several researches observed that ballistically impacted laminates exhibit bulging deformation underneath the impactor (Zhu *et al.*, 1992b,a; Lee and Sun, 1993; Wu *et al.*, 1994; Frissen *et al.*, 1995; Goldsmith *et al.*, 1995; Vinson and Walker, 1995; Wu and Chang, 1995). The bulging is similar in shape to the laminate deflection in drop weight impacts, but occurs on a smaller scale and is localised closely around the impacted area. Further, cross-sections of ballistically perforated woven Kevlar-29 specimens presented by Zhu *et al.* (1992b), showed a conical damage pattern with the largest amount of fibre failure and delamination at the back face of the specimen.

The fore-going experimental observations in ballistically impacted laminates indicate that the damage mechanisms in these tests were similar to those observed in drop weight impacts. It seems reasonable, therefore, to assume that delaminations are initiated in ballistic impacts by matrix cracks extending into the ply interface, and that delaminations and intralaminar matrix cracks strongly interact during the impact event.

Besides the delamination mechanisms observed in drop weight impacts, other mechanisms that are related to projectile penetration can cause delamination in ballistically impacted laminates. In the impacted area, the material deforms laterally as well as downward, producing both in-plane and out-of-plane compression (Zhu *et al.*, 1992a). The in-plane compression results in interlaminar shear stresses, whereas the out-of-plane compression leads to interlaminar normal stresses. Both types of interlaminar stresses can cause delamination growth.

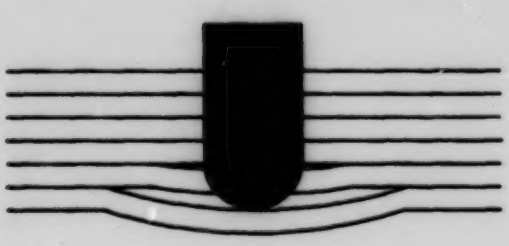

Figure 1.5: Delamination mechanism in ballistically impacted laminates as proposed by Zhu *et al.* (1992a).

Delaminations at the bottom of the panel can be further extended when the projectile separates the underlying plies from the remainder of the laminate (Figure 1.5). The separated plies are generally referred to as the backplane. Zhu *et al.* (1992a) and Goldsmith *et al.* (1995) found that for blunt projectiles the delaminations extended much further into the laminate than was the case for sharp projectiles. Zhu *et al.*

(1992a) argued that the penetration of composite laminates by sharp projectiles resulted in a localised delamination region, since the sublaminate could not deform very much before it was perforated by the projectile.

Critescu *et al.* (1975) observed in ballistically impacted angle-ply laminates that delaminations seemed to be induced through a strip of finite width within the first lamina, referred to as the generator strip. The generator strip was pushed forward by the projectile, inducing shear cracks in the matrix parallel to the fibres. This strip, in turn, applied a transverse load to the second ply and resulted in a separation between the first two laminae. The delamination spread until it was stopped by the cutting of the generator strip by the projectile. This process repeated through the thickness of the plate. Lee *et al.* (1994) observed similar phenomena in angle-ply, but not in woven, laminates.

In summary, the delamination mechanisms observed in drop weight impacts also occur under ballistic conditions. In addition, penetration related mechanisms can cause additional damage in ballistic impacts. Both types of impact result in the same major damage modes (fibre failure, matrix cracking, delamination, penetration). Therefore, the information available from drop weight impacts can be used to predict the damage response under ballistic conditions. The major differences are that penetration phenomena are much more important in ballistic impacts and that these tests occur at a much higher rate.

1.5 Delamination Initiation and Growth Criteria

Over the last few decades, several techniques have emerged for predicting the initiation or growth of delamination in composite materials. These techniques can typically be ranked under one of two main approaches. One is based on a strength of materials approach, in which a stress-based failure criterion is utilised to predict delamination initiation. The second approach is based on fracture mechanics techniques and generally involves the calculation of the strain energy release rate to predict delamination growth.

These two approaches will be outlined in the following, together with commonly used experimental techniques that are based on these approaches. Experimental characterisation of delamination was not part of the research presented in this report, but is discussed briefly for completeness. Further, a relatively new approach using Continuum Damage Mechanics (CDM) to predict both the initiation and initial growth of damage in composites will be described.

1.5.1 Strength of Materials Approach

Theoretical Considerations

The early work looked at qualitatively predicting when delamination was likely to occur based on the calculated values of the interlaminar stresses (Pipes and Pagano, 1970). Various techniques have been applied and different authors have concentrated on the interlaminar normal and shear stresses. These techniques can all be grouped under a strength of materials approach, which assumes an intact laminate, devoid of any defects, and evaluates the stresses in the region of interest by either numerical or analytical methods. The stresses so obtained are then subjected to either a point stress or an average stress criterion to predict the occurrence of failure. Failure

refers to the breakdown of the material in the vicinity of the region where the failure criterion has been applied.

The magnitudes of the interlaminar stresses are known to be dependent upon the laminate layup, ply stacking sequence and ply thickness. Therefore, these factors greatly influence onset and growth of delamination (Poon *et al.*, 1993). When implemented in the finite element method, a point-wise criterion leads to failure prediction that will be dependent on the discretisation of the mesh (Majeed, 1995). Therefore, failure criteria that are associated with an average distance or area over which the stresses are calculated are more appropriate for implementation in the finite element method. Further, the average stress approach has met with considerable success in predicting the initiation of delamination (Paul *et al.*, 1992). However, the strength of materials approach can only predict the onset of failure and is unable to specify the size of the failed/damaged zone or the subsequent failure process if the initial damage grows in a stable manner (Lagace and Bhat, 1993).

The strength of materials approach was quantified by Kim and Soni (1984, 1986) using an average stress concept similar to that used by Whitney and Nuismer (1974) for the prediction of the fracture stress in notched composites. They reasoned that failure is not caused by the stress at some point, but rather by the average of the stress(es) over some critical area reaching an ultimate value. This critical area was defined by a characteristic distance and Kim and Soni proposed that this distance is a material constant, which is a function of material, layup, stacking sequence, geometry, and loading. Kim and Soni used a characteristic distance of one ply thickness from the delamination edge. Brewer and Lagace (1988) generalised this approach to include all three interlaminar stresses σ_{i3} and compared each with the associated interlaminar strength:

$$\left(\frac{\bar{\sigma}_{33}}{S_{33}}\right)^2 + \left(\frac{\bar{\sigma}_{13}}{S_{13}}\right)^2 + \left(\frac{\bar{\sigma}_{23}}{S_{23}}\right)^2 = 1 \tag{1.1}$$

where S_{i3} are the interlaminar strength values. This equation is referred to as the Quadratic Delamination Criterion. The overbar on the stresses denotes that the stresses are averaged over a critical dimension, which must be determined experimentally. The local (material) 1–direction is in the fibre direction, the 2–direction is perpendicular to the fibre direction, and the 3–direction is perpendicular to the laminate plane. This quadratic criterion compared well with experimental uniaxial test results from graphite/epoxy specimens (Brewer and Lagace, 1988).

Choi and Chang (1992) used the Quadratic Delamination Criterion as a starting point for their criterion, which predicts delaminations that initiate from matrix cracks. Using finite element techniques, Choi and Chang predicted the occurrence of a critical matrix crack with the following criterion

$$\left(\frac{\bar{\sigma}_{22}}{S_{22}}\right)_n^2 + \left(\frac{\bar{\sigma}_{23}}{S_{23}}\right)_n^2 \geq 1 \tag{1.2}$$

The subscript n refers to the n^{th} layer in the composite. Once the critical matrix crack size is reached, the following delamination criterion is used to predict the initiation of a delamination at the critical matrix crack

$$D_s\left[\left(\frac{\bar{\sigma}_{23}}{S_{23}}\right)_m^2 + \left(\frac{\bar{\sigma}_{13}}{S_{13}}\right)_m^2 + \left(\frac{\bar{\sigma}_{22}}{S_{22}}\right)_m^2\right] \geq 1 \tag{1.3}$$

Here, D_s is an empirical constant, determined by experiments, that accounts for the fracture toughness of the laminate and the subscript m refers to the m^{th} interface. Simulations using the Choi and Chang damage criteria agreed well with experimental impact data on graphite/epoxy specimens (Choi and Chang, 1992).

A variation of the strength of materials technique has been proposed by Sih (1981) and deals with the strain energy density ahead of the damage in a composite. Sih proposed that the rate at which the crack grows can be associated with the amount of energy absorbed and released by each element ahead of the advancing cracking. The key point is that the critical value of the strain energy density can be evaluated in a simple tension test, in the appropriate loading direction, by calculating the area under the stress-strain curve to failure. It is necessary to calculate the strain energy density ahead of the delamination and to compare this value to the measured critical value. This is generally done at some distance ahead of the damage region, this distance being a material parameter. This technique has met with some success in predicting intraply matrix cracking. Little work has been done with this model for delamination; nevertheless, it deserves further attention (Lagace and Bhat, 1993).

Gosse and Mori (1988) used their so-called K-rule to predict the spatial distribution of delaminations and coupling matrix cracks resulting from impacts on quasi-isotropic laminated composite panels. The K-rule uses the material lay-up and the principal tensile strains in the material to relate transverse matrix crack initiation to subsequent delamination initiation and propagation. The impact induced strains were determined using the analytical impact stress analysis by Dobyns (1980). However, this stress analysis does not determine the normal strains in the laminate thickness direction (Gosse and Sorscher, 1988). The K-rule incorporates lay-up dependence, such that the angular orientation of the coupling transverse cracks depends on the fibre orientation in adjacent plies. As a result, the K-rule is capable of predicting the wedge shape damage pattern shown in Fig. 1.2 and the staircase delamination pattern shown in Fig. 1.3. Gosse *et al.* (1988) found that the initiation location and growth of coupling matrix cracks depended on the existence of previously initiated cracks.

Experimental Characterisation

A commonly used test based on the strength of materials approach is the Short-Beam Shear (SBS) test (ASTM D 2344-84). The SBS test is mainly used to characterise delamination initiation by centre-loading a laminated specimen in three-point bending with the specimen ends on two supports that allow lateral motion (Figure 1.6).

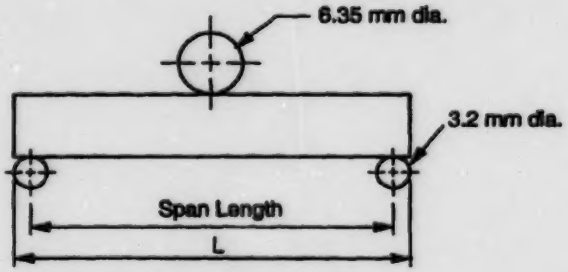

Figure 1.6: Short-Beam Shear test set-up (ASTM D 2344-84, 1997).

The span-to-thickness ratio L/d of the SBS specimen is chosen such that interlaminar shear failure is induced along the centre line rather than tensile or compressive failure on the surface of the beam. The load to break the specimen is recorded and used to calculate the interlaminar shear strength. However, when thin beams are used, which is necessary for high-modulus composites such as graphite or aramid, the material often fails in a failure mode other than interlaminar shear failure (Whitney, 1989).

1.5.2 Fracture Mechanics Approach

Theoretical Considerations

The great majority of work on the prediction of delamination has centred on a fracture mechanics methodology employing the concept of strain energy release rate (Jurf and Pipes, 1983; Wang, 1983, 1989). This methodology is based on the reasoning that delamination can only occur if the strain energy released as the delamination grows is sufficient to provide the energy needed to create the new surfaces due to this delamination (Rybicki *et al.*, 1977). This approach is equivalent to the classical fracture mechanics crack growth criterion by Griffith (1920). The strain energy is then equated to a critical material parameter, known as the critical strain energy release rate or delamination fracture toughness, G_c.

The propagation of matrix cra. s in laminates is, in general, fundamentally different from that seen in metallic materials. The failure of metallic structures is usually precipitated by a dominant crack which propagates in a self-similar manner until a critical size is reached. The propagation of matrix cracks is, in general, not self-similar and is strongly influenced by the orientation of the fibre reinforcement with respect to the loading direction and the stacking sequence (Poon *et al.*, 1993). The reinforcing fibres influence the pattern of crack propagation by acting as crack stoppers. This crack-arresting capability of the fibres not only prohibits the dominance of a single crack but also encourages similar cracks to form throughout the laminate at increased loading levels.

As opposed to the strength of materials approach, the fracture mechanics method assumes the presence of an inherent defect in the material. Hence, the use of the term initiation of delamination holds a different meaning, since it is not the initial formation of the damage itself that is of interest, but the growth of a pre-existing

small defect. Contrary to the strength of materials approach, fracture mechanics can be used to predict the stable and unstable regimes of growth of damage (Lagace and Bhat, 1993).

The early work of Wang and coworkers (Wang, 1980, 1989) examined the application of the strain energy release methodology to the prediction of the initiation and growth of delamination using the finite element method. O'Brien and his colleagues (O'Brien, 1982; O'Brien and Martin, 1993; O'Brien and Elber, 1993) have been central in the development and extension of this methodology for delamination in composites, including the development of a number of simple equations to determine the total strain energy release rate for various delamination configurations.

In general, the growth of a crack under any mixed condition of loading can be broken down into three components: Mode I, the opening mode due to stresses normal to the fracture plane; Mode II, the in-plane shearing mode occurring due to shear stresses in the direction of crack propagation; and Mode III, the anti-plane shearing mode due to the shear stresses parallel to the propagating crack front (Fig. 1.7).

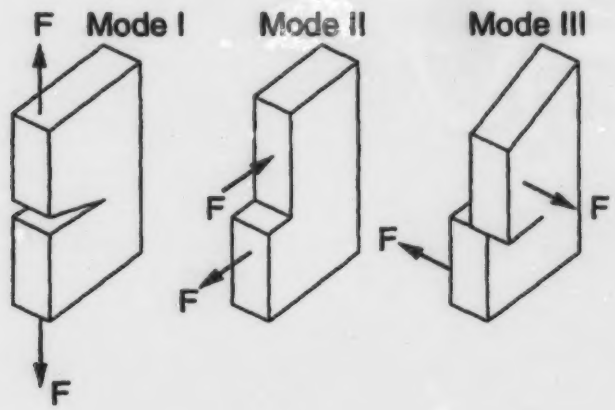

Figure 1.7: Interlaminar fracture modes.

Due to the anisotropic behaviour of laminated composites, delamination under general in-plane loading is a mixture of modes I and II. In applying the strain energy release rate technique to mixed-mode cases, it is necessary to determine the contribution of each of the modes, generally using the finite element technique, and then utilising a mixed mode strain energy release rate failure criterion (Hahn, 1983; Garg, 1988).

Most of the current research on mixed-mode failure criteria has focussed on mixed mode I-II fracture. For the prediction of delamination growth under mixed mode conditions, the following criterion is often used

$$\left(\frac{G_I}{G_{Ic}}\right)^m + \left(\frac{G_{II}}{G_{IIc}}\right)^n = 1 \tag{1.4}$$

where G_{Ic} and G_{IIc} are the critical energy release rates for pure Modes I and II, respectively, and m and n are constants determined by curve fitting of the experimental data. This type of failure criterion is not based on physical or morphological principles, but is simply a relationship to fit the data (Whitney, 1989). Bolotin (1996) argued that it was more appropriate to use the total energy release rate G as the generalised driving force for delamination growth under mixed mode conditions, assuming that the critical magnitude Gc depends on fracture mode.

Experimental Characterisation

Various tests have been developed for the characterisation of the effects of the individual fracture modes shown in Figure 1.7. The Double Cantilever Beam (DCB) test (ASTM D 5528-94a) is the most widely used method to measure the Mode I critical strain energy release rate G_{Ic} of composites. The DCB specimen is a laminated composite with a non-adhesive insert placed at the midplane at one end prior to curing, which serves as a delamination initiator. Opening forces are applied to

the specimen by means of piano hinges or loading blocks bonded to one end of the specimen (Figure 1.8).

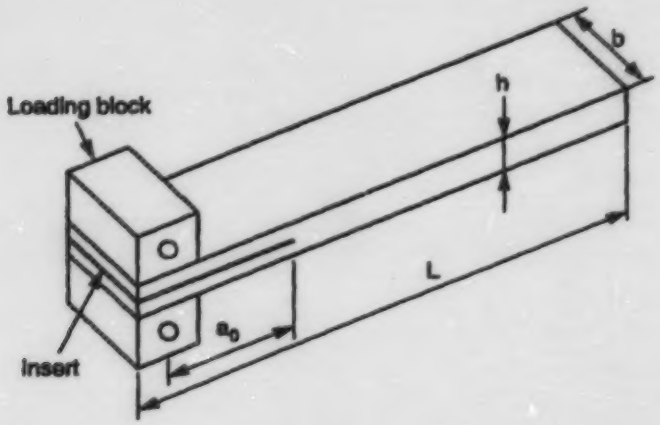

Figure 1.8: Double Cantilever Beam specimen (ASTM D 5528-94a, 1997).

The specimen is loaded continuously under displacement control and the load versus opening displacement trace at the point of load application is recorded. A DCB specimen subjected to displacement controlled loading usually experiences stable delamination growth (Whitney *et al.*, 1982), which allows several values of G_{Ic} to be determined along the specimen's length. The load versus opening displacement trace is also recorded during unloading to determine if any plastic deformation occurred during the test. A data reduction scheme is used to calculate the critical strain energy release rate, G_{Ic}, from the measured load-displacement curve.

The End Notch Flexure (ENF) specimen was first introduced by Russell and Street (1984), and has been widely used ever since for determining the interlaminar Mode II response of high-performance composite materials. As shown in Figure 1.9, the shear loading is applied to the specimen by three-point bending. As in the DCB test, a starter crack of a desired length, a_0, is introduced at one end of the beam.

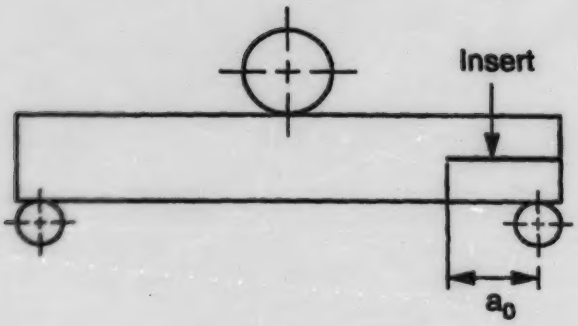

Figure 1.9: End Notch Flexure specimen (Martin, 1996).

Crack propagation in the ENF specimen tends to be unstable, even under displacement control, for the majority of the useful length of the beam (Martin, 1996). As a result, Russell and Street (1984) were able to obtain only two fracture energy values, G_{IIc}, for each specimen tested. The first value was associated with crack growth from the root of the starter crack. This initial crack usually arrests when it reaches the point of load application. If a large overhang is utilised at the unnotched end of the beam, the specimen can be slid over and reloaded to obtain a second value of G_{IIc}.

Stable Mode II delamination growth can be achieved by two alternative approaches to conducting the ENF test. In the Crack Sliding Displacement (CSD) test, the crack sliding displacement is controlled by a clip gauge, which results in stable delamination growth (Martin, 1996). The second alternative approach to the ENF test is the End Loaded Split (ELS) test, where the specimen is rigidly clamped at one end and loaded in bending at the other, resulting in stable delamination growth.

The mixed mode bending (MMB) test is one of the most commonly used mixed mode tests (Martin, 1996). The MMB test uses the same type of specimen as the DCB and ENF tests. By varying the position of the applied loading point, c, the mixture of the modes can be altered (Figure 1.10). Thus, virtually any combination of Modes I and II can be obtained from one specimen type. MMB toughness measurements may be used with DCB and ENF measurements to develop mixed mode delamination failure criteria.

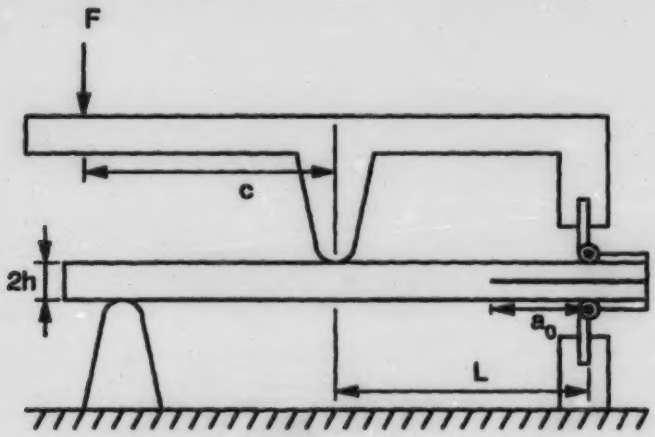

Figure 1.10: Mixed Mode Bending test specimen (Martin, 1996).

1.5.3 Continuum Damage Mechanics Approach

Theoretical Background

Continuum damage mechanics (CDM) is a relatively new discipline that focuses on predicting the effects of progressive degradation of mechanical properties (damage evolution) on the macro-response and failure of solids (Kachanov, 1986; Krajcinovic and Lemaitre, 1987; Lemaitre, 1992; Krajcinovic, 1996). Damage evolution is related to the nucleation and growth of micro-cracks and other micro-defects. Since CDM is the adopted approach for the numerical model presented in this report, an extensive description of the theoretical background of CDM is provided in this section.

CDM bridges the gap between traditional elasticity theory and fracture mechanics. The CDM-description of a defect-free material is equivalent to the application of elasticity theory. The CDM and elasticity theories will deviate as soon as micro-defects start to nucleate and grow with increased loading. At the other end of the spectrum, when the growth of one or at most a few micro-cracks becomes the dominant aspect of the deformation of the material, a CDM-description will no longer suffice and the fracture mechanics theory must be applied.

Continuum damage models are typically derived within the framework of irreversible thermodynamics with internal variables, which provides a qualitative measure of the effects that randomly distributed micro-defects exert on the macro-parameters of a structure (Coleman and Gurtin, 1967; Lubliner, 1972; Germain *et al.*, 1983; Krajcinovic, 1983; Kestin, 1992; Lemaitre, 1992; Maugin, 1992; Krajcinovic, 1996). Assuming that there are no internal heat sources and heat fluxes and assuming infinitesimal deformations, the internal energy per unit mass, e, at a local continuum point $\boldsymbol{x}$ is given by:

$$e = e[\boldsymbol{x}, s(\boldsymbol{x}), \epsilon(\boldsymbol{x}), \omega(\boldsymbol{x})], \tag{1.5}$$

where s is the entropy per unit mass, ϵ is the strain tensor, and ω is a set of (mechanical) internal variables. The explicit notation of the dependence on location x will be dropped in the following, but this dependency is implied throughout the remainder of this section.

The internal variables are introduced in the thermodynamic formulation to describe the irreversible (dissipative) rearrangements in the micro-structure. Each internal variable describes a particular dissipative mechanism of the micro-structural rearrangement. The plastic strain, or an appropriate function of plastic strains, is an example of a commonly used internal variable to describe the inelastic response of ductile materials. In CDM, common internal variables are parameters that indicate the extent, distribution, and orientation of the micro-cracks. One of the central aspects of the theory of thermodynamics with internal variables is related to the selection of the set of internal variables (in our case damage variables).

Dissipation is governed by the second law of thermodynamics, which is expressed by the Clausius-Duhem inequality (Coleman and Gurtin, 1967):

$$\rho\theta\dot{s} \geq \rho\dot{e}(s,\epsilon,\omega) - \sigma : \dot{\epsilon} \tag{1.6}$$

where ρ is the density, θ is the absolute temperature, σ is the Cauchy stress tensor, and the symbol (:) stands for the inner (scalar) product of two tensors. Substitution of eqn. (1.5) into (1.6) yields the following expression for the dissipation rate:

$$D \equiv -\rho\frac{\partial e}{\partial \omega}\dot{\omega} \geq 0. \tag{1.7}$$

Using a Legendre transformation, we can replace the internal energy e by the Helmholtz free energy H:

$$H(\theta,\epsilon,\omega) = u(s,\epsilon,\omega) - \theta s \tag{1.8}$$

Assuming isothermal processes only, we define the thermodynamic forces conjugate to the damage variables by:

$$\boldsymbol{Y} = -\frac{\partial H(\epsilon, \omega)}{\partial \omega} \tag{1.9}$$

In continuum damage mechanics, the thermodynamic forces have the interpretation of energy released per volume due to advancement of damage. Lemaitre (1985) referred to $\boldsymbol{Y}$ as "energy release rate", a term borrowed from fracture mechanics. The dissipation rate inequality can now be viewed as the inner product between the rates of the internal variables and the energy release rates

$$D = -\rho \boldsymbol{Y} : \dot{\omega} \geq 0. \tag{1.10}$$

The kinetic equations for the internal variables are typically formulated by means of a damage (dissipation) potential $Q(\boldsymbol{Y}, \omega)$, an approach similar to the use of a yield function (plastic potential) in plasticity theory. These potential functions are constitutive equations which relate the internal variables with their conjugate thermodynamic forces. The constitutive relations are usually based on relevant experimental data, guided by the restrictions imposed by the principles of objectivity and dissipation (eqn. (1.10)).

The state of damage is assumed not to change along a path of strain in the interior of a well-defined region, called the elastic range, $\mathcal{E}$. It is further assumed that any state of stress or strain lies either inside $\mathcal{E}$ or on the boundary $\partial\mathcal{E}$ of the elastic range, defined by the damage (failure) surface. The damage surface is analogous to the yield surface in plasticity theory and defines the state and conditions which must be satisfied for the onset or the continuation of the damage process.

The damage surfaces are defined in the thermodynamic force space, $\boldsymbol{Y}$. However, neither the forces, $\boldsymbol{Y}$, nor their rates are directly controllable in a loading process. Therefore, the damage surfaces are usually defined by damage (failure) criteria in

stress space, $f_i(\sigma, \omega, r)$, or strain space, $g_i(\epsilon, \omega, r)$. The components of variable r are the damage thresholds, which determine the size of the elastic region. The damage thresholds, r, play a role in damage mechanics that is similar to that taken by the yield stress in plasticity.

The following loading conditions (in strain space) are distinguished (Matzenmiller *et al.*, 1995):

$$\begin{aligned} g_i = 0 \quad &\text{and} \quad \frac{\partial g_i}{\partial \epsilon}\dot{\epsilon} > 0 \quad \text{loading} \\ g_i = 0 \quad &\text{and} \quad \frac{\partial g_i}{\partial \epsilon}\dot{\epsilon} = 0 \quad \text{neutral loading} \\ g_i = 0 \quad &\text{and} \quad \frac{\partial g_i}{\partial \epsilon}\dot{\epsilon} < 0 \quad \text{unloading} \end{aligned} \tag{1.11}$$

During unloading the state moves inside the elastic range, away from the damage surface. In the neutral loading case, the state moves along the fixed damage surface. It is generally assumed that during the loading case, damage evolution takes place along a direction normal to the damage surfaces (Krajcinovic, 1996). This assumption is similar to associative flow in plasticity. As a result, the elastic range $\mathcal{E}$ has to expand outwards, at least locally, and the damage threshold rate $\dot{r}$ must be positive, $\dot{r} \geq 0$. Because the stress (or strain) state has to remain inside or at least on the border of the elastic range, the consistency condition $\dot{g} = 0$ has to hold during the damage evolution process. The consistency condition can be written in expanded form:

$$\frac{\partial g}{\partial \epsilon}\dot{\epsilon} + \frac{\partial g}{\partial \omega}\dot{\omega} + \frac{\partial g}{\partial r}\dot{r} = 0 \tag{1.12}$$

Since $\frac{\partial g}{\partial r}\dot{r} \geq 0$, the consistency equation puts restrictions on the amount and/or direction of damage growth $\dot{\omega}$:

$$-\frac{\partial g}{\partial \omega}\dot{\omega} \leq \frac{\partial g}{\partial \epsilon}\dot{\epsilon} \tag{1.13}$$

This restriction is comparable to critical softening in elastoplasticity (Lubliner, 1990). It states that a possible shrinkage of the elastic range $\mathcal{E}$ due to damage growth is less than the expansion of the damage surface resulting from an increase in strain (Matzenmiller *et al.*, 1995).

In classical continuum damage mechanics, as proposed by Kachanov (1958), only the undamaged (effective) part of the cross-section A (net-area) is assumed to carry loading. Consequently, the stresses σ in the failure criteria should be interpreted as effective stresses, $\hat{\sigma}$, related to the net area. This means that the failure criteria are assumed to hold in terms of the effective stresses rather than the nominal (true) stresses.

The effective stress tensor $\hat{\sigma}$ can in general be represented by a projection of the Cauchy stress tensor:

$$\hat{\sigma} = M(\omega_d) : \sigma \tag{1.14}$$

where $M(\omega_d)$ is the effective-stress operator (a fourth order tensor) that is a function of the (internal) damage variables ω_d. The specific form of this operator depends on the applied damage representation theory, which can either be derived from a phenomenological or a micro-mechanical approach. For reference, Hansen and Schreyer (1994) present a few examples of effective-stress operators.

The damage accumulation during a deformation process can be accurately described by the change of the effective stiffness tensor. In CDM models, the internal variables are usually chosen such that they reflect the effects of stiffness changes (Krajcinovic, 1996). The effective stiffness can be measured directly in a tensile test by repeatedly loading and unloading of the specimen.

A different method was used by Audoin and Baste (1994), who made very detailed ultrasonic measurements of the change of stiffness due to the anisotropic damage in a ceramic matrix composite. The changes in nine different components of the effective stiffness tensor were measured directly using an immersed interferometer within a tensile machine. The effective stiffness was found to be independent of the specimen size and insensitive to the details of the local stress concentrations and the distributions of weak spots in the material (within the hardening regime). The scatter of the effective stiffness measurements was acceptable and relatively independent of the experimental details (Krajcinovic, 1996).

CDM theory can be easily extended to incorporate ductile behaviour. In this case, the inelastic (residual) strain, ϵ_p, will be used to quantify the ductile behaviour while the damage parameters, ω_d, will provide measures of the deterioration of the solid. These internal variables are easily and uniquely identified and determined in simple experiments by measuring the residual strain and the change of slope of the unloading segment along the stress-strain curve.

Applications to Composite Materials

Several researchers have applied the CDM-theory to composite materials (Talreja, 1985, 1989, 1994; Allix *et al.*, 1995; Daudeville *et al.*, 1995; Matzenmiller *et al.*, 1995). Two of these publications will be discussed in the following.

Matzenmiller *et al.* (1995) applied the CDM-approach to model intralaminar damage in unidirectional composite materials. They represented the damage accumulation inside a laminate by means of intralaminar compliance changes. These compliance changes were quantified by the introduction of the (internal) damage variables ω:

$$C(\omega) = \begin{bmatrix} \frac{1}{(1-\omega_{11})E_{11}} & -\frac{\nu_{12}}{E_{11}} & 0 \\ -\frac{\nu_{12}}{E_{22}} & \frac{1}{(1-\omega_{22})E_{22}} & 0 \\ 0 & 0 & \frac{1}{(1-\omega_{12})G_{12}} \end{bmatrix} \tag{1.15}$$

The inverse of the compliance matrix $C(\omega)$ is the stiffness matrix $S(\omega)$, which will always exist as long as the damage variables are less than unity, $\omega_{ij} < 1$.

The following criteria were used to predict fibre and matrix failure, respectively:

fibre failure:

$$f_1 = \left(\frac{\sigma_{11}}{(1-\omega_{11_{c,t}})S^2_{11_{c,t}}} \right)^2 - r_{1_{c,t}} = 0 \tag{1.16}$$

matrix failure:

$$f_2 = \left(\frac{\sigma_{22}}{(1-\omega_{22_{c,t}})S^2_{22_{c,t}}} \right)^2 + \left(\frac{\sigma_{12}}{(1-\omega_{12_{c,t}})S^2_{12}} \right)^2 - r_{2_{c,t}} = 0 \tag{1.17}$$

The notation $(\ )_{c,t}$ is used to indicate that differences exist in quantities for compressive versus tensile loading. Using the constitutive tensor, the failure criteria f_i in stress space can be transformed to the failure criteria g_i in strain space.

The rate equations for the damage variables ω (denoted by Matzenmiller *et al.* as the "damage rule") have to allow either independent growth of the damage parameters or appropriate coupling between them; for example, damage growth in the matrix may not affect fibre damage, whereas fibre breakage causes damage growth in the matrix. Therefore, the following damage rule was proposed:

$$\dot{\omega} = \sum_i \phi_i \, q_i \tag{1.18}$$

The scalar functions $\phi_i(\sigma, \omega, \dot{\epsilon})$ control the amount of growth, while the vector-valued functions $q_i(\sigma, \omega)$ accommodated the coupling of growth for the individual

damage variables in the various damage modes. Matzenmiller et al. assumed rate-independent material behaviour to obtain the following relation for ϕ_i:

$$\phi_i = \gamma_i \left\langle \frac{\partial g_i}{\partial \epsilon} : \dot{\epsilon} \right\rangle \tag{1.19}$$

where for convenience the following notation is used:

$$\langle x : y \rangle = \begin{cases} x : y & \text{if } x : y > 0 \\ 0 & \text{if } x : y \leq 0 \end{cases}$$

The inner product between the strain rate $\dot{\epsilon}$ and the normal to the damage surface $\partial g / \partial \epsilon$ was used to ensure that damage growth occurred in the direction normal to the damage surface. The growth functions $\gamma_i(Y, \omega)$ are defined in terms of the thermodynamic forces Y:

$$\gamma_1(Y, \omega) = \alpha_{11_{e,t}} Y_{11}^{n_{11_{e,t}}}, \qquad \gamma_2(Y, \omega) = \alpha_{22_{e,t}} Y_{22}^{n_{22_{e,t}}} + \alpha_{12_{e,t}} Y_{12}^{n_{12_{e,t}}} \tag{1.20}$$

where the coefficients α_{ij} and exponents n_{ij} are used to adjust the growth functions to material data. As a result of the choice for the constitutive tensor by Matzenmiller et al., there is a direct mapping between the stresses, σ, and the thermodynamic forces, Y, which make the fitting of the growth functions to experimental data possible.

The vector-valued functions q_i are defined from the damage potentials $Q(Y, \omega)$ (each damage mode has a corresponding damage potential)

$$q_i = \frac{\partial Q_i}{\partial Y} \tag{1.21}$$

With all this, the final relation for the damage rule is:

$$\dot{\omega} = \sum_i \gamma_i \left(\frac{\partial Q_i}{\partial Y} \otimes \frac{\partial g_i}{\epsilon} \right) \dot{\epsilon} \tag{1.22}$$

where the symbol $\otimes$ stands for the outer (dyadic) tensor product.

When Matzenmiller *et al.* (1995) applied the above to a uniaxial tensile test in the fibre direction, they arrived at the following relation for the damage rule:

$$\dot{\omega}_{11} = \alpha_{11} \left(\frac{\epsilon_{11}}{S_{11}/E_{11}} \right)^{m-1} \frac{\dot{\epsilon}_{11}}{S_{11}/E_{11}} \tag{1.23}$$

The quotient S_{11}/E_{11} is replaced by the "nominal" failure strain ϵ_f. When α_{11} is chosen equal to $\frac{1}{e}(1-\omega_{11})$ and the resulting damage rule is integrated, the relation found for the damage variable ω_{11} is:

$$\omega_{11} = 1 - \exp\left[-\frac{1}{me} \left(\frac{\epsilon}{\epsilon_f} \right)^m \right] \tag{1.24}$$

This relation is similar to the Weibull distribution function and the same result may be derived from statistical mechanics by means of probability theory for the failure of a bundle of fibres with initial defects, subjected to the stress σ (Matzenmiller *et al.*, 1995; Krajcinovic, 1996). The stress σ and strain ϵ can be normalised with respect to the tensile strength S_{11} and the nominal failure strain ϵ_f to obtain

$$\frac{\sigma}{S_{11}} = \exp\left[-\frac{1}{me} \left(\frac{\epsilon}{\epsilon_f} \right)^m \right] \frac{\epsilon}{\epsilon_f} \tag{1.25}$$

The effect of progressive damage on the stiffness variables is given in Figure 1.11, where the stiffness reduction is visualised by a decreasing unloading stiffness. Figure 1.12 shows the effect the failure exponent m has on the post-failure behaviour: the post-failure strength decreases more rapidly with strain with increasing values for m and the post-failure model approaches the instantaneous failure model for high values of m. Williams and Vaziri (1995) implemented a version of the MLT model for shell elements in LS-DYNA3D.

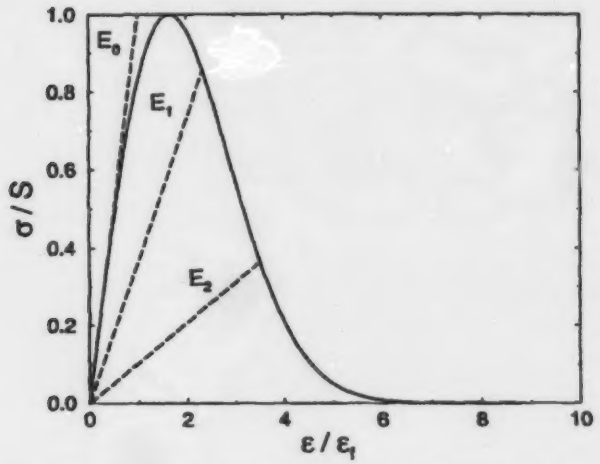

Figure 1.11: Progressive damage represented by decreasing unloading stiffness.

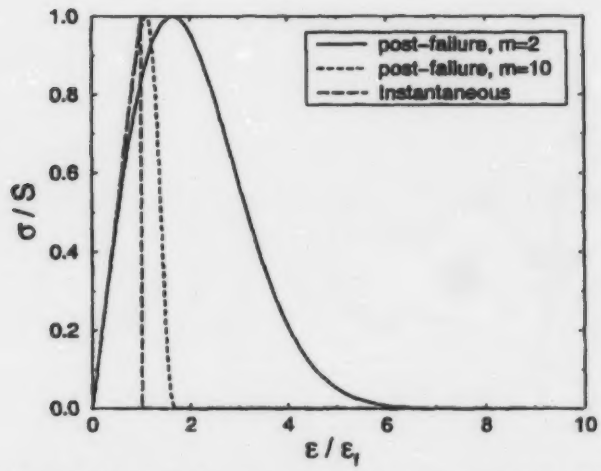

Figure 1.12: Effect of damage exponent m on post-failure behaviour.

Another interesting application of the CDM-theory to composites was taken by Daudeville *et al.* (1995), who used a continuum damage mechanics approach to model the onset of delamination and its propagation over a short distance in unidirectional carbon-epoxy laminates. They modelled the laminate at the meso-scale as a stacking of homogeneous layers connected by interfaces (Fig. 1.13).

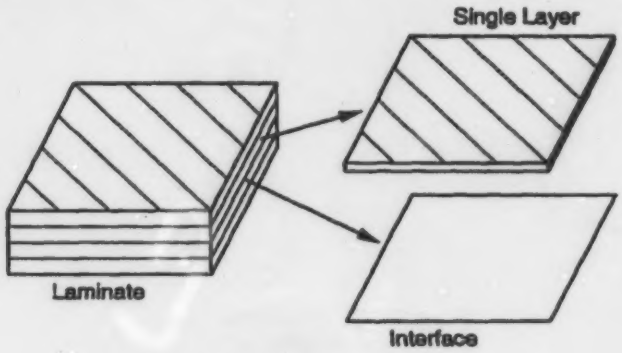

Figure 1.13: Laminate modelled at meso-scale as stacking of layers connected by interfaces Daudeville *et al.* (1995).

Damage modes incorporated at the single layer level are progressive transverse matrix cracking, brittle fracture of fibres, and debonding of the fibre-matrix interface. The damage state is assumed to be uniform in the layer thickness and the relative deteriorations in stiffness are considered as damage indicators. Experiments have shown that for the type of material used by Daudeville *et al.*, the only moduli modified by progressive damage (matrix micro-cracking and fibre-matrix debonding) were the transverse and in-plane shear moduli, E_{22} and G_{12}. A previously developed elastic-plastic material model including the above damage modes (Ladevèze and Le Dantec, 1992; Allix *et al.*, 1994) was used to describe the material behaviour of the layers.

The interface can be visualised as a two-dimensional medium with zero thickness which connects two adjacent layers. The interface ensures displacement and traction transfer between plies (layers). Its mechanical behaviour is assumed to be orthotropic and the directions of orthotropy are defined by the bisector of the fibre directions of the adjacent layers (Fig. 1.14).

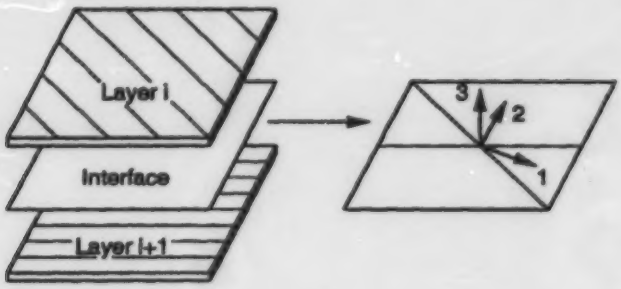

Figure 1.14: Interface coordinate system (Daudeville *et al.*, 1995).

The interface material behaviour is assumed to be elastic with damage (Allix and Ladevèze, 1992). The interface stiffness values are approximated by

$$k_1^0 = \frac{2G_{13}}{t}, \qquad k_2^0 = \frac{2G_{23}}{t}, \qquad k_3^0 = \frac{E_{33}}{t} \tag{1.26}$$

where t is the thickness of the resin rich zone between the laminates and G_{ij} and E_{33} are the elastic moduli of the resin (which are chosen equal to the homogenised layer moduli).

Delamination initiation and growth are represented by progressive damage in the interface (Allix and Ladevèze, 1992). Tensile-induced damage in the interface corresponds to Mode I fracture, while shear induced damage corresponds to modes II and III. A similar approach, using an interface with damage for delamination simulation, was applied by Schellekens and de Borst (1991).

1.6 Numerical Modelling of Delamination

This section discusses the numerical techniques that have been used to predict impact induced delaminations. A distinction is made between techniques applied for the prediction of delamination initiation and delamination growth.

1.6.1 Delamination Initiation

As was shown in Section 1.5.1, the most successful and, therefore, most commonly applied criteria for delamination initiation are based on the strength of materials approach. As a result, most numerical models for the prediction of delamination initiation are based on stress criteria. The finite element method is one of the most powerful numerical tools for the prediction of the time-dependent stress state and the complex failure behaviour of impacted composites.

Edlund (1993) used the following criterion in the explicit three-dimensional finite element code LS-DYNA3D to predict the onset of delamination:

$$\left(\frac{\sigma_{33}}{S_{33}}\right)^2 + \left(\frac{\sigma_{13}}{S_{13}}\right)^2 + \left(\frac{\sigma_{23}}{S_{23}}\right)^2 \geq 1 \qquad (1.27)$$

This criterion only predicts the onset of delamination and does not provide details concerning the size and growth of the delamination. Edlund (1993) did not compare his results with experimentally observed damage.

1.6.2 Delamination Growth

Energy-based linear elastic fracture mechanics has been extensively used for the numerical prediction of delamination growth in composites (Wang, 1980, 1983; Kim and Soni, 1986; Kim, 1991; Lu and Liu, 1991; Jensen, 1993; Hitchings *et al.*, 1994; Robinson *et al.*, 1995). In this approach, delamination growth is often predicted by

testing the strain energy release rate G in some criterion involving the critical strain energy release rate G_c of the material.

The strain energy release rate distribution along the delamination front can be calculated by the modified virtual crack closure technique (VCCT) (Rybicki and Kanninen, 1977). In this technique, the work required to close a delamination by a virtual amount of surface area δA is assumed to be equal to the strain energy released for the same amount of delamination extension. Using finite element techniques, the strain energy release rate can be expressed in terms of nodal displacements and nodal resultants:

$$G = \frac{1}{2\delta A}\sum_{i=1}^{n}\sum_{j=1}^{k}(F_j\Delta u_j)_i \tag{1.28}$$

where F_j are the nodal resultants (both nodal forces and moments), Δu_j are the relative displacement components between the upper and lower delamination surfaces (translational and rotational), and n and k are the number of nodes in the closing face and the number of degrees of freedom per node, respectively. The element surface area is denoted by δA.

Figure 1.15 shows a typical finite element representation of a crack. Equation 1.28 was implemented in a finite element code by Hitchings *et al.* (1994) and validated by Robinson *et al.* (1995) who compared simulations of a DCB test with experimental results. The numerical results were in reasonable agreement with the experimental data.

Some researchers have used the normal and shear components of the displacements and forces individually to calculate the strain energy release rate for modes I and II, $G_{I,II}$. The individual strain energy release rates are calculated as follows:

$$\begin{aligned} G_I &= \frac{F_z(W_c - W_d)}{2b\Delta a} \\ G_{II} &= \frac{F_y(V_c - V_d)}{2b\Delta a} \end{aligned} \tag{1.29}$$

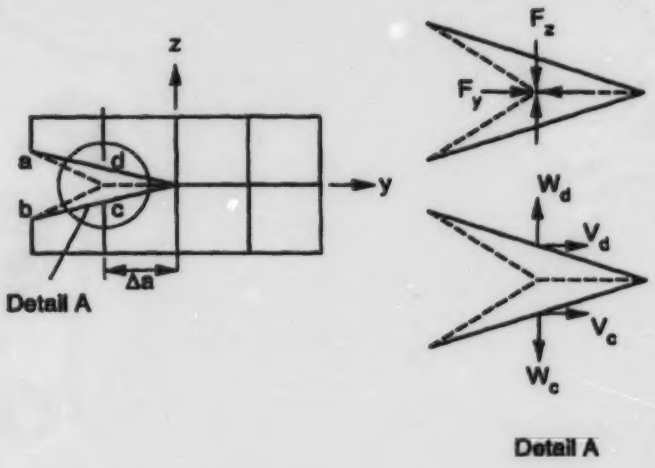

Figure 1.15: Finite element crack growth model (Majeed, 1995).

where Δa is the amount of crack extension, which is predicted using the relations $G_I = G_{Ic}$ and $G_{II} = G_{IIc}$. The displacements V and W are the sliding and opening displacements on the crack face, respectively. F_z and F_y are the forces in the z- and y-directions required to hold nodes c and d together. Sun and Jih (1990) and Jih and Sun (1994) used this technique in their finite element simulations of high mass/low velocity impact on laminated graphite/epoxy composites. Good agreement was found between measured and predicted crack lengths. The total strain energy release rate can be obtained by summing the individual components and can be verified using a global energy balance analysis.

Liu (1993) used the crack closure technique to predict delamination growth in cross-ply laminates subjected to drop weight impact. They used the following criterion to predict mixed mode fracture:

$$\left(\frac{G_I}{G_{Ic}}\right)^{\alpha} + \left(\frac{G_{II}}{G_{IIc}}\right)^{\beta} + \left(\frac{G_{III}}{G_{IIIc}}\right)^{\gamma} = E_d \qquad (1.30)$$

where it was assumed that G_{Ic}, G_{IIc}, and G_{IIIc} do not change with delamination

size. Based on a previous 2-D study by Liu, α=β=γ=1, since this provided the best fit to experimental data. Further, it was assumed that G_{IIc}=G_{IIIc}, because no value for G_{IIIc} was found in the literature. Delamination growth occurred when $E_d \geq 1$ at any point on delamination front. Delaminations were only allowed to grow into either circular or elliptical shape.

Simulations by Liu (1993) using the above criterion showed that the presence of initial matrix cracking prior to delamination growth significantly affected the growth of the delamination. The experimentally observed slender peanut shape of the delamination was not observed without the existence of a matrix crack. Models with a matrix crack were found to initiate delamination growth at a much earlier loading stage than models without initial matrix cracking. Once delamination propagated, it was found to grow along the direction of matrix cracking. Further, in laminate models containing an initial matrix crack, the total strain energy release rate G_t along delamination front was dominated by G_I. Without matrix cracking, modes II and II fracture dominated G_t along the delamination front.

Barsoum (1989) argued that "any good elastic analysis will show that one cannot obtain a pure Mode I or II at a laminate interface". Therefore, it is questionable whether using G_{Ic} and G_{IIc} is meaningful. Raju *et al.* (1988) showed that the values of G_I and G_{II} computed in finite element models are a function of the element size. This invalidates G_I and G_{II} as good candidates for use as material properties when calculated from an elastic finite element analysis. However, when the values of G_I and G_{II} are added numerically, then the total G is not a function of mesh refinement.

In a numerical study using the crack closure technique to compute the strain energy release rates, Lu and Liu (1991) found that for a 0/90 stacking sequence, the strain energy release rate was not constant along the delamination front. This resulted in anisotropic delamination growth, resembling the experimentally observed

peanut-shape. The highest strain energy release rate was found to coincide with the major material principal direction of the lamina beneath the interface.

Another fracture mechanics parameter often used in numerical simulations is the so-called J integral. This integral was originally proposed by Rice (1968) for homogeneous materials, but has later been extended for cracks in anisotropic materials (Wang *et al.*, 1980; Tsamasphyros, 1989; Chu and Hong, 1990). For linear elastic materials, J is equivalent to the strain energy release rate G. One of the major advantages of using the J integral is that it determines the energy release rate for cases where plasticity effects are not negligible, whereas the strain energy release rate G is only applicable in linear elastic cases. Just like G, the J-integral is mesh-independent.

1.7 Outline

The long-term goal of this research programme is to predict the injurious effects resulting from the impact of the backplane of a laminated helmet with the head. This report focuses on one aspect of this problem, that is the development of a model to predict the penetration and backplane deformation in ballistically impacted laminates. Ultimately, this model is required to accurately represent the backplane deformation and its interaction with the head. Since the finite element method is the most powerful numerical tool for the prediction of the dynamic deformation and damage behaviour of structures, the numerical model presented in this report was developed within a finite element framework.

Section 1.4 demonstrated that there are many similarities between the damage response resulting from drop weight and ballistic impacts. Both impact types were found to exhibit the same damage mechanisms (fibre failure, matrix crack, delam-

ination, punching failure). Since these damage modes closely interact during the impact event, the numerical model needs to be capable of accounting for these interactions. Section 1.5.3 showed that the Continuum Damage Mechanics (CDM) approach enables the prediction of the evolution of individual damage modes together with their interactions. CDM was therefore chosen as the approach for the numerical model presented in this report.

The details of the numerical model are outlined in Chapter 2. A distinction will be made between intralaminar and interlaminar damage. The intralaminar failure modes include in-plane tensile failure (fibre breakage and matrix cracking) and through-thickness failure (shear punching and crushing). The model incorporates the interactions between the various intralaminar damage modes. The interlaminar failure mode includes delamination, which is modelled with a discrete damageable interface inserted between layers of elements. This interface enabled the formation of a discrete delaminated backplane during the final stage of the laminate penetration process.

To assess the accuracy of this model, a series of ballistic impact tests were performed on woven Kevlar-29/phenolic laminated panels. Since it was shown in Section 1.4.2 that the response of ballistically impacted laminates depended highly upon the impact conditions, different types of projectiles with a range of impact velocities were considered. The results of the ballistic impact tests are presented in Chapter 3.

The accuracy and limitations of the numerical model are evaluated in Chapter 4 from simulations of the ballistic impact tests presented in Chapter 3. A general discussion of the findings from the presented research is given in Chapter 5. Conclusions and recommendations are presented in Chapters 6 and 7.

Chapter 2

Numerical Model

Traditional damage models for composite materials do not incorporate any residual load bearing capacity once the material is loaded beyond its strength (Hashin, 1980; Chang and Chang, 1987a). These models are generally referred to as instantaneous failure models, since the stiffness values related to the failure direction are instantaneously reduced to zero once the strength is exceeded in a particular direction.

However, composite materials generally exhibit some residual load bearing capacity once the loading surpasses the material strength. This residual load bearing capacity can be modelled with so-called post-failure models, which define a more gradual decrease in the material stiffness once its strength value has been exceeded. Recent work has shown that post-failure modelling can significantly improve damage predictions and reduce mesh sensitivity in models of transverse impacts on laminated composites (Majeed *et al.*, 1994; Straznicky *et al.*, 1995; Williams and Vaziri, 1995).

This chapter presents both an instantaneous and post-failure model, developed as part of this research, to predict the response of ballistically impacted laminated composites. The failure models were implemented in the explicit, non-linear three-dimensional finite element code LS-DYNA3D. A distinction was made between intralaminar and interlaminar failure modes, and each of this type of failure modes

was treated in a separate part of the software.

The intralaminar failure modes (fibre breakage, matrix cracking, through-thickness crushing and shear failure) were modelled within the element constitutive routines, implemented in a so-called user-defined material subroutine. The interlaminar failure mode included delamination, which was treated using discrete interfaces inserted between layers of elements, allowing the formation of a discrete delaminated backplane during the final stages of the laminate penetration process.

2.1 Constitutive Model

The compliance response of the composite laminate is given by:

$$\epsilon = C\,\sigma \tag{2.1}$$

where C is the orthotropic compliance matrix,

$$C = \begin{bmatrix} \frac{1}{E_{11}} & -\frac{\nu_{21}}{E_{22}} & -\frac{\nu_{31}}{E_{33}} & 0 & 0 & 0 \\ -\frac{\nu_{12}}{E_{11}} & \frac{1}{E_{22}} & -\frac{\nu_{32}}{E_{33}} & 0 & 0 & 0 \\ -\frac{\nu_{13}}{E_{11}} & -\frac{\nu_{23}}{E_{22}} & \frac{1}{E_{33}} & 0 & 0 & 0 \\ 0 & 0 & 0 & \frac{1}{G_{12}} & 0 & 0 \\ 0 & 0 & 0 & 0 & \frac{1}{G_{23}} & 0 \\ 0 & 0 & 0 & 0 & 0 & \frac{1}{G_{31}} \end{bmatrix} \tag{2.2}$$

with E denoting Young's modulus, ν is Poisson's ratio, and G is the shear modulus. The indices $_{1,2,3}$ denote the local material axes. Because of the symmetry properties of C, the following holds:

$$\frac{\nu_{ij}}{E_{ii}} = \frac{\nu_{ji}}{E_{jj}} \tag{2.3}$$

Jones (1975) argued that the parameters for a thermodynamically stable material must satisfy the following inequalities:

$$|\nu_{12}| < \left(\frac{E_{11}}{E_{22}}\right)^{1/2} \quad |\nu_{23}| < \left(\frac{E_{22}}{E_{33}}\right)^{1/2} \quad |\nu_{31}| < \left(\frac{E_{33}}{E_{11}}\right)^{1/2} \tag{2.4}$$

The stiffness matrix, S, is obtained by inverting the compliance matrix:

$$S = C^{-1} \tag{2.5}$$

Relation (2.5) was implemented in a user-defined material subroutine to transform the strains provided by LS-DYNA3D into stresses. Care was taken that the applied material parameters satisfied the inequalities in Equation (2.4).

2.2 Intralaminar Failure

The intralaminar failure modes included in-plane tensile failure (fibre breakage and matrix cracking) and through-thickness crushing and shear failure. Both instantaneous and post-failure models were developed as part of this research to predict the onset and growth of these failure modes. The intralaminar failure modes were implemented in a user-defined material subroutine.

2.2.1 Instantaneous Failure Model

A strain-based instantaneous failure model, similar to the failure models by Hashin (1980) and Chang and Chang (1987a,b), was developed for this project. The instantaneous failure model predicts in-plane tensile failure by relating either the longitudinal or transverse tensile strain to a corresponding critical strain. In case of uni-directional laminae this implies that longitudinal tensile failure represents fibre breakage and transverse tensile failure represents matrix cracking. For woven laminated composites, both longitudinal and transverse tensile failures correspond to

fibre breakage. In-plane tensile failure was predicted by the following criteria:

$$f_i = \left(\frac{\epsilon_{ii}}{\epsilon_{f_{ii}}}\right)^{m_i} - r_i \begin{cases} \geq 0 : \text{failure} \\ < 0 : \text{no failure} \end{cases} \tag{2.6}$$

where the subscript $i = 1, 2$ denotes the in-plane directions (longitudinal and transverse, respectively), ϵ_{ii} are the in-plane tensile strains, $\epsilon_{f_{ii}}$ the corresponding failure strains, m_i are the damage exponents, and r_i are the failure thresholds which are set equal to 1. When tensile failure occurs in the i-direction, all stresses related to that direction ($\sigma_{ij}, j = 1 - 3$) are set to zero instantaneously. In practice, the stresses were set to zero in 100 time steps to avoid numerical stability problems.

During ballistic impacts, the composite material in the impacted area will be compressed by the projectile. This will lead to high compressive stresses under the projectile and high transverse shear stresses in the surrounding area. When these stresses exceed their related strength values, the projectile will punch a hole in the material. In order to be able to determine the relative contributions of the compressive and shear punching failure modes, different failure criteria were used to predict each of the punching failure modes. Compressive punching failure was predicted by the following criterion:

$$f_3 = \left(\frac{\epsilon_{33}}{\epsilon_{f_{33}}}\right)^{m_3} - r_3 \begin{cases} \geq 0 : \text{failure} \\ < 0 : \text{no failure} \end{cases} \tag{2.7}$$

where ϵ_{33} is the through-thickness compressive strain, $\epsilon_{f_{33}}$ the corresponding failure strain, m_3 is the corresponding damage exponent, and r_3 is the failure threshold which was set equal to 1. Shear punching failure was predicted using the following

criterion:

$$f_4 = \left(\frac{\epsilon_{23}}{\epsilon_{f_{23}}}\right)^{m_4} + \left(\frac{\epsilon_{31}}{\epsilon_{f_{31}}}\right)^{m_4} - r_4 \begin{array}{l} \geq \\ < \end{array} \begin{array}{l} 0 : \text{failure} \\ 0 : \text{no failure} \end{array} \tag{2.8}$$

where ϵ_{23} and ϵ_{31} are the through-thickness shear strains, $\epsilon_{f_{23}}$ and $\epsilon_{f_{31}}$ the corresponding failure strains, m_4 is the damage exponent, and r_4 is the failure threshold set equal to 1. When either compressive or shear punching failure occurs, all stresses are set to zero and the element is deleted from the mesh to simulate the formation of a crater by the projectile.

The failure strains used in the above failure criteria can be obtained from the appropriate stress-strain relations for the composite laminate through:

$$\epsilon_{f_{ij}} = \frac{S_{ij}}{E_{ij}} \tag{2.9}$$

where S_{ij} represent the strength values and E_{ij} are the corresponding stiffness values (Young's or shear modulus).

2.2.2 Post-Failure Model

The post-failure model used in this research is based on a Continuum Damage Mechanics approach (see Section 1.5.3), which characterises the onset and growth of damage by a decrease in stiffness of the material (Kachanov, 1986; Krajcinovic, 1996). Matzenmiller *et al.* (1995) developed a continuum damage mechanics model for anisotropic damage in elastic-brittle fibre-reinforced composites. Williams and Vaziri (1995) first implemented a two-dimensional version of this model as a user-defined material subroutine in LS-DYNA3D. Since an accurate representation of the three-dimensional stress state is required for the prediction of impact induced delaminations, a three-dimensional damage model based on the model by Matzenmiller *et al.* (1995) was developed for this project.

A set of damage variables, ω_{ij}, was introduced to relate the onset and growth of damage to stiffness losses in the material. The effect of the damage variables on the material's stiffness can be seen in the compliance matrix C (see Equation 2.2):

$$C = \begin{bmatrix} \frac{1}{(1-\omega_{11})E_{11}} & -\frac{\nu_{21}}{E_{22}} & -\frac{\nu_{31}}{E_{33}} & 0 & 0 & 0 \\ -\frac{\nu_{12}}{E_{11}} & \frac{1}{(1-\omega_{22})E_{22}} & -\frac{\nu_{32}}{E_{33}} & 0 & 0 & 0 \\ -\frac{\nu_{13}}{E_{11}} & -\frac{\nu_{23}}{E_{22}} & \frac{1}{(1-\omega_{33})E_{33}} & 0 & 0 & 0 \\ 0 & 0 & 0 & \frac{1}{(1-\omega_{12})G_{12}} & 0 & 0 \\ 0 & 0 & 0 & 0 & \frac{1}{(1-\omega_{23})G_{23}} & 0 \\ 0 & 0 & 0 & 0 & 0 & \frac{1}{(1-\omega_{31})G_{31}} \end{bmatrix} \tag{2.10}$$

Similar to Matzenmiller *et al.* (1995), damage growth was predicted by:

$$\dot{\omega_{ij}} = \sum_{k=1}^{n_{fm}} g_k \, q_k \tag{2.11}$$

where n_{fm} is the number of failure modes, the scalar functions g_k control the amount of growth, and the vector-valued functions q_k indicate the coupling of growth between the individual damage variables in the various failure modes.

The same failure criteria as in the instantaneous failure model were used in the post-failure model. However, in the post-failure model the damage (failure) thresholds are no longer constants, but are continuously increasing functions with increasing damage. The damage thresholds in the post-failure model can be thought of as being similar to the yield strength in plasticity theory with hardening. Consequently, the corresponding failure criteria, f_k, can be represented as damage surfaces in strain space, similar to the yield surface in plasticity theory.

The post-failure model assumes linear elastic behaviour within the part of the strain space bounded by the damage thresholds. This means that both loading and unloading of the material are linear elastic as long as the damage thresholds are not exceeded. The non-linear material behaviour is captured by the damage functions, ω_i, in case of damage growth. Damage growth will occur when the strain path crosses the failure surface ($f_k = 0$) and the strain increment has a non-zero component in the direction of the normal to the damage surface. In mathematical form:

$$g_k = \gamma_k \left\langle \frac{\partial f_k}{\partial \epsilon}, \dot{\epsilon} \right\rangle \tag{2.12}$$

where

$$\langle x, y \rangle = \begin{cases} (x, y) & \text{if } (x, y) > 0 \\ 0 & \text{if } (x, y) \leq 0 \end{cases} \tag{2.13}$$

with $(,)$ denoting the inner product, and γ_k are growth functions.

With this we find the following for the scalar functions g_k:

$$g_k = \gamma_k m_k \left(\frac{\epsilon_{kk}}{\epsilon_{fkk}} \right)^{m_k - 1} \frac{\dot{\epsilon}_{kk}}{\epsilon_{fkk}} \tag{2.14}$$

Choosing

$$\gamma_k = \frac{1 - \omega_k}{m_k e} \tag{2.15}$$

leads to

$$g_k = \frac{1 - \omega_k}{e} \left(\frac{\epsilon_{kk}}{\epsilon_{fkk}} \right)^{m_k - 1} \frac{\dot{\epsilon}_{kk}}{\epsilon_{fkk}} \tag{2.16}$$

For the tensile failure modes (modes 1 and 2), the damage coupling vectors q_1 and q_2 are chosen such that tensile failure results in stiffness reduction in the loading direction and in all shear directions. For the punching failure modes (modes 3 and

4), the damage coupling vectors q_3 and q_4 are chosen such that all stiffness values are reduced as soon as damage grows in either of the two modes. In mathematical form the damage coupling vectors look as follows:

$$q_1 = \begin{bmatrix} 1 \\ 0 \\ 0 \\ 1 \\ 0 \\ 1 \end{bmatrix}, \quad q_2 = \begin{bmatrix} 0 \\ 1 \\ 0 \\ 1 \\ 1 \\ 0 \end{bmatrix}, \quad q_3 = q_4 = \begin{bmatrix} 1 \\ 1 \\ 1 \\ 1 \\ 1 \\ 1 \end{bmatrix} \tag{2.17}$$

With these damage coupling vectors, the following expressions for the damage variables are found:

$$\omega_{ij} = 1 - exp\left[\frac{-1}{m_k e}\left(\frac{\epsilon_{ij}}{\epsilon_{f_{ij}}}\right)^{m_k}\right] \tag{2.18}$$

The stiffness matrix, S, is updated according to changes in the damage variables ω_{ij}. A graphical representation of the effect of progressive damage on the stiffness variables and the effect of the damage exponent m was given in Figure 1.11 and Figure 1.12, respectively.

2.3 Interlaminar Failure

The interlaminar damage considered in this research consisted of delamination failure of adjacent laminae. Delamination failure was implemented using a discrete delamination interface connecting adjacent element layers.

2.3.1 Discrete Delamination Interface

The discrete delamination interface is based on the tie-break contact algorithm in LS-DYNA3D. A similar approach was undertaken by Hung *et al.* (1995), who modelled delamination in drop weight impacts with the LS-DYNA3D tie-break interfaces and their numerical results were in good agreement with experimental data.

The tie-break contact interface uses the penalty method to treat contact between two separate parts of a mesh. The penalty method is a numerical approach that can be visualised by normal interface springs between the contacting nodes and element surfaces (Figure 2.1).

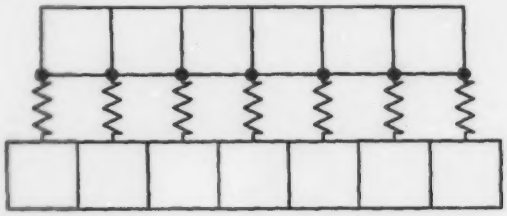

Figure 2.1: Penalty method visualised by interface springs between contacting nodes and element faces.

The discrete delamination interface is inserted between each ply of the laminate mesh. To avoid problems with initial contact, the plies are positioned a small distance apart (10 nm). The initial contact stiffness (interface spring stiffness) of the discrete delamination interface is automatically determined by the software from the

properties of the contacted element by:

$$E_{contact} = \alpha K \frac{A^2}{V} \tag{2.19}$$

where $E_{contact}$ is the contact stiffness, α the penalty scale factor, K the bulk modulus of the contacted material, and A and V the segment area and volume of the contacted element, respectively.

The discrete delamination interface incorporates two different modes: the delamination and penetration mode. The delamination mode is activated when tensile and/or shear forces exist in the interface. The penalty method (interface springs) resists these interface forces until the following failure criterion is exceeded:

$$f_{delam} = \left(\frac{\sigma_n}{S_n}\right)^2 + \left(\frac{\sigma_s}{S_s}\right)^2 - 1 \begin{cases} \geq 0 : \text{failure} \\ < 0 : \text{no failure} \end{cases} \tag{2.20}$$

where σ_n and σ_s are the normal and shear interface stresses, respectively, and S_n and S_s are the corresponding strength values. When the delamination criterion is exceeded, the interface is allowed to separate, simulating inter-ply cracking. In terms of the interface springs, once the interface has failed the springs no longer resist separation of the connected plies.

The delamination failure criterion defined in Equation 2.20 is similar to the delamination initiation criteria based on the Strength of Materials approach in Section 1.5.1. It was noted in Section 1.5 that the Strength of Materials approach is most suitable to predict delamination initiation and that a fracture mechanics approach is more appropriate to predict delamination growth. However, the extensive amount of work involved in the implementation of a fracture mechanics approach in the numerical model, together with the problems related to numerical fracture mechanics mentioned in Section 1.6.2 prevented us from pursuing further research

in this direction. Nevertheless, using a fracture mechanics approach to predict delamination growth in the numerical model definitely deserves further attention in the future.

Modifications were made to the original discrete delamination release mechanism. Originally, the discrete delamination forces were immediately set to zero once the discrete delamination criterion was exceeded. This instantaneous release of the interface can lead to numerical instabilities. Two additional release mechanisms were implemented to release the discrete delamination interface more gradually.

One approach reduced the discrete delamination forces to zero in 100 time steps, while the other approach used a post-failure approach similar to the one outlined in Section 2.2.2 for the post-failure intralaminar response. The post-failure release mechanism relates the discrete delamination interface forces, F_n and F_s, to the relative displacements between the tied nodes, d_n and d_s, as follows:

$$\text{normal:} \quad F_n = (1 - \omega_{tb_n})\, E_{contact}\, d_n \qquad (2.21)$$
$$\omega_{tb_n} = 1 - \exp\left[\frac{-1}{m_{delam}\, e}\left(\frac{d_n}{d_{f_n}}\right)^{m_{delam}}\right]$$

$$\text{shear:} \quad F_s = (1 - \omega_{tb_s})\, K\, d_s \qquad (2.22)$$
$$\omega_{tb_s} = 1 - \exp\left[\frac{-1}{m_{delam}\, e}\left(\frac{d_s}{d_{f_s}}\right)^{m_{delam}}\right]$$

where $E_{contact}$ is the interface contact stiffness defined in Equation 2.19, the subscripts $_{n,s}$ denote the normal and shear components of the interface forces and relative displacements, and $d_{f_{n,s}}$ are the critical interface displacement values, defined as

$$d_{f_n} = \frac{S_n}{K} \qquad (2.23)$$
$$d_{f_s} = \frac{S_s}{K}$$

where S_n and S_s are the interface normal and shear strength, respectively.

The penetration mode of the delamination interface is activated when the nodes in the interface penetrate the opposing elements. The penalty method detects this penetration and moves the penetrating nodes back out of the elements. In other words, the interface springs push the nodes back out of the penetrated elements. The penetration mode of the delamination interface remains active once the interface has failed in the delamination mode. This way, the delaminated plies are prevented from penetrating each other.

In Section 2.2.1 it was mentioned that the elements that fail in either the compressive or shear punching failure mode are deleted from the mesh to simulate the formation of a crater by the projectile. Modifications were made to the original tie-break interface to ensure that the contact definitions in the discrete delamination interface were properly updated when elements are deleted.

2.4 Model Description

Finite element models were created for flat panels fabricated from woven Kevlar-29/phenolic laminates. The finite element models were build using I-DEAS Master Series 6. The flat panels were used in both the numerical and experimental analyses as a simplified substitute for ballistic helmets. The planar dimensions of the laminated panels were 101.6x152.4 mm (4x6 inches) and the panel was 9.5 mm thick. The panels consisted of 19 layers, each 0.5 mm thick.

Figure 2.2 shows the finite element mesh of the woven Kevlar-29 laminated panels. The panel mesh also consists of 19 layers and adjacent layers were connected by a discrete delamination interface to model the initiation and growth of impact induced delaminations. Initially, each layer contained only one element over its

thickness. The panel mesh consisted entirely out of 8-node brick elements with single point (reduced) integration. To reduce computational time, only one-quarter of the problem was modelled utilising symmetry.

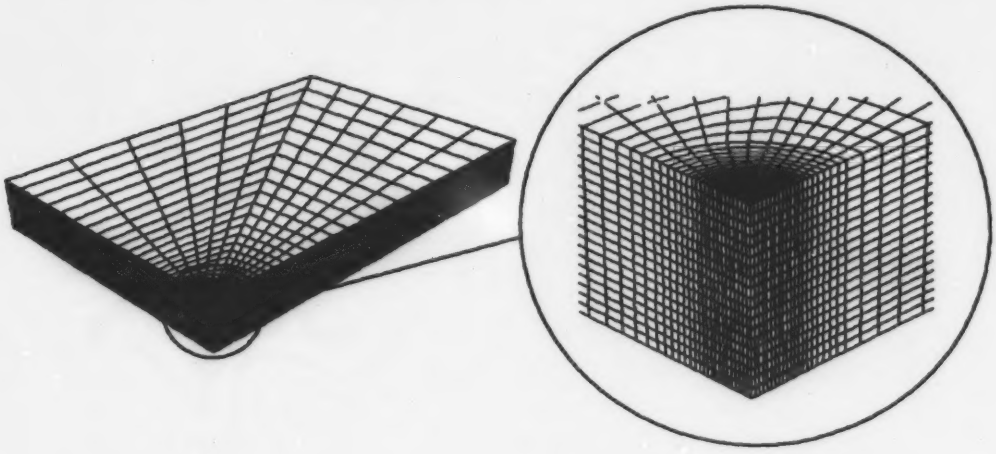

Figure 2.2: Finite element model of the woven Kevlar-29 laminated panel

Four different types of projectiles were used to determined the effects of projectile characteristics on the impact response of woven Kevlar-29/phenolic laminates. Fragment Simulation Projectiles (FSP) are commonly used to assess the ballistic protection provided by composite body armour. The laminated panels were impacted by both .22 and .30 calibre chisel nose FSP's (MIL-P46593).

Figure 2.3 shows the .22 calibre FSP dimensions and Figure 2.4 the finite element mesh developed for the simulations. The dimensions of the .30 calibre FSP are given in Figure 2.5 and its finite element mesh is given in Figure 2.6. The FSP's were fabricated using 4340 steel and heat treated to 29 HRc. The .22 calibre FSP's weighed 1.1 gram, whereas the .30 calibre FSP's weighed 2.8 gram.

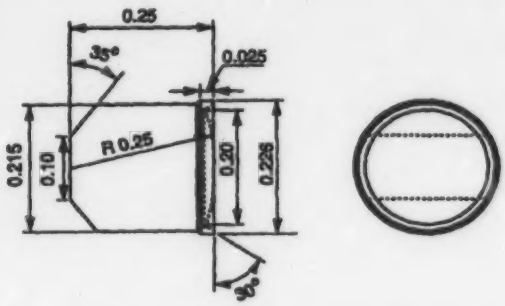

Figure 2.3: .22 calibre FSP dimensions (inches)

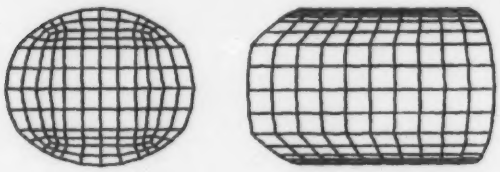

Figure 2.4: .22 calibre FSP finite element mesh

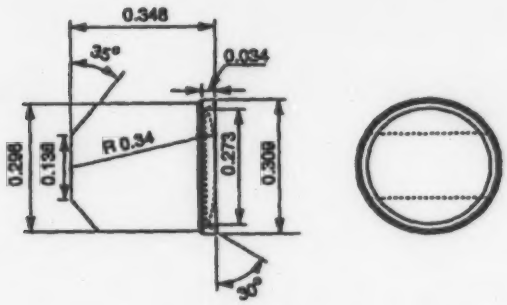

Figure 2.5: .30 calibre FSP dimensions (inches)

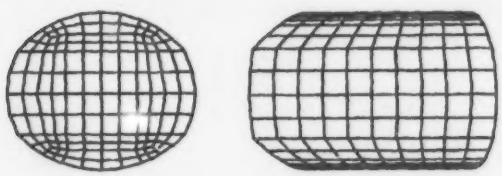

Figure 2.6: .30 calibre FSP finite element mesh

In addition to the FSP's, two types of cylindro-conical projectiles were used. These projectiles differed in tip cone angle. The sharp-nose projectiles had a tip cone angle of 37°, whereas the flat-nose projectiles had a 120° tip cone angle. Both cylindro-conical projectiles had a nominal weight of 13.2 gram, were manufactured from 4340 steel and hardened to 30 HRc. The nominal dimensions of the cylindro-conical projectiles are given in Figure 2.7. The meshes created for the simulations with the cylindro-conical projectiles are given in Figure 2.8.

(a) sharp-nose (b) flat-nose

Figure 2.7: Cylindro-conical projectile dimensions (mm)

(a) sharp-nose (b) flat-nose

Figure 2.8: Cylindro-conical projectile finite element meshes

Automatic surface-to-surface eroding contact interfaces were defined between the target (panel) and the projectile. This contact interface automatically updates the contacting surfaces in case of element erosion instigated by element failure in either of the two through-thickness failure modes (compression or shear). The automatic eroding contact interface facilitates crater formation by the penetrating projectile.

2.5 Material Properties

2.5.1 Kevlar laminates

The ballistic panels tested in this study were made of woven Kevlar-29 fabric, embedded in a phenolic resin. Material properties for the woven Kevlar laminates were obtained from data published in the literature. Limited data was found on the material properties for Kevlar-29. A larger amount of data was found available on Kevlar-49, which is mainly used in structural applications. Kevlar-49 has a higher modulus than Kevlar-29, but the energy absorption capabilities of Kevlar-29 are superior.

Tables 2.1-2.3 give an overview of the published data for Kevlar-29 and Kevlar-49. Tables 2.1 summarises the elastic properties for Kevlar fibres, including the tensile stiffness E_t, tensile strength S_t, and strain at tensile failure ϵ_f. The tensile stiffness values for each of the fibres obtained from different sources were generally found to be consistent, with the tensile stiffness of Kevlar-49 fibres about twice that of Kevlar-29 fibres. This explains why Kevlar-49 fibres are mainly used in structural applications. The published data for the tensile strength was found to vary considerably for both types of fibres. On average, the tensile failure strain values for Kevlar-29 fibres were found to be higher than those for Kevlar-49 fibres.

Table 2.1: Elastic properties for Kevlar fibres

Reference	Kevlar	E_t [GPa]	S_t [GPa]	ϵ_f [%]	ρ [g/cm^3]
Galasso (1989)	29	62	3.4	4.0	1.44
Agarwal and Broutman (1990)	29	62	2.760	3.0-4.0	1.44
Zhu *et al.* (1992b,a)	29	62	2.758	4.0	1.44
Andrews *et al.* (1997)	29	94	2.5	2.5	–
Galasso (1989)	49	131	3.4	2.4	1.45
Agarwal and Broutman (1990)	49	124	3.62	2.0-8.0	1.44
Zhu *et al.* (1992b,a)	49	125	2.8-3.6	2.4	1.44
Atallah and Galiotis (1993)	49	124	2.8	2.5	–
Hill and Okoroafor (1994)	49	110	2.509	2.45	–
Nath and Fenner (1996)	49	115	3.6	2.9	–
Young *et al.* (1996)	49	120	2.6	2.2	–
Andrews *et al.* (1997)	49	124	2.3	1.8	–

E_t: Fibre Tensile Modulus

S_t: Tensile Strength

ϵ_f: Failure Strain

ρ: Density

Table 2.2 gives an overview of the properties of woven fabric-reinforced Kevlar composite laminates, such as fibre volume fraction V_f, in-plane tensile stiffness $E_{11,22}$ (which are assumed to be equal for woven fabric laminates), in-plane shear modulus G_{12}, and through-thickness compressive stiffness E_{33}. A limited amount of data was obtained.

Different resins were used by the various sources in Table 2.2, resulting in varying material properties. Phenolic resins are commonly used in ballistic protection applications due to their superior fire-retardant and flammability properties compared to polyester and epoxy resins (Charalambides and Williams, 1995; Brown and Mathys, 1997). However, the mechanical properties of phenolic resins are inferior

Table 2.2: Elastic properties for woven Kevlar laminates

Reference	Kevlar	Resin	V_f [%]	$E_{11,22}$ [GPa]	E_{33} [GPa]	G_{12} [GPa]	ν_{12} [-]	$\nu_{31,32}$ [-]	ρ [g/cm^3]
Zhu et al. (1992a,b)	29	polyester	55.0	18.5	static: 1.47 dynamic: 6.0	0.77	0.25	–	1.23
Langlie and Cheng (1989)	49	phenolic	–	39.9	3.9	–	0.25	0.33	–
Want et al. (1995)	49	epoxy	40.0	22.1	–	–	–	–	–

V_f: Fibre Volume Fraction

$E_{11,22}$: In-Plane Tensile Moduli

E_{33}: Through-Thickness Compressive Modulus

static: quasi-static, $\dot{\epsilon} = 0.0027 - 0.13/s$

dynamic: Hopkinson Bar, $\dot{\epsilon} = 1500 - 2000/s$

G_{12}: In-Plane Shear Modulus

ν_{ij}: Poisson's Ratios

ρ: Density

to those of polyester and epoxy resins (Brown and Mathys, 1997). Consequently, the structural properties of phenolic resin-based composites are lower than those of composites based on polyester and epoxy resins.

Table 2.3 gives the published strength data for woven fabric-reinforced Kevlar laminates. A limited amount of data was found with varying properties, especially for the in-plane tensile strength values, $S_{11,22}$, and the delamination strength, S_{delam}. The differences might be caused by variations in fibre volume fraction, resin properties, or differences in the applied experimental techniques.

Table 2.3: Strength properties for woven Kevlar laminates

Reference	Kevlar	Resin	V_f [%]	$S_{11,22}$ [MPa]	$S_{23,32}$ [MPa]	S_{delam}
Zhu *et al.* (1992b,a)	29	polyester	55.0	–	–	G_{Ic}: 0.455±0.050 [kN/m]
Chen and Jang (1995)	29	epoxy	54.0	–	–	ILSS: 28.39±1 34 [MPa]
Brown and Mathys (1997)	29	phenolic	65.3	–	–	ILSS: 8.6±0.2 [MPa]
Langlie and Cheng (1989)	49	phenolic	–	1,086	543	ILTS: 34.5 [MPa]
Briscoe *et al.* (1993)	49	epoxy	–	–	–	G_{Ic}: 1.0-2.1 [kN/m]
Wang *et al.* (1995)	49	epoxy	40.0	388	–	G_{Ic}: 1.85 [kN/m] ILSS: 24.1 [MPa]

$S_{11,22}$: In-Plane Tensile Strength
E_{33}: Through-Thickness Shear Strength
S_{delam}: Delamination Strength
ILSS: Interlaminar Shear Strength
ILTS: Interlaminar Tensile Strength

Mechanical characterisation of the dynamic (and quasi-static) properties of the laminates used for the ballistic impact tests was not undertaken as part of this study. Instead, the published values given in Tables 2.1-2.3 were used to determine starting values for the data required by the numerical material model. The adopted values for the numerical model are summarised in Table 2.4 and Table 2.5. The values of $S_{11,22}$, S_{33}, S_{12}, and $G_{23,31}$ were based on measured values in Tables 2.1-2.3 and failure strains $\epsilon_{11,22} = 0.1$, $\epsilon_{33} = 0.2$, $\epsilon_{12} = 0.1$, and $\epsilon_{23,31} = 0.1$, respectively. The effects of the individual material properties on the laminate's impact response will be discussed in section 2.6.

Table 2.4: Elastic properties adopted for woven Kevlar in numerical model

$E_{11,22}$ [GPa]	E_{33} [GPa]	ν_{21} [-]	$\nu_{31,32}$ [-]	G_{12} [GPa]	$G_{23,31}$ [GPa]	ρ [g/cm^3]
18.5	6.0	0.25	0.33	0.77	5.43	1.23

Table 2.5: Strength properties adopted for woven Kevlar in numerical model

$S_{11,22}$ [MPa]	S_{33} [MPa]	S_{12} [MPa]	$S_{23,31}$ [MPa]	S_n [MPa]	S_s [MPa]
1850.0	1200.0	77.0	543.0	34.5	9.0

2.5.2 Projectiles

The projectiles used in this study were manufactured from 4340 steel. An elastic-plastic material model with isotropic hardening was used to model the projectiles. The material parameters used for the projectiles are given in Table 2.6.

Table 2.6: Material properties adopted for projectiles

E [GPa]	ν [-]	S_y [MPa]	H [MPa]
206.8	0.3	1034.2	685.0

E: Young's Modulus

ν: Poisson's Ratio

S_y: Yield Strength

H: Hardening Modulus

2.6 Effects of Model Parameters on the Ballistic Response of the Panel Model

This section presents the results of a parametric study, in which the effects of the model characteristics on the predicted impact response were studied. The parametric study analysed the differences between the instantaneous and post-failure models, the effects of the material parameters, and the mesh sensitivity of the model response. Only simulations of a 1.1 gram FSP impacting a woven Kevlar-29/phenolic laminated panel at 400 m/s were considered in this study.

2.6.1 Instantaneous vs. Post-Failure Model Response

Figure 2.9 presents the sequence of events occurring in a panel mesh utilising the instantaneous failure model with the material properties given in Tables 2.4 and 2.5. The plot at $t = 25\ \mu s$ shows the initial events of the FSP forming a crater in the panel and the initiation of delaminations in the impacted area. The crater was formed by the deletion of elements that failed in either the through-thickness compressive or shear punching failure mode. Delamination can be seen to occur both adjacent to and ahead of the advancing FSP. The delaminations ahead of the FSP are thought to be caused by reflected stress waves induced by the FSP impact. At $t = 100\ \mu s$, the FSP is about to completely perforate the panel. The plot at $t = 200\ \mu s$ shows the FSP exiting at the bottom of the panel.

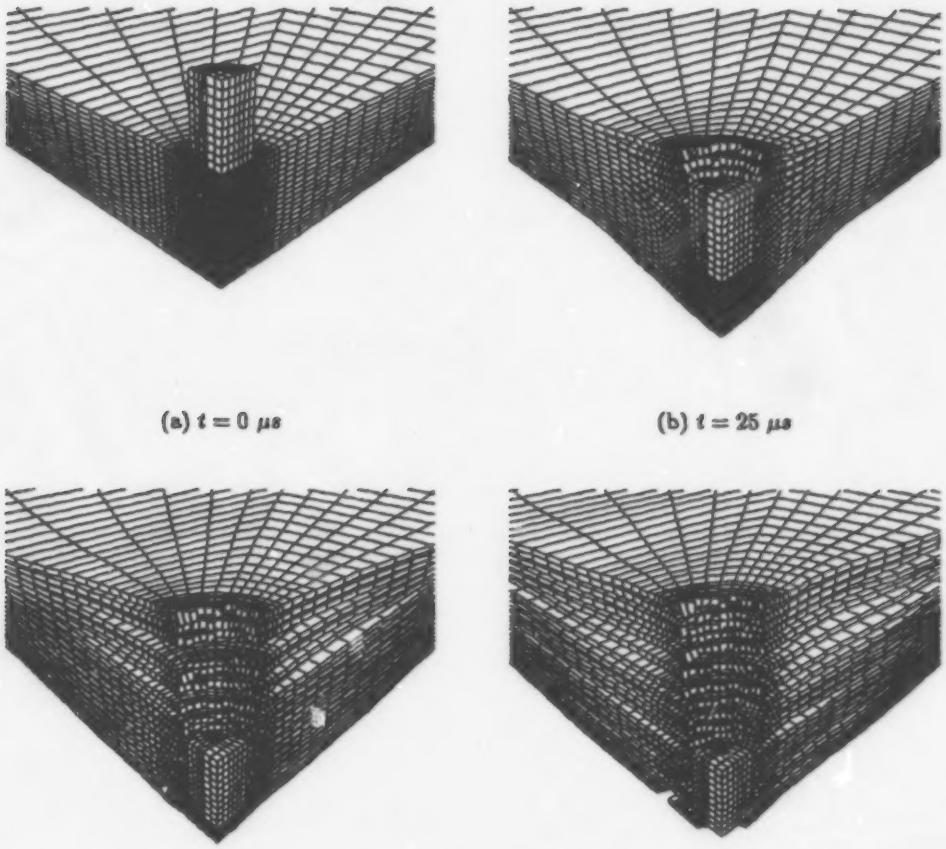

(a) $t = 0\ \mu s$ (b) $t = 25\ \mu s$

(c) $t = 100\ \mu s$ (d) $t = 200\ \mu s$

Figure 2.9: Sequence of deformed mesh plots using the instantaneous failure model.

Figure 2.10 shows the sequence of events occurring in a panel utilising the post-failure model with the material properties given in Tables 2.4 and 2.5. The plot at $t = 25\ \mu s$ is similar to the one found for the instantaneous failure model shown in Figure 2.9(b). However, at $t = 100\ \mu s$ the FSP has not penetrated the panel as far as was seen for the instantaneous failure model (Figure 2.9(c)). The plot at $t = 200\ \mu s$ shows that for the post-failure model, the FSP was sufficiently decelerated

that it was no longer capable of perforating the remainder of the panel. However, the remaining kinetic energy of the FSP causes it to push the backplane further down, resulting in larger delaminations at the backplane than were seen for the instantaneous failure model (Figure 2.9(d)).

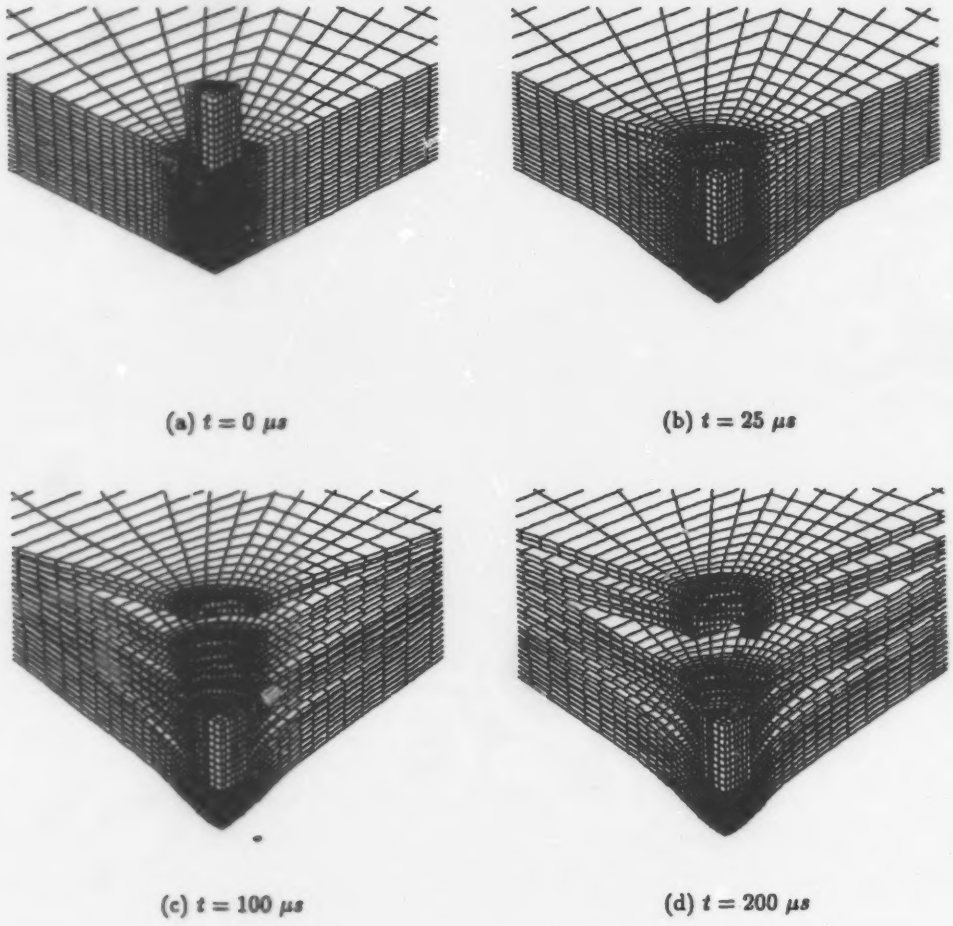

(a) $t = 0\ \mu s$ (b) $t = 25\ \mu s$

(c) $t = 100\ \mu s$ (d) $t = 200\ \mu s$

Figure 2.10: Sequence of deformed mesh plots using the post-failure model with the standard material properties.

The differences in the predicted response between the instantaneous and post-failure model are summarised in Figure 2.11. Figure 2.11(a) shows that the velocity-time histories do not differ much for the instantaneous and post-failure model. The figure further shows that the FSP velocity for the instantaneous failure model reduces to zero, indicating that the FSP just perforated the panel.

However, the differences in backplane displacement in Figure 2.11(b) are significant. The figure shows the displacement of the centre node of the backplane. The curve for the instantaneous failure model ends at the time of backplane perforation. The backplane displacement was much smaller in case the instantaneous failure model was used than was found with the post-failure model. The impact velocity of 400 m/s is well below the ballistic limit, which is about 600 m/s. Therefore, the post-failure model provides a more realistic prediction than the instantaneous failure model.

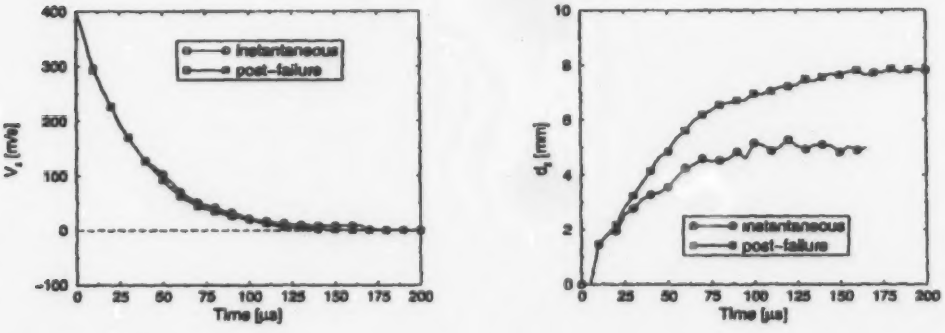

(a) FSP velocity-time history

(b) Backplane displacement-time history

Figure 2.11: Differences in response between instantaneous and post-failure models.

2.6.2 Effect of Material Parameters

In-plane Material Parameters

The effects of the in-plane tensile stiffness properties on the model response are presented in Figure 2.12. The figure indicates that increasing the in-plane tensile stiffnesses increased the ballistic resistance of the panel model for both the instantaneous and post-failure model, since the FSP velocities and backplane displacements were decreased. The effects were the most significant for the instantaneous failure model, where the panel was able to stop the projectile when the in-plane tensile stiffnesses were doubled.

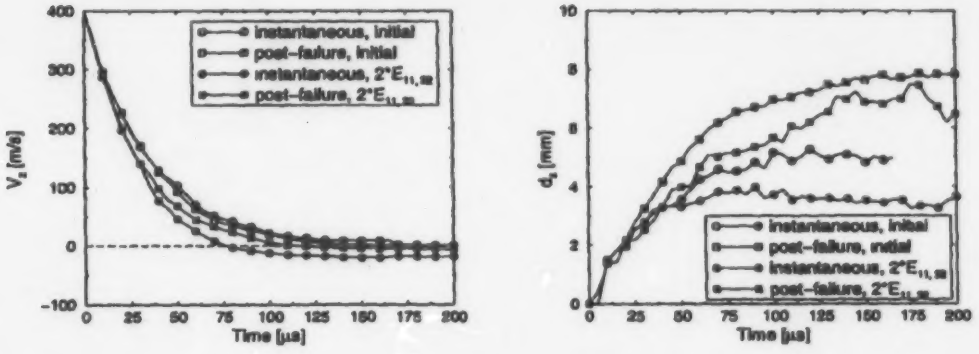

(a) Effects on FSP velocity.

(b) Effects on backplane displacement.

Figure 2.12: Comparison between the instantaneous and post-failure model of the effects of the in-plane tensile stiffnesses.

According to Equation 2.9, increasing the stiffness will result in a decrease in the failure strain, which leads to fibre breakage at lower strains under the same loading conditions. Figure 2.12 indicates that the increased in-plane stiffness has a more dominant effect than the lower resistance to fibre breakage.

Figure 2.13 presents the effects of the in-plane tensile strength properties on the simulated panel response. The figure shows that perforation occurred for both failure models when the in-plane tensile strength was increased, indicating that the ballistic resistance was reduced. In case of the post-failure model, the backplane was just perforated, resulting in extensive backplane displacement. For the instantaneous failure model, backplane perforation was observed to occur earlier in the impact event when the in-plane tensile strength was increased. However, the maximum backplane displacement was similar to that found for the initial strength properties.

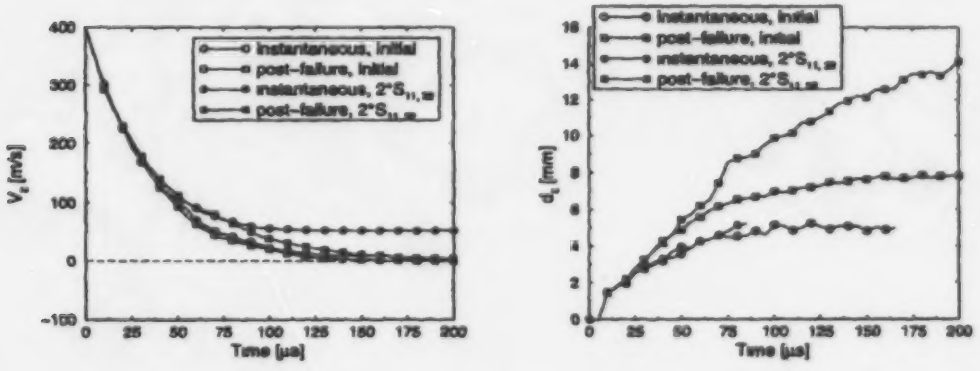

(a) Effects on FSP velocity. (b) Effects on backplane displacement.

Figure 2.13: Comparison between the instantaneous and post-failure model of the effects of the in-plane strength properties.

The combined effects of the in-plane tensile stiffness and strength on the predicted model response is given in Figure 2.14. Comparison of Figure 2.14(a) with Figures 2.13(a) and 2.12(a) shows that the response in this case was similar to that found when only the in-plane tensile stiffness was increased, especially for the instantaneous failure model.

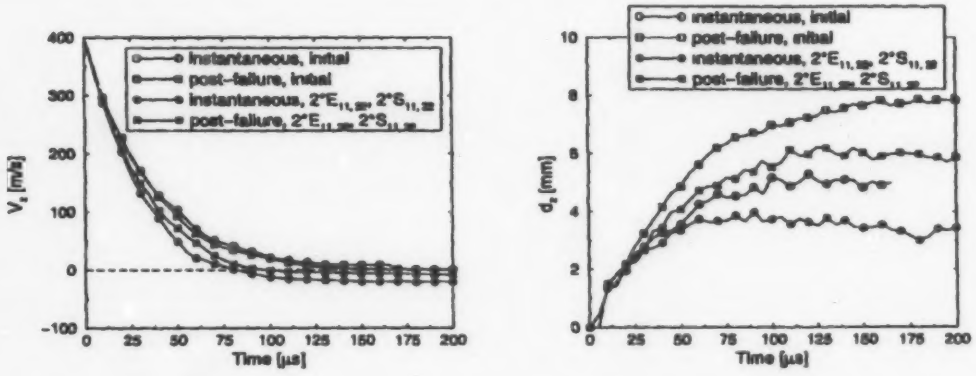

(a) Effects on FSP velocity.

(b) Effects on backplane displacement.

Figure 2.14: Comparison between the instantaneous and post-failure model of the combined effects of the in-plane stiffness and strength properties.

Through-Thickness Material Parameters

Figure 2.15 compares the effects that the through-thickness compression stiffness properties have on the predicted panel response for the instantaneous and post-failure models. As can be inferred from Equation (2.9), doubling the modulus is equivalent to halving the failure strain, ϵ_f. Consequently, doubling the modulus lowers the material resistance to punching failure. Figure 2.15 shows that the through-thickness compressive modulus has a stronger effect on the backplane deformation when the instantaneous failure model is used: backplane displacement is smaller and the backplane is completely perforated at an earlier stage in the impact event.

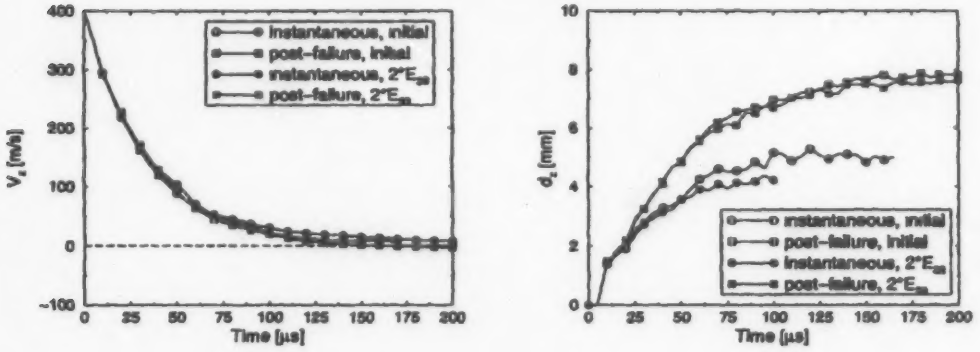

(a) Effects on FSP velocity.

(b) Effects on backplane displacement.

Figure 2.15: Comparison between the instantaneous and post-failure model of the effects of the through-thickness compression stiffness.

The effect of doubling the through-thickness shear moduli on the response of the model is given in Figure 2.16. The effects of the transverse shear stiffnesses were found to be much more severe than for the transverse compressive moduli (Figure 2.15). The ballistic resistance of the panel was decreased drastically and backplane perforation occurred for both the instantaneous and post-failure models.

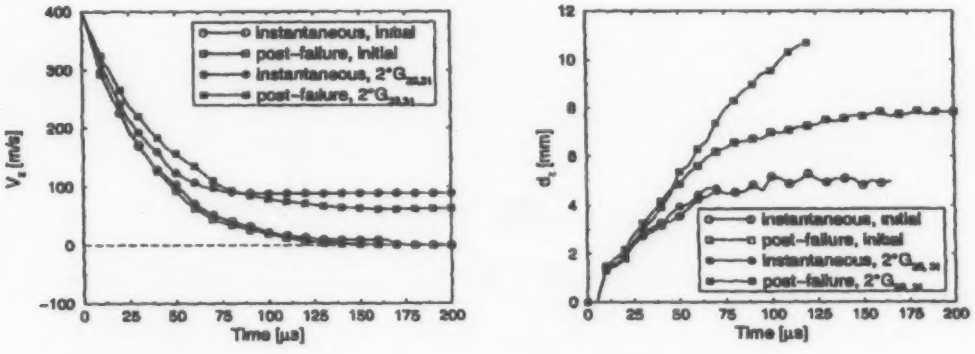

(a) Effects on FSP velocity.

(b) Effects on backplane displacement.

Figure 2.16: Comparison between the instantaneous and post-failure model of the effects of the through-thickness shear stiffness.

Figure 2.17 compares the effects that doubling the through-thickness compressive strength has on the predicted response for the instantaneous and post-failure treatments. The effect of the transverse compressive strength was seen to be small, at least for the range of S_{33} considered. The through-thickness compressive strength is likely overwhelmed by the large volume changes ahead of the projectile. An equation of state relating the volume changes to the applied compressive loading might be required.

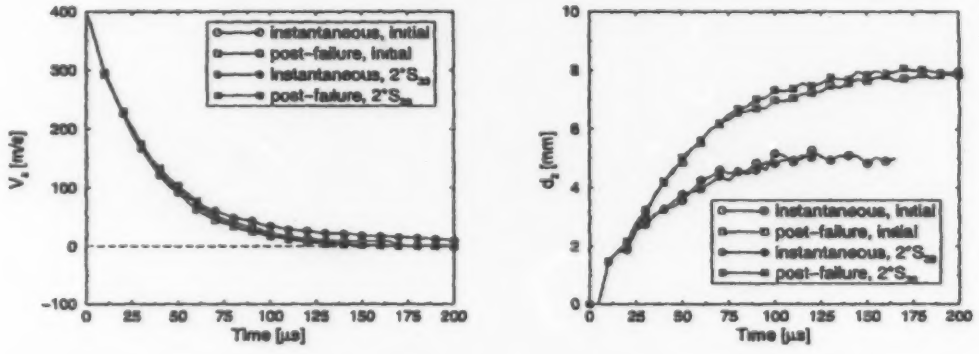

(a) Effects on FSP velocity. (b) Effects on backplane displacement.

Figure 2.17: Comparison between the instantaneous and post-failure model of the effects of the through-thickness compression strength.

The effect of increased transverse shear strength (S_{23}, S_{31}) was more significant, as can be seen in Figure 2.18. Doubling the through-thickness shear strengths resulted in a considerable drop in the projectile velocity (Figure 2.18(a)). In fact, Figure 2.18(b) shows that doubling the through-thickness shear strength in the instantaneous failure model enabled the panel mesh to prevent complete perforation by the projectile. Since the projectile was decelerated much faster when the through-thickness shear strength was increased, the kinetic energy of the projectile was smaller, resulting in a smaller backplane displacement.

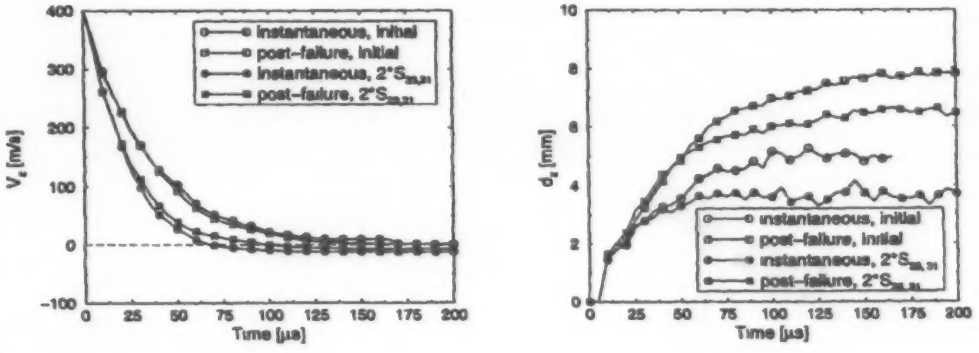

(a) Effects on FSP velocity.

(b) Effects on backplane displacement.

Figure 2.18: Comparison between the instantaneous and post-failure model of the effects of the through-thickness shear strengths.

Figure 2.19 shows the combined effects of changes in the through-thickness compressive stiffness and strength on the predicted FSP velocity-time history and the backplane displacement-time history. Doubling both the stiffness and strength is equivalent to doubling the stiffness while keeping the failure strain constant. Figure 2.19 shows that the effects are similar to those seen in Figure 2.15, where only the compressive stiffness was increased.

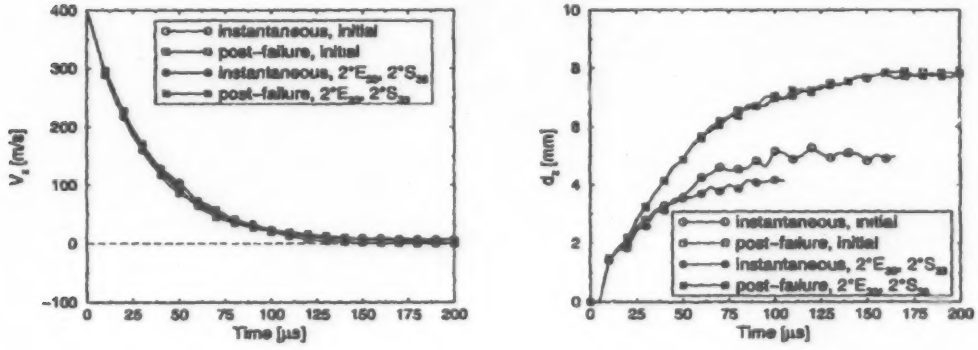

(a) Effects on FSP velocity. (b) Effects on backplane displacement.

Figure 2.19: Comparison between the instantaneous and post-failure model of the combined effects of the through-thickness compression stiffness and strength.

This behaviour of the post-failure model is perhaps counter-intuitive since one would expect that increasing the compressive stiffness while keeping the failure strain constant would lead to an increased resistance to penetration. However, the higher resistance to compressive punching failure might result in a change in failure mode to shear punching, which could be an explanation for the results seen in Figure 2.19.

Increasing both the through-thickness shear stiffness and strength increases the penetration resistance, as can be seen in Figure 2.20. For both the instantaneous and post-failure models, the increase in penetration resistance was similar to that seen in Figure 2.18, where only the through-thickness shear strength was doubled.

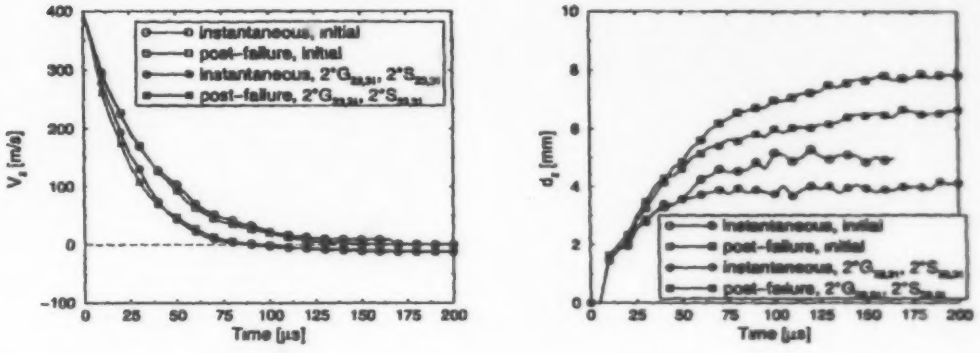

(a) Effects on FSP velocity.

(b) Effects on backplane displacement.

Figure 2.20: Comparison between the instantaneous and post-failure model of the combined effects of the through-thickness shear stiffness and strength.

2.6.3 Effect of Damage Parameters

Intralaminar Damage

Figure 2.21 presents the effects of the damage parameters m_i on the model response in case the instantaneous failure model is utilised. Only the damage exponent associated with through-thickness shear failure, m_4, was found to have an effect. A decrease in this damage exponent resulted in a reduction in the ballistic resistance of the panel model.

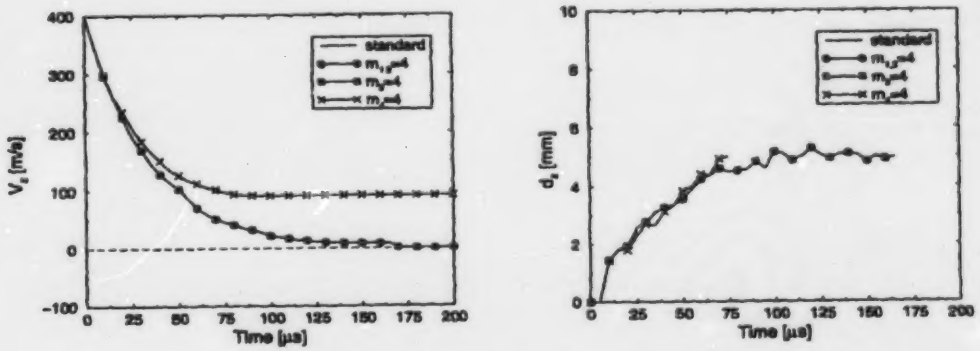

(a) Effects on FSP velocity.

(b) Effects on backplane displacement.

Figure 2.21: Effects of the damage exponents m_i for the instantaneous failure model.

Figure 1.12 shows that the post-failure model responds differently to changes in the various damage exponents, but the differences are not very large. Figure 1.12 showed that a decrease in m results in a more gradual decrease in the post-failure strength. The damage exponent related to the through-thickness shear failure was found to have the largest effect in Figure 2.22(b), resulting in the smallest backplane displacement.

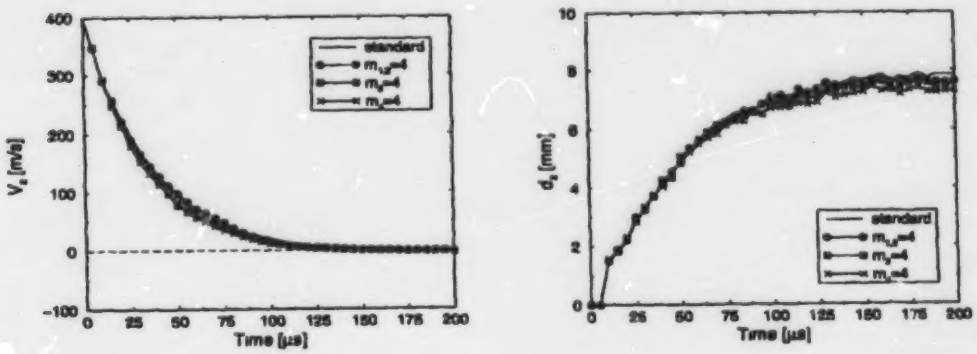

(a) Effects on FSP velocity.

(b) Effects on backplane displacement.

Figure 2.22: Effects of the damage exponents m_i for the post-failure model.

Interlaminar Damage

Doubling either the delamination normal or shear strength for the instantaneous failure model resulted in a lower ballistic resistance, as can be seen in Figure 2.23. On the other hand, doubling the delamination normal and shear strength simultaneously improved the ballistic resistance.

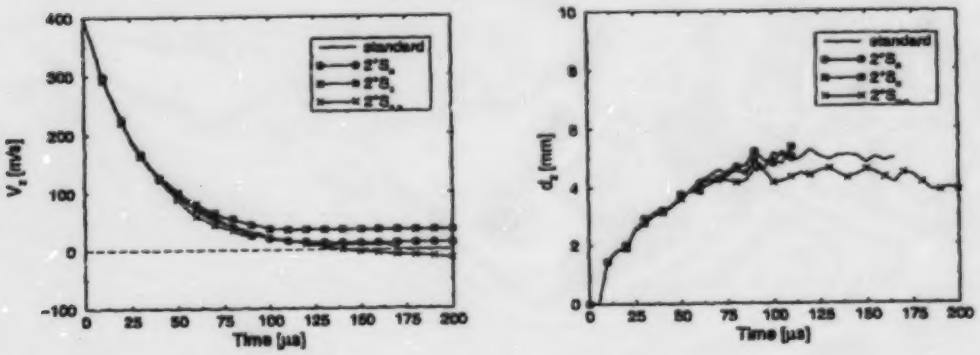

(a) Effects on FSP velocity.

(b) Effects on backplane displacement.

Figure 2.23: Effects of the delamination strength for the instantaneous failure model.

The effects of the delamination strength on the predicted panel response when the post-failure model is used is shown in Figure 2.24. Contrary to the effects seen for the instantaneous failure model in Figure 2.23, either individual or combined increases in the delamination normal or shear strength improved the predicted ballistic resistance. The effects were the largest for the delamination shear strength.

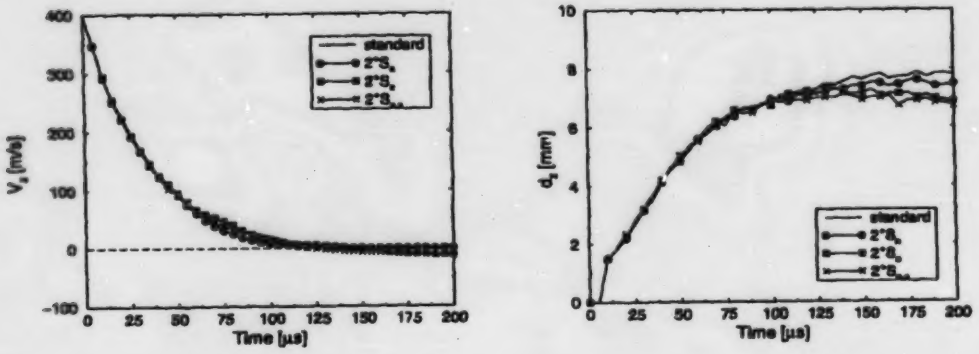

(a) Effects on FSP velocity.

(b) Effects on backplane displacement.

Figure 2.24: Effects of the delamination strength for the post-failure model.

Figure 2.25 shows the effects of the type of delamination release mechanism when the instantaneous failure model was used. Reducing the delamination release forces to zero in 100 time steps slightly decreased the predicted ballistic resistance. For the post-failure delamination release mechanism, the predicted ballistic resistance decreased with increasing values for the delamination release damage exponent m_{delam}.

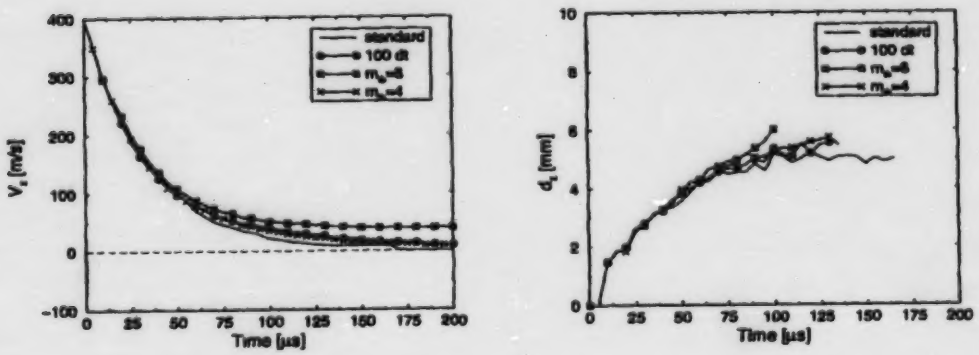

(a) Effects on FSP velocity.

(b) Effects on backplane displacement.

Figure 2.25: Effects of the discrete delamination release mechanism for the instantaneous failure model.

The effects of the delamination release mechanism on the model response in case the post-failure model was used is shown in Figure 2.26. Releasing the discrete delamination interface over 100 time steps resulted in a higher backplane displacement than found for the standard delamination release mechanism. The use of the post-failure delamination release mechanism led to smaller backplane displacements. The backplane displacement did not change for the values for the delamination release damage exponent m_{delam} used in this study.

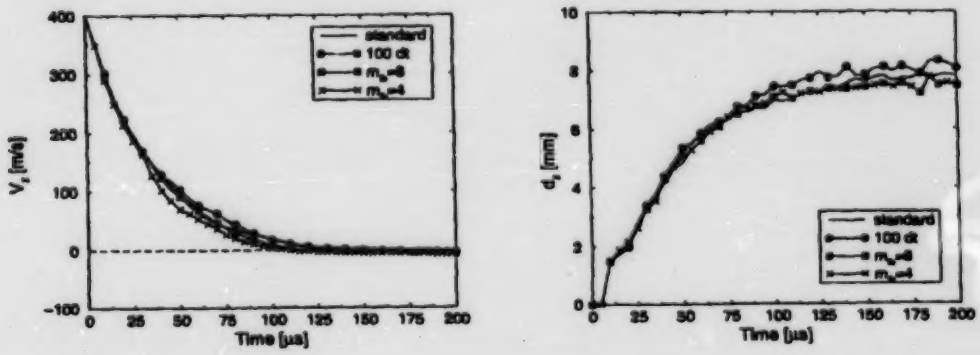

(a) Effects on FSP velocity.

(b) Effects on backplane displacement.

Figure 2.26: Effects of the discrete delamination release mechanism for the post-failure model.

2.6.4 Effect of Hourglass Control

All meshes used in the current study consisted entirely out of 8-node brick elements with single-point (reduced) Gaussian quadrature integration. Gaussian integration is used in finite element codes to perform volume integrations required in the solution process. The integration of some function g over the volume using Gaussian integration looks as follows:

$$\int_V g dV = \int_{-1}^{1}\int_{-1}^{1}\int_{-1}^{1} g\,|J|\,d\xi d\eta d\zeta = \sum_{j=1}^{n}\sum_{k=1}^{n}\sum_{l=1}^{n} g_{jkl}\,|J_{jkl}|\,w_j w_k w_l \qquad (2.24)$$

where $|J|$ is the determinant of the Jacobian matrix J; ξ, η, and ζ are the parametric coordinates of the nodal points varying between ± 1 (see Figure 2.27); n is the number of integration points; $g_{jkl} = g(\xi_j, \eta_k, \zeta_l)$; and w_j, w_k, and w_l are weighting factors.

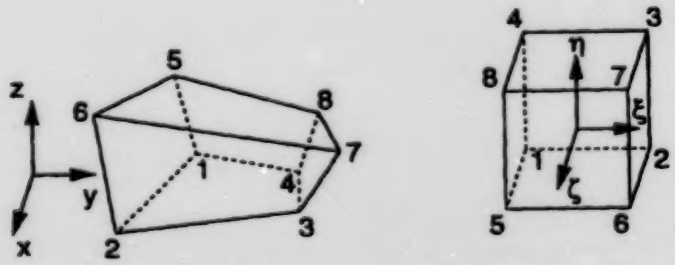

Figure 2.27: Element definition.

The Jacobian matrix J is given by:

$$J = \begin{bmatrix} \frac{\partial x}{\partial \xi} & \frac{\partial y}{\partial \xi} & \frac{\partial z}{\partial \xi} \\ \frac{\partial x}{\partial \eta} & \frac{\partial y}{\partial \eta} & \frac{\partial z}{\partial \eta} \\ \frac{\partial x}{\partial \zeta} & \frac{\partial y}{\partial \zeta} & \frac{\partial z}{\partial \zeta} \end{bmatrix} \qquad (2.25)$$

For single-point quadrature the following holds:

$$\begin{aligned} n &= 1 \\ w_j = w_k &= w_l = 2 \\ \xi_1 = \eta_1 &= \zeta_1 = 0 \end{aligned} \tag{2.26}$$

Which leads to:

$$\int_V g dV = 8g(0,0,0)\,|J(0,0,0)| \tag{2.27}$$

where $8\,|J(0,0,0)|$ approximates the element volume.

The biggest advantage of single-point integrated elements over fully integrated ($n = 8$) elements is a substantial saving in computational time. The costs for single-point integration are reduced by a factor of 16 for the strain and element nodal force computations and a factor of 8 for the stresses, compared to fully integrated elements (Hallquist, 1993).

The biggested disadvantage of the use of single-point integrated elements is their susceptibility to spurious zero-energy deformation modes, commonly referred to as hourglass modes. The deformations in the element resulting from the hourglass modes cause no stresses or internal forces to resist this deformation mode. Therefore, the hourglass modes can grow unboundedly (hence zero-energy modes) if they are not artificially controlled.

Hourglass modes can be resisted in LS-DYNA3D by either viscous or stiffness hourglass control forms (LS-DYNA3D, 1997). The hourglass controls are designed to resist the formation of the anomalous deformation modes resulting from hourglassing, but to have a negligible effect on the structural deformation modes. The viscous hourglass control forms resist the hourglass components of the nodal velocity with a viscous damping. The stiffness hourglass modes control hourglassing modes by adding a small elastic stiffness.

According to the LS-DYNA3D manual (LS-DYNA3D, 1997), the stiffness hourglass control form is often superior in reliability, but can stiffen the response of the model considerably, especially in case of large deformations. Galbraith (1998) stated that the viscous hourglass control forms are good for high velocity models, because the hourglass resistance is proportional to the hourglassing velocities; whereas the stiffness hourglass control forms are better for lower velocity models. Further, according to Galbraith (1998), the viscous forms will stop the hourglass oscillation, but will not correct the hourglassed shape; whereas the stiffness forms will bring the element to an 'un-hourglassed' shape, but will also affect the displacements.

Because the hourglass modes are orthogonal to the structural deformation, work done by the hourglass resistance is neglected in the energy equation. Consequently, the total and internal energies in the model are underestimated in case a substantial amount of energy is artificially added to the system to suppress hourglassing. Galbraith (1998) suggested that as a general rule the energy absorbed by the hourglass resisting forces should be less than 10 % of the internal energy. Unfortunately, the version of the LS-DYNA3D code used in the current research did not provide the option to output the hourglass energies.

The various hourglass control forms available in LS-DYNA3D were applied in the panel model together with the material properties given in Tables 2.4 and 2.5. Only the stiffness hourglass control form led to a stable solution. When the viscous hourglass control forms were used, the simulation was terminated due to excessive element deformation resulting in negative volume. Since the stiffness hourglass control form is known to stiffen the model response, the effects of this type of hourglass control on the projectile and backplane response were checked. The difference in response when either the entire panel model had stiffness hourglass control or when only the crater area was controlled with the stiffness hourglass control form and the

rest of the panel had the default viscous hourglass control was determined for both the instantaneous and post-failure model.

Figure 2.28(a) shows the effects of the stiffness hourglass control form on the projectile velocity. Using the stiffness hourglass control form only in the crater area resulted in an increased ballistic resistance for both the instantaneous and post-failure model. The higher ballistic resistance was represented by the lower projectile velocity and smaller backplane displacement. In case of the instantaneous failure model, complete backplane perforation was prevented when the stiffness hourglass control was used only in the crater area.

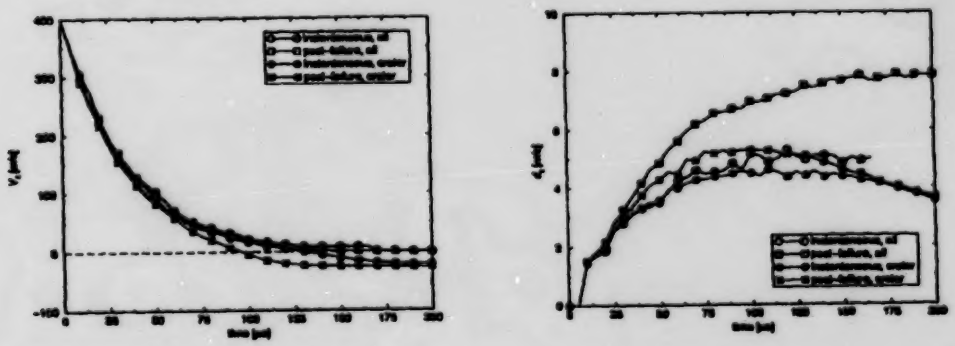

(a) Effects on FSP velocity. (b) Effects on backplane displacement.

Figure 2.28: Comparison between the instantaneous and post-failure model of the effects of the stiffness hourglassing control.

2.6.5 Mesh Sensitivity

Damage predictions using finite element techniques are known to be heavily dependent on the adopted mesh definition (Pijaudier-Cabot and Bažant, 1987; Pijaudier-Cabot and Bodé, 1995; Needleman and Tvergaard, 1994; Jirasek and Bažant, 1994; Tvergaard and Needleman, 1995; Anderson and Bodner, 1998; Kamel *et al.*, 1998). The damage and failure response of an element largely depends on the element dimension. In general, the smallest element in the mesh fails first and failure is a function of element size. This section presents the effects of the panel mesh definition on the simulated response obtained with the instantaneous and post-failure models. A distinction is made between changes in the element sizes in the in-plane and through-thickness direction of the panel.

Table 2.7 summarises the effects of the panel mesh definition on the simulation characteristics. The table shows that the in-plane element dimensions determine the stable time step size computed by the software. Doubling the number of elements per layer (through-thickness) did not result in a change in this minimum time step. However, doubling the in-plane element density resulted in halving the time step size. The table further shows that an increase in the number of elements and a decrease in the time step size led to an increase in the total CPU time of the simulation. The post-failure model was found to be more expensive computationally than the instantaneous model. Doubling both the number of in-plane and through-thickness elements resulted in an about fifteen-fold increase in CPU time compared to the initial mesh.

Table 2.7: Effects of mesh definition on simulation

Mesh	Nodes	Elements	Time Step [μs]	CPU - Instan [s]	CPU - Post [s]
initial	18658	8436	28.88	3180	2558
double t-t	27982	16872	28.88	7084	10320
triple t-t	37316	25308	28.88	11530	12120
double i-p	71022	33744	13.94	27000	50210
double i-p & tt	106533	67488	13.94	49200	52950

Nodes : number of nodes in panel mesh

Elements : number of elements in panel mesh

CPU - Instan : total CPU time of simulation with instantaneous failure model

CPU - Post : total CPU time of simulation with post-failure model

t-t : number of through-thickness elements

i-p : number of in-plane elements

The effects of the through-thickness mesh definition on the response of the model when the instantaneous failure model was used is given in Figure 2.29. The response of the model to increases in the number of elements per ply was not consistent. Doubling the amount of through-thickness elements resulted in a smaller decrease in the predicted projectile velocity and an earlier perforation of the backplane. However, tripling the through-thickness elements density improved the predicted ballistic resistance and the projectile was prevented from completely perforating the panel mesh. The results shown in Figure 2.29 indicate that the response of a model using the instantaneous failure model was highly sensitive to the through-thickness mesh definition. The response of the panel mesh is seen to not converge with the mesh refinement.

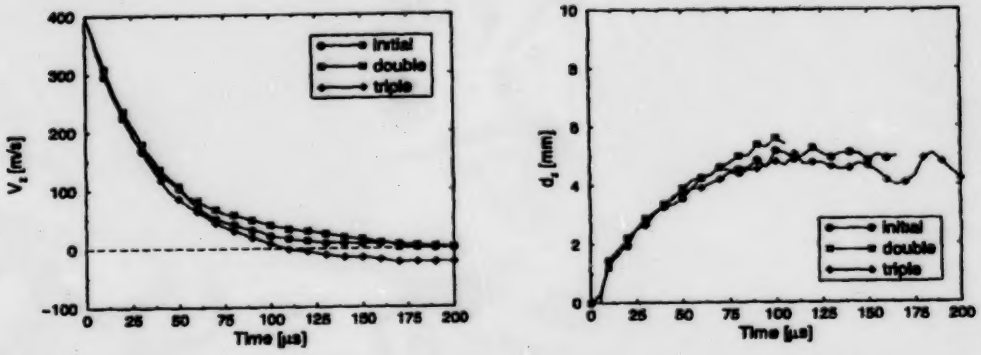

(a) Effects on FSP velocity.

(b) Effects on backplane displacement.

Figure 2.29: Effects of the through-thickness mesh definition for the instantaneous failure model.

Figure 2.30 shows the effect of the through-thickness mesh density on the predicted model response when the post-failure model was used. Increasing the number of through-thickness elements led to a corresponding increase in the predicted ballistic resistance. The rate of change in displacement with refinement decreased with increasing through-thickness mesh density, indicating that the panel mesh response had a tendency to converge with increased mesh refinement. Comparing Figure 2.29 with Figure 2.30 indicates that the use of the post-failure model resulted in a lower sensitivity of the model response to the through-thickness mesh definition than when the instantaneous failure model was used. This is consistent with findings by Majeed (1995), who studied the response of graphite laminated composites to drop weight impacts.

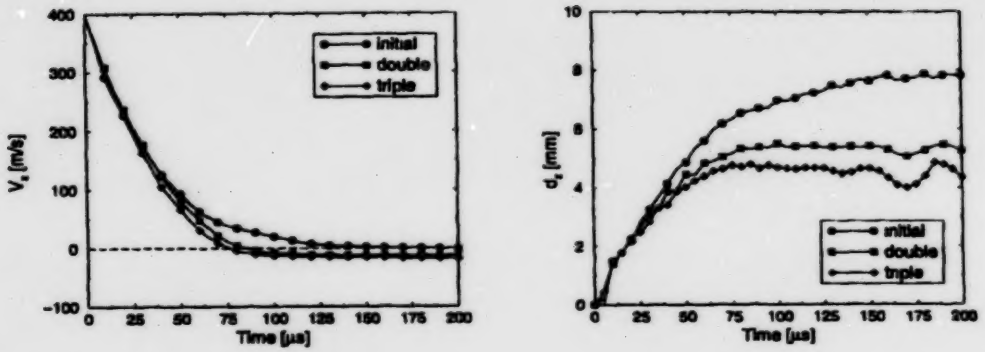

(a) Effects on FSP velocity.

(b) Effects on backplane displacement.

Figure 2.30: Effects of the through-thickness mesh definition for the post-failure model.

Figure 2.31 shows the effect that the in-plane mesh definition had on the predicted model response for the instantaneous failure model. Doubling the number of in-plane elements was found to result in a lower predicted ballistic resistance of the panel model, as can be observed from the higher projectile exit velocity in Figure 2.31(a) and an earlier complete perforation of the panel in Figure 2.31(b). Tripling the amount of in-plane elements resulted in 78,484 elements and 160,259 nodes, which exceeded the capacity of the software. Figure 2.31 also shows the effects of doubling both the amount of in-plane and through-thickness elements. In this case, the projectile was prevented from completely perforating the panel mesh. The results shown in Figure 2.31 confirm the trends seen in Figure 2.29 that the use of the instantaneous failure model resulted in a panel mesh that is very sensitive to the applied mesh definition.

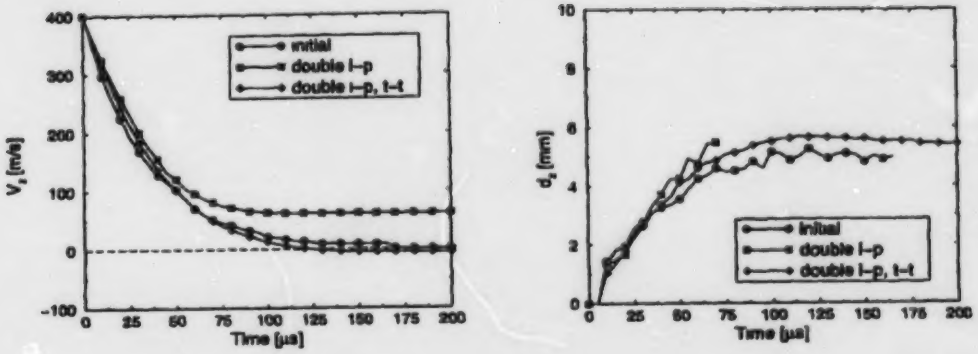

(a) Effects on FSP velocity.

(b) Effects on backplane displacement.

Figure 2.31: Effects of the in-plane mesh definition for the instantaneous failure model.

The effects of the in-plane mesh definition on the predicted panel response when the post-failure model was used is shown in Figure 2.32. The figure shows that the predicted ballistic resistance increased when the in-plane mesh definition was refined. The FSP decelerated at a higher rate and a substantially smaller backplane displacement was found when the in-plane mesh density was increased. As noted earlier, tripling the number of in-plane elements resulted in a mesh that exceeded the software capacity. When both the in-plane and through-thickness element density were doubled, the panel response resembled that obtained when only the number of in-plane elements were doubled. This confirms the observation made from Figure 2.30 that the use of the post-failure model resulted in a less mesh-sensitive panel response than with the instantaneous failure model, and that the response of the panel mesh with the post-failure model seemed to converge with increased mesh refinement.

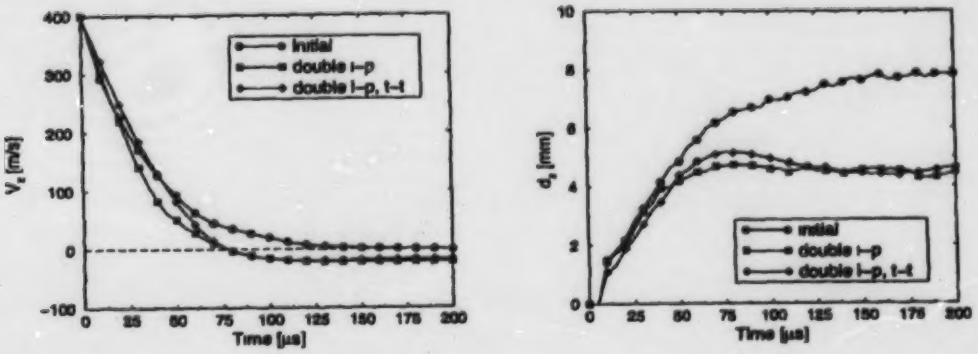

(a) Effects on FSP velocity.

(b) Effects on backplane displacement.

Figure 2.32: Effects of the in-plane mesh definition for the post-failure model.

2.7 Summary of Findings

It was found in this chapter that the post-failure model provides a more accurate prediction of the ballistic impact response of a Kevlar panel to a 1.1 g FSP than the instantaneous failure model. The through-thickness shear properties and the mesh definition were found to be the model characteristics exerting the largest influence on the model response. These findings will be used in Chapter 4, where the experiments presented in Chapter 3 are simulated.

Chapter 3

Ballistic Impact Testing

A series of ballistic impact tests were performed to evaluate the accuracy of the numerical model. The impact conditions were varied by using four different types of projectiles with a range of impact velocities. The tests were performed at the impact facility of the Composites Group at the University of British Columbia, Vancouver, BC, Canada (UBC series) and at the TNO Prins Maurits Laboratory, Rijswijk, The Netherlands (TNO Series). The details of the test setup, the measurement techniques, and the results obtained are presented in the following.

3.1 Experimental Set-up

The impact tests were performed on woven fabric Kevlar-29/phenolic laminated panels with planar dimensions of 101.6 x 152.4 mm (4x6 inches) and a thickness of 9.5 mm. The fabric was manufactured to conform to military specification MIL-C-44050 type II, class I, which specifies 14 ounces per square yard (oz/sq yd) untreated fabric using 1500 denier filaments having a 20.0 grammes per denier tenacity. The weaving style was a 2 by 2 basket weave using Kevlar-29 fibre. The panels consisted of 19 layers of fabric and were fabricated in accordance with military specification

MIL-H-44099A. The resin consisted of 50 percent phenol formaldehyde and 50 percent polyvinyl butyral resins (PVB). The resin content was between 15 to 18 % by weight. The resin density was approximately 1.2 g/cm^3 and the Kevlar density was about 1.45 g/cm^3. Using the rule of mixtures, this results in a density of the laminate of approximately 1.4 g/cm^3 (at 82 % fibre volume fraction).

During the ballistic tests in the UBC Series, the test specimens were supported by the fixture shown in Figure 3.1. The support fixture was made from aluminium and contained a 127 mm by 76.2 mm rectangular opening to enable measurements of the backplane deformation. The Kevlar panels were clamped to the support fixtures at all four corners. In order to have an unobstructed line of sight for the IMAX camera (see Section 3.2.2) in the TNO Series, a port-hole was created by extending the rectangular opening in the support fixture over the full length of the opening (i.e. 127 mm). This way, the panels were completely supported on their short side (101.6 mm) and completely free along their long side (127.0 mm).

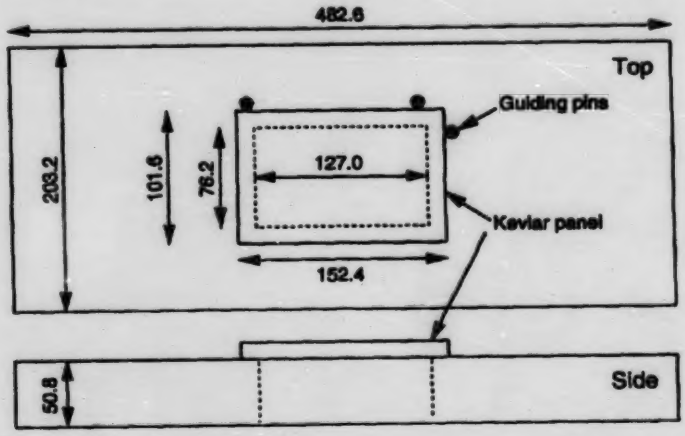

Figure 3.1: Target support fixture (dimensions in mm).

The panels tested in the UBC series were impacted by the cylindro-conical projectiles shown in Figure 2.7. The 0.22 and 0.30 calibre FSPs shown in Figure 2.3 and Figure 2.5 were used in the TNO Series. In both test series, the projectiles were propelled using a powder gun. A range of impact velocities was obtained by varying the amount of gun powder used to propel the projectile.

3.2 Measurement Techniques

Different measurement techniques were used in each test series to obtain information from the ballistic impact event. In the UBC Series, the ELVS system was used to obtain the projectile response history during the impact. In the TNO Series, IMAX and VISAR techniques were used to measure the response of both the projectile and the backplane. These measurement techniques will be discussed in more detail in the following sections.

3.2.1 ELVS Measuring System

The Enhanced Laser Velocity Sensor (ELVS), shown schematically in Figure 3.2, uses a sheet of laser light to continuously track the displacement of the projectile (Abdel-Rahman *et al.*, 1998; Starratt *et al.*, 1998; Cepuš *et al.*, 1999). The laser sheet is 25.4 mm (1 inch) wide and is aligned perpendicular to the flight path of the projectile. As the projectile passes through the laser sheet, the changing laser light intensity is recorded and correlated to the projectile displacement. Successive differentiation of the displacement-time history yields the projectile velocity- and acceleration-time histories, respectively. From this kinematic data, the projectile's energy- and impact force-time histories can easily be obtained.

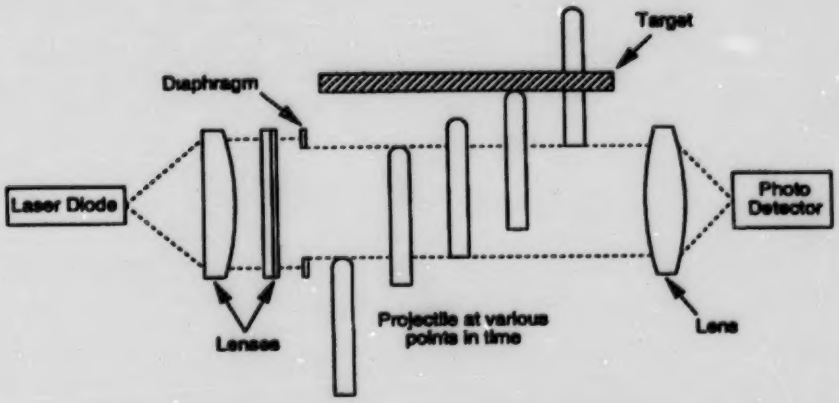

Figure 3.2: ELVS schematic (Cepuš *et al.*, 1999).

The ELVS system is capable of measuring velocities up to about 1000 m/s and the resolution in the projectile displacement measurements is 0.5 mm (Starratt *et al.*, 1998). The ELVS requires the use of sufficiently long projectiles to measure the projectile response during the entire impact event. The cylindro-conical projectiles shown in Figure 2.7 were specifically designed for this measuring system. However, due to their length, these projectiles become unstable in-flight at low velocities. Further, in cases where the target significantly deforms during the impact, the tail of the projectile exits the laser sheet before the impact event is over. Consequently, information on the final part of the impact event is lost. Another limitation of the ELVS system is that the data reduction scheme assumes the use of a non-deforming projectile. Obviously, the distinction between projectile displacement and deformation cannot be determined from the laser sheet measurements.

3.2.2 IMAX System

IMAX stands for IMAcon X-ray system, which is able to make high-speed framing pictures with X-rays (van der Heiden and van Bree, 1995). The system consists of an IMACON cine radiographic high-speed framing camera, an image converter tube (Thompson tube), and an X-ray gun. The X-ray gun is a conventional X-ray system with a hot cathode and can operate at a range of 70-150 kV. The X-ray gun can produce either single- or multiple-pulsed X-ray beams. The image converter tube converts the X-rays into visible light. The IMACON camera is an electro-optical camera, which converts the light from the image converter tube into electrons which are shifted (horizontally and vertically) and focussed onto a phosphor screen. A negative or polaroid film is placed against the phosphor screen to capture the frames. The IMACON camera is capable of taking 6-24 pictures at a recording speed of 10,000 to 1 million frames per second. With the IMAX system, eight pictures can be taken.

Since the IMAX system is based on X-ray technology, both the position of the projectile inside the target and the deformation response of the target can be measured during the impact event. Limitations of the IMAX system include the number of images (8) that can be taken and the limited resolution of these images.

3.2.3 VISAR System

The Velocity Interferometer System for Any Reflector (VISAR) is a laser Doppler measuring system which detects velocity changes in time of any surface that gives sufficient reflection (van der Heiden and van Bree, 1995). The system uses a high power Argon Ion laser with a nominal power of 1 Watt (single frequency). The laser spot is focussed onto the target by a lens. The target must reflect the light in all

directions. The reflected light will have a Doppler shift if the surface is moving. The shifted light is directed into the VISAR, which is an interferometer based on the principle of Michelson. The VISAR determines the phase shift of the light by dividing the light into two beams with a different path length. Interference occurs when these beams are combined. Both fast velocity changes (500 m/s in 50 ns maximum) and slow velocity changes (10 m/s in 1 ms maximum) can be measured with the VISAR system by adjusting the path length of the delay beam in the interferometer. The velocity history is determined from this interference signal by a signal analysis software specifically designed for the VISAR system.

3.3 TNO Series

The results obtained from the TNO Series are presented in this section. The test matrix used during this series is summarised in Table 3.1. The table indicates the type of FSP used, the measured impact velocity, and the figure presenting the displacement- and velocity-time histories. The impact velocities of the projectiles used in the TNO series were measured with two light-screens placed 127 mm apart in front of the target. The stand-off between the target and the nearest light-screen was 100 mm. All shots from the TNO Series presented in the following were non-perforating. The moment of impact was measured by a trigger foil glued to the front of the panel. Perforation of this foil by the FSP triggered the IMAX and VISAR measurements. Therefore, t=0 μs in the following graphs is equal to the time of impact.

Table 3.1: Summary of TNO Series

FSP Type	Impact Velocity	Results in
1.1 g	586 m/s	Fig. 3.4(a)
1.1 g	560 m/s	Fig. 3.4(b)
1.1 g	545 m/s	Fig. 3.4(c)
1.1 g	483 m/s	Fig. 3.4(d)
2.8 g	511 m/s	Fig. 3.8(a)
2.8 g	461 m/s	Fig. 3.8(b)
2.8 g	446 m/s	Fig. 3.8(c)
2.8 g	398 m/s	Fig. 3.8(d)
2.8 g	386 m/s	Fig. 3.8(e)
2.8 g	321 m/s	Fig. 3.8(f)

The velocity-time histories for the backplane were obtained from the VISAR measurements. The fast velocity changes of the backplane at the beginning of the impact event could not be determined from the VISAR signal, since the VISAR settings were adjusted to obtain information on the maximum backplane displacement which occurs at low velocity changes over longer times. A curve was fit through the velocity data points obtained from the VISAR. The fit data was time-integrated to obtain the backplane time-history. The position of the projectile and the backplane were obtained from the IMAX pictures by using either a magnifying glass (10 X) or a densitometric scanner.

Due to the limited resolution of the IMAX images, the exact position of the FSP inside the panel was hard to determine, especially for the small 1.1 g FSP. Consequently, the IMAX data provided useful data on the FSP displacement in only a few cases. Therefore, only the backplane displacements obtained from the IMAX data will be presented here. Since the IMAX system provides only eight images, a maximum of eight discrete data points could be obtained.

The VISAR system provided a continuous measurement of the backplane velocity with a higher resolution than could be obtained with the IMAX. However, the VISAR measurements did not always give the maximum backplane displacement, since the VISAR laser beam was not always directed at the location with maximum backplane deformation. In these cases, the IMAX data provided a better representation of the backplane deformation. Therefore, both the IMAX and VISAR data should be considered to obtain a complete picture of the backplane response.

3.3.1 1.1 g FSP

Figure 3.3 shows an IMAX image captured during the impact of a Kevlar panel by a 1.1 g FSP at 586 m/s. The figure clearly shows the limited resolution of the IMAX image and the difficulty in distinguishing the FSP from the panel. However, the image does provide a good picture of the extent of the backplane displacement at various instances during the impact event. The IMAX images captured during the other impacts with 1.1 g FSPs will not be presented in this section, but can be found in Appendix A.1.

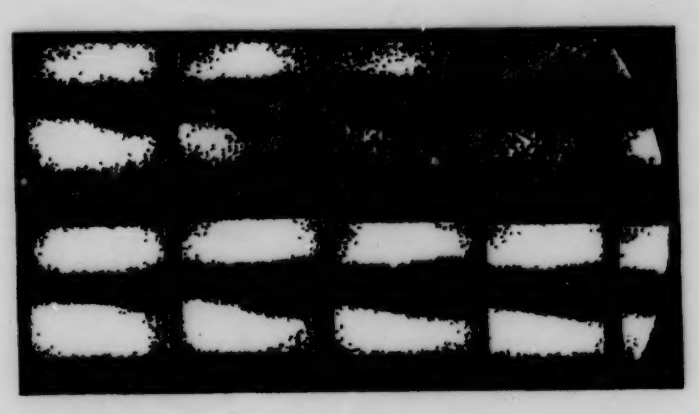

Figure 3.3: IMAX image of a Kevlar panel impacted by a 1.1 g FSP at 586 m/s.

The measured backplane responses for the Kevlar panels impacted by 1.1 g FSPs are given in Figure 3.4. The figure shows the data obtained with the VISAR system, together with the curve fit through the VISAR data points. The fit curve was integrated to obtain the backplane displacement-time history (VISAR, fit). Figure 3.4 also shows the discrete backplane displacement data obtained from the IMAX images.

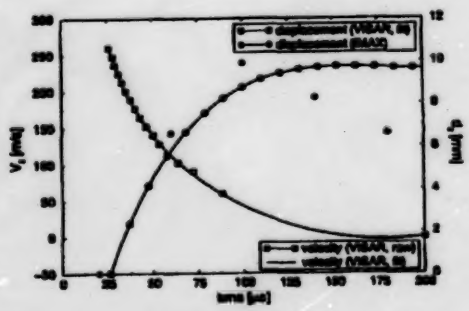

(a) V_i=586 m/s.

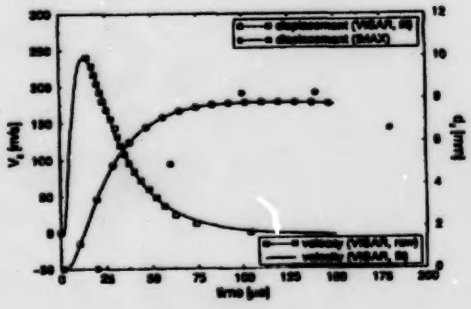

(b) V_i=560 m/s.

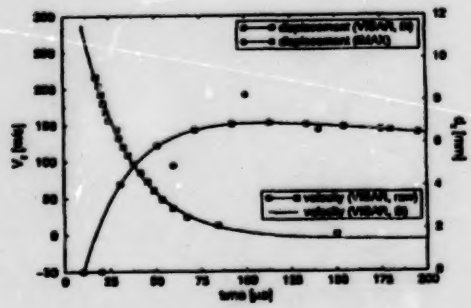

(c) V_i=545 m/s.

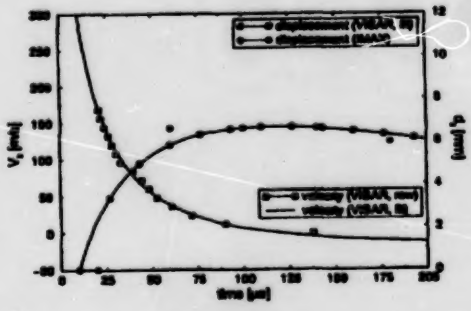

(d) V_i=483 m/s.

Figure 3.4: Measured backplane response of Kevlar panels impacted by 1.1 g FSPs.

In general, the maximum backplane displacement obtained from the IMAX and VISAR data agreed well. The measurements are compared in Figure 3.5, which shows the maximum backplane displacement versus the FSP impact velocity. Both the IMAX and VISAR data show that the maximum backplane displacement decreases with decreasing impact velocity.

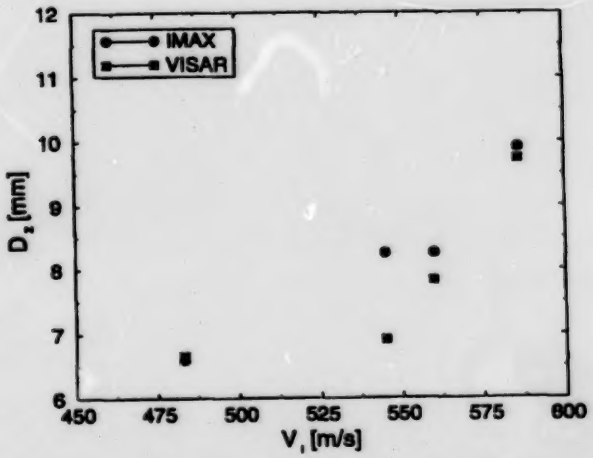

Figure 3.5: Maximum backplane displacement versus impact velocities for Kevlar panels impacted by 1.1 g FSPs.

However, the displacement-time history deduced from the VISAR measurement did not always follow the trend observed in the IMAX data points. A number of explanations can be found for this. First, the low resolution of the IMAX images made it hard to determined the onset of backplane motion. Second, the raw VISAR data in Figure 3.4 indicates that the majority of the VISAR data points were obtained prior to the occurrence of the maximum backplane displacement. Consequently, the VISAR data could not give an accurate representation of the backplane displacement around its maximum.

Figure 3.6 displays the front and back face of a Kevlar panel after it was impacted by a 1.1 g FSP at 586 m/s. The FSP had impacted the panel slightly to the right of its centre. The backplane showed a small amount of residual deformation. The centre of the residual deformation was slightly to the right of centre, which was in accordance with the point of impact.

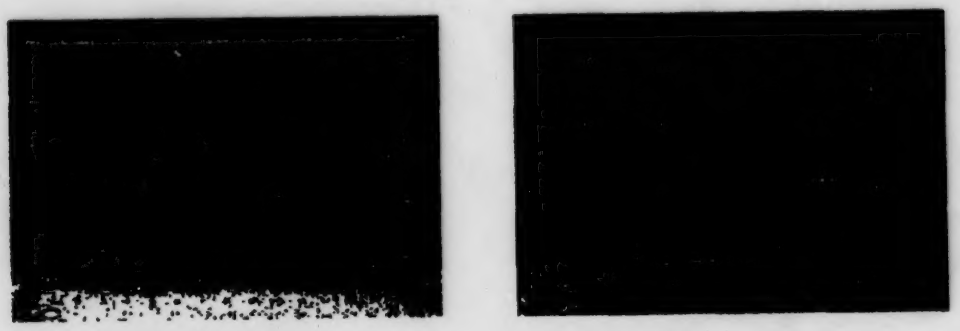

(a) Front. (b) Back.

Figure 3.6: Pictures of Kevlar panel after being impacted by a 1.1 g FSP at 586 m/s.

Visual examination of the panels impacted by the 1.1 g FSPs revealed that the panels impacted at 586, 560, and 545 m/s showed signs of delaminations on the right edge of the panel. No signs of delaminations were observed at the other edges. These delaminations separated the backplane from the remainder of the panel. The extent of the delamination decreased and the thickness of the backplane increased with decreasing impact velocity.

3.3.2 2.8 g FSP

Figure 3.7 presents an IMAX image captured when a 2.8 g FSP impacted a Kevlar panel at 511 m/s. The figure shows that the 2.8 g FSP was easier to distinguish from the panel than was the case for the smaller 1.1 g FSP in Figure 3.3. The image shows the backplane at various stages during the impact event. The IMAX images captured during the other impacts with 2.8 g FSPs will not be presented in this section, but are placed in Appendix A.2.

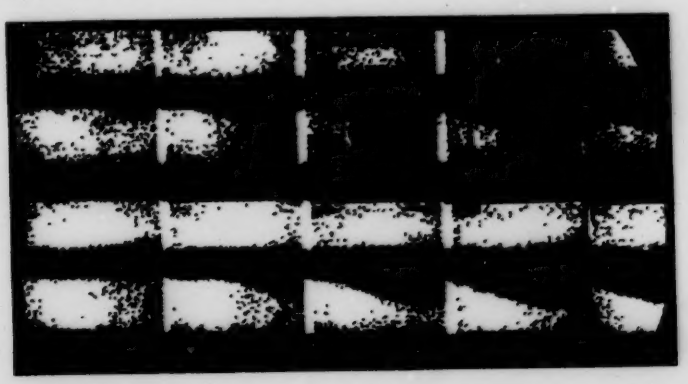

Figure 3.7: IMAX image of a Kevlar panel impacted by a 2.8 g FSP at 511 m/s.

Figure 3.8 presents the measured backplane displacements obtained from the Kevlar panels impacted by 2.8 g FSPs. With the exception of Figure 3.8(a), the agreement between the IMAX and VISAR maximum backplane displacements is good. The backplane displacement-time history obtained from the VISAR measurements in Figure 3.8 seem to follow the IMAX data points more closely than was the case for the 1.1 g FSP. This is probably due to the larger number of VISAR data points around the point of maximum backplane displacement.

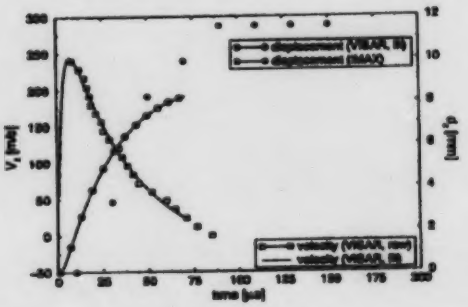

(a) V_i=511 m/s.

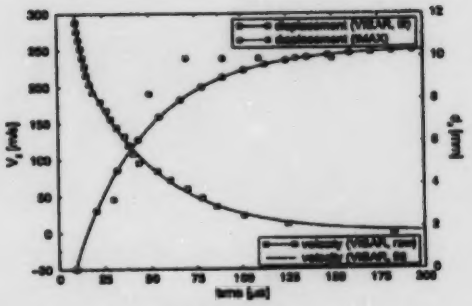

(b) V_i=461 m/s.

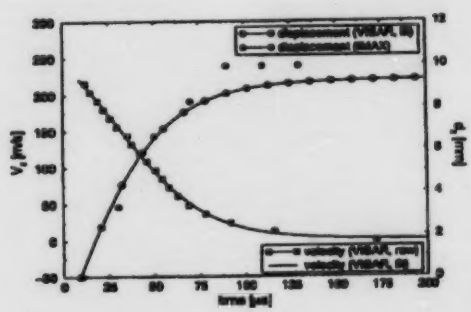

(c) V_i=446 m/s.

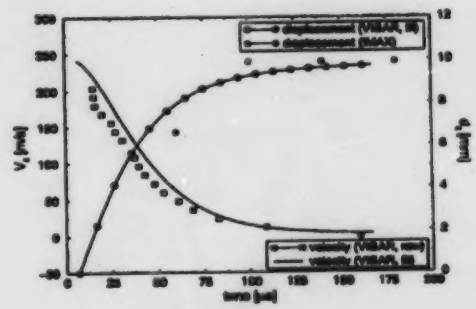

(d) V_i=398 m/s.

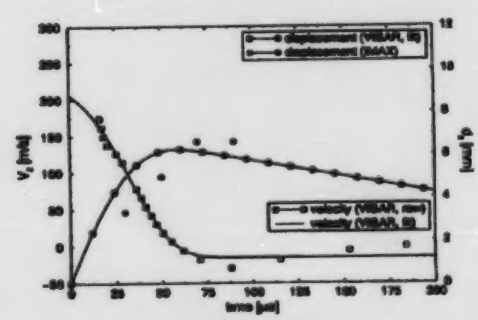

(e) V_i=386 m/s.

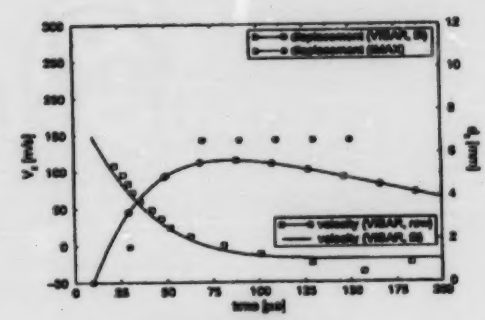

(f) V_i=321 m/s.

Figure 3.8: Measured backplane response of Kevlar panels impacted by 2.8 g FSPs.

The relation between the maximum backplane displacement and the impact velocity of the 2.8 g FSP is shown in Figure 3.9. The figure reiterates the relatively good agreement between the IMAX and VISAR data. In general, the maximum backplane displacement decreased with decreasing impact velocity.

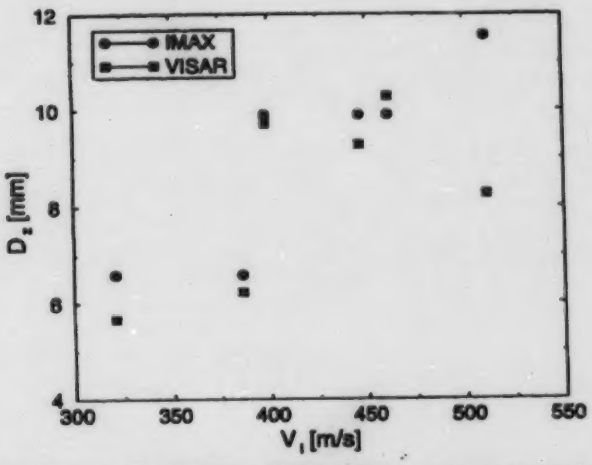

Figure 3.9: Maximum backplane displacement versus impact velocities for Kevlar panels impacted by 2.8 g FSPs.

The post-impact state of a panel impacted by a 2.8 g FSP at 511 m/s is shown in Figure 3.10. In general, the apparent damage and residual deformation was larger in the panels impacted by 2.8 g FSPs than seen for the 1.1 g FSPs. Figure 3.10 shows that the impacting projectile caused wrinkling at the panel's front face and substantial residual backplane deformation. The residual backplane deformation decreased with decreasing impact velocity.

Delaminations were found on both long edges of the panel and extended over almost the entire length of the edge for the panel shown in Figure 3.10. Only the panels impacted at 386 and 321 m/s showed no visible signs of delamination along

the edges. Figure 3.10 clearly shows that these delaminations separate the backplane from the remainder of the panel. The size of these delaminations decreased and the thickness of the backplane increased with decreasing impact velocity.

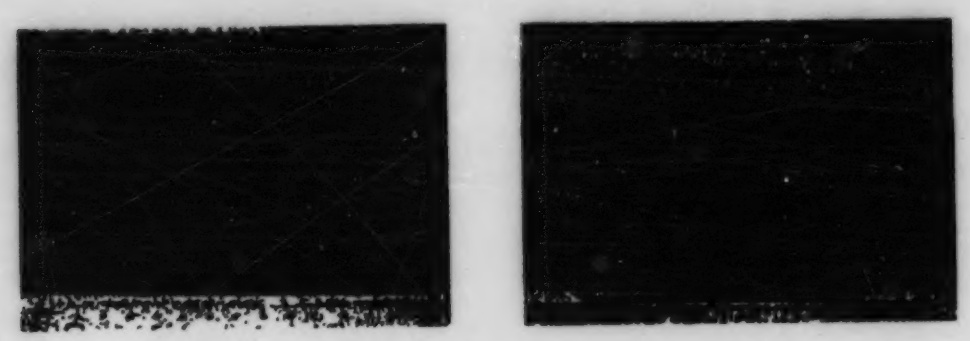

(a) Front. (b) Back.

Figure 3.10: Pictures of Kevlar panel after being impacted by a 2.8 g FSP at 511 m/s.

3.4 UBC Series

This section presents the measurements obtained from the panels impacted in the UBC Series. Table 3.2 summarises the tests from this series. The table indicates the type of cylindro-conical projectile used, the measured impact velocity, whether the panel was perforated completely, and the figure in this report containing the velocity- and displacement-time histories. The incident impact velocities for the panels tested in the UBC series were measured with a separate laser system. Since the ballistic limits of the projectile-panel combinations used in this series were not known, a number of shots were fired with both types of projectiles to obtain an impact velocity that did not result in complete perforation of the panel. Once this velocity was obtained, a number of tests were performed above and below this velocity to obtain a range of impact conditions. In the following, the tests are ordered in decreasing impact velocity.

Table 3.2: Summary of UBC Series

Projectile Type	Impact Velocity	Perforation	Results in
flat-nose	369 m/s	yes	Fig. 3.11(a)
flat-nose	287 m/s	yes	Fig. 3.11(b)
flat-nose	263 m/s	yes	Fig. 3.11(c)
flat-nose	251 m/s	no	Fig. 3.12(a)
flat-nose	238 m/s	no	Fig. 3.12(b)
flat-nose	230 m/s	no	Fig. 3.12(c)
flat-nose	211 m/s	no	Fig. 3.12(d)
flat-nose	178 m/s	no	Fig. 3.12(e)
sharp-nose	262 m/s	yes	Fig. 3.14(a)
sharp-nose	236 m/s	yes	Fig. 3.14(b)

3.4.1 Flat-Nose Cylindro-Conical Projectiles

Perforating Shots

Figure 3.11 presents the measured projectile response of flat-nose cylindro-conical projectiles impacting Kevlar panels. All impacts presented in this figure resulted in complete perforation of the panel. The projectile displacement was measured by the ELVS system. The projectile velocity was obtained by differentiating a curve fit through the measured displacement data. The moment of impact was not measured directly, but was determined by the ELVS data analysis software as the time at which the slope of the measured displacement-time history changed from a constant value, indicating a change in projectile velocity. The graphs in Figure 3.11 start at the numerically determined time of impact.

Based on a projectile length of 40 mm and the 20 mm gap between the ELVS laser beam and the panel, the back 20 mm of the projectile should be still inside the laser beam at the moment of impact. Therefore, only 20 mm of projectile displacement can be measured after the moment of impact, since the projectile was found not to deform noticeably during the impact. The final projectile displacements of 25 mm in Figure 3.11 indicates that the moment of impact was determined inaccurately by the ELVS data analysis system. The slight increases in the projectile velocity at the beginning of the test in Figure 3.11(b) and 3.11(c) confirm that the moment of impact is determined incorrectly.

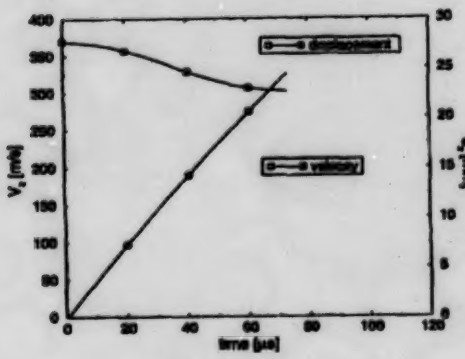

(a) V_i=369 m/s.

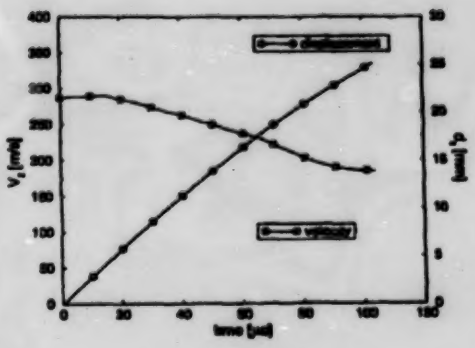

(b) V_i=287 m/s.

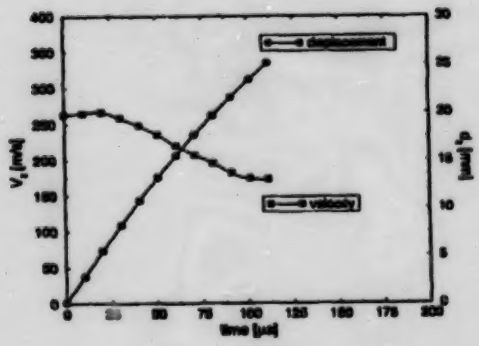

(c) V_i=263 m/s.

Figure 3.11: Measured response of flat-nose cylindro-conical projectiles impacting Kevlar panels: perforating shots.

Non-Perforating Shots

The measurements obtained from the non-perforating impacts of flat-nose cylindro-conical projectiles on Kevlar panels are shown in Figure 3.12. The figure exhibits the same problem with the numerically determined moment of impact as was found in Figure 3.11.

For the measurements presented in Figure 3.12(c), the settings of the ELVS were changed so that measurements could be taken over a longer period of time. Examination of the post-mortem panel showed that the projectile had punctured the backplane, but rebounded out of the panel afterwards due to the elastic springback of the backplane. The projectile displacement-time history in Figure 3.12(c) indicates the puncturing of the backplane by the sudden increase in the projectile displacement around 250 μs. The plateau in the displacement-time history between 300 - 400 μs shows that the backplane maintained its maximum deformation before it rebounded. The projectile displacement-time history also shows part of the backplane springback process, represented by the decreasing projectile displacement after about 400 μs.

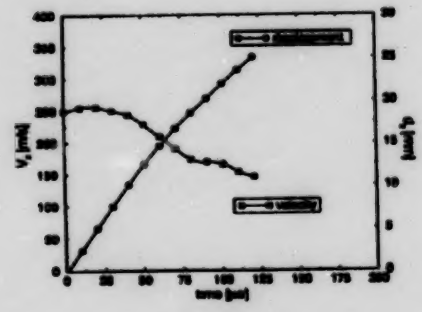

(a) V_i=251 m/s.

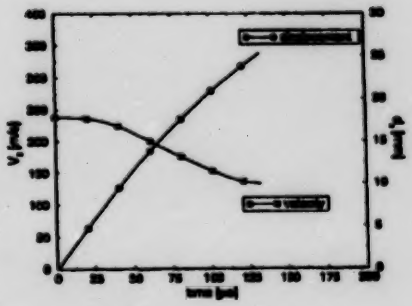

(b) V_i=238 m/s.

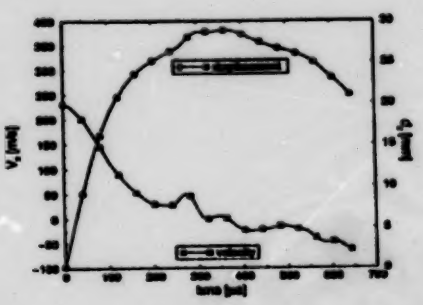

(c) V_i=230 m/s.

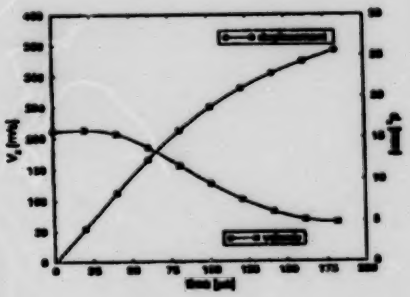

(d) V_i=211 m/s.

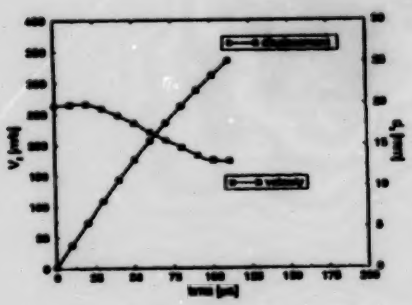

(e) V_i=178 m/s.

Figure 3.12: Measured response of flat-nose cylindro-conical projectiles impacting Kevlar panels: non-perforating shots.

Figure 3.13 shows a Kevlar panel impacted by a flat-nose cylindro-conical projectile at 251 m/s. The figure shows a substantial amount of residual backplane deformation and signs of delamination along the long edges. Examination of the impacted panel revealed that the projectile had punctured the backplane, but did not completely perforate the panel. The projectile rebounded back out of the panel after impact. The panel impacted at 251 m/s was the only panel showing signs of puncture damage on its backface.

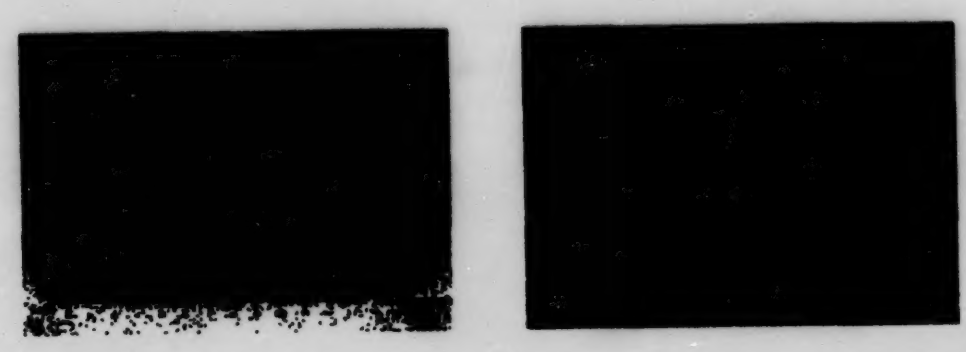

(a) Front. (b) Back.

Figure 3.13: Pictures of Kevlar panel after being impacted by a flat-nose cylindro-conical projectile at 251 m/s.

Visual comparison of the impacted panels showed that the residual backplane deformation decreased with decreasing impact velocity. Only the panels impacted at 251 and 238 m/s showed visible signs of delaminations extending to the long edges of the panel. The backplane deformation was found to have been restricted by the support conditions in all panels impacted by flat-nose cylindro-conical projectiles.

3.4.2 Sharp-Nose Cylindro-Conical Projectiles

Perforating Shots

Figure 3.14 presents the measured response for the sharp-nose cylindro-conical projectiles impacting Kevlar panels. Complete backplane perforation was prevented only for the 155 m/s case, but in this case the backplane was punctured by the projectile. The figures related to the complete perforation cases show that the measured data exhibited the same problem with the determination of the moment of impact observed previously. For the measurements presented in Figure 3.14(d), the settings of the ELVS were changed so that measurements could be taken over a longer period of time. This figure indicates that the projectile was stopped by the panel and rebounded afterwards.

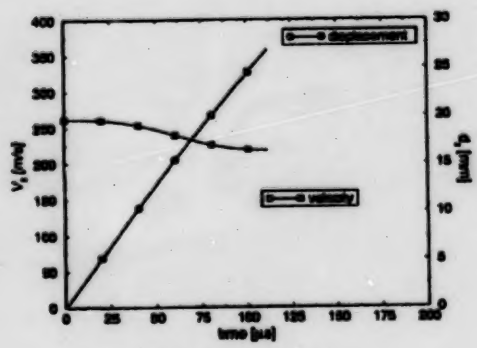

(a) V_i=262 m/s.

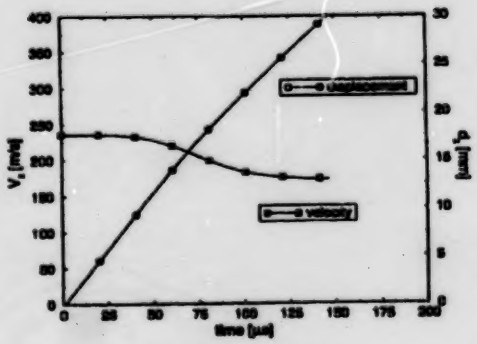

(b) V_i=236 m/s.

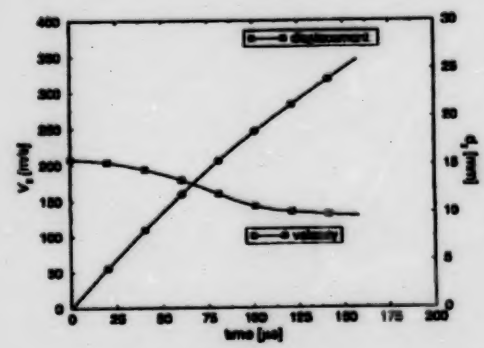

(c) V_i=207 m/s.

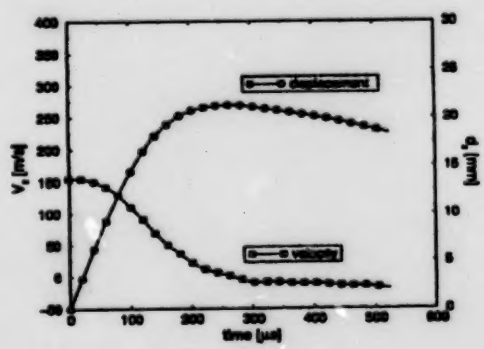

(d) V_i=155 m/s.

Figure 3.14: Measured response of sharp-nose cylindro-conical projectiles impacting Kevlar panels: perforating shots.

Figure 3.15 shows the Kevlar panel after it was impacted by a sharp-nose cylindro-conical projectile at 236 m/s. The figure shows that the residual backplane deformation was small and localised around the crater. No signs of delamination were found along any of the edges. Fibres were pushed out of the crater at the backface. There were no signs that the backplane deformation had been restricted by the support conditions, indicating that the dynamic backplane deformation had been smaller than for the flat-nose projectiles.

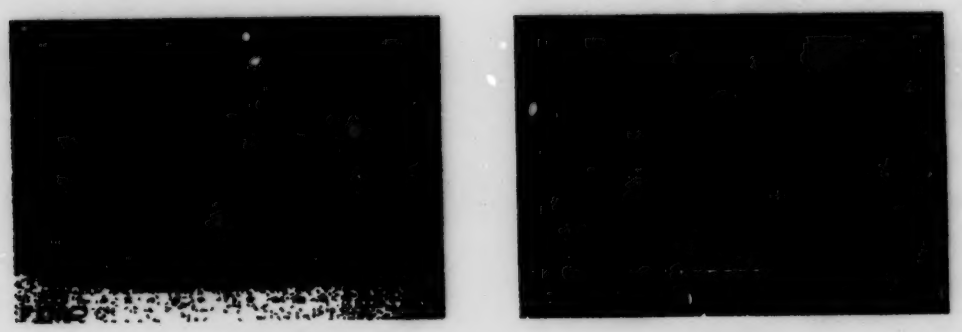

(a) Front. (b) Back.

Figure 3.15: Pictures of Kevlar panel after being impacted by a sharp-nose cylindro-conical projectile at 236 m/s.

Chapter 4

Simulation of Ballistic Impact Tests

The ballistic experiments on Kevlar panels presented in Chapter 3 were simulated using the numerical model presented in Chapter 2. In this chapter, the numerical and experimental results are compared to assess the capabilities and limitations of the numerical model.

4.1 Model Description

4.1.1 Mesh

Finite element meshes of the Kevlar panels were built, including the support conditions corresponding to the UBC and TNO test conditions. The support conditions differed somewhat between the UBC and TNO series. For the simulation of the tests performed at UBC, the panel was supported at the bottom over a distance of 12.7 mm (0.5 inches) from the periphery. In the simulations of the TNO tests, the bottom of the panel was supported only on the short sides, accounting for the IMAX port-hole created for these tests.

To reduce computational time, only one quarter of the problem was modelled, utilising symmetry boundary conditions on the interior edges. All components of the model were discretised using 8-node brick elements with single point integration. Figure 4.1 shows the panel mesh used for the simulations of the experiments. The panel model consisted of 19 plies, each 0.5 mm thick, resulting in a total panel thickness of 9.5 mm. Each ply in the panel model was 2 elements thick, resulting in 38 elements through the thickness of the panel. A discrete delamination interface was inserted between each adjacent ply pair to enable the simulation of delamination initiation and growth.

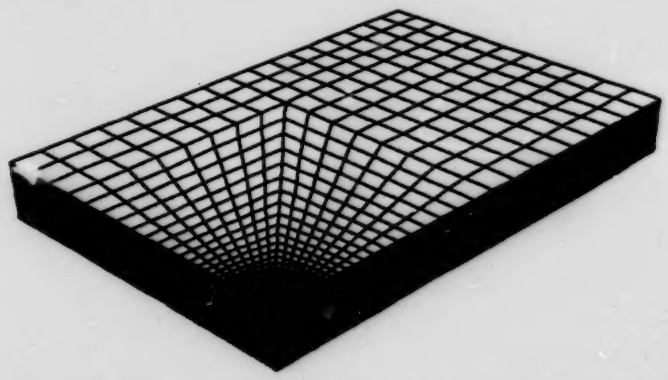

Figure 4.1: Finite element model of woven Kevlar-29 laminated panel used in simulations of UBC and TNO series.

Figure 4.2 shows a close-up of the impact area together with the meshes used for the FSPs in simulations of the TNO series. The meshes used for the conical projectiles in the simulations of the UBC series are shown in Figure 4.3. Care was taken to have similar element sizes in the projectiles and immediate impact area to avoid numerical contact problems. The impact velocities measured in the experiments were prescribed as initial velocities for the projectile nodes.

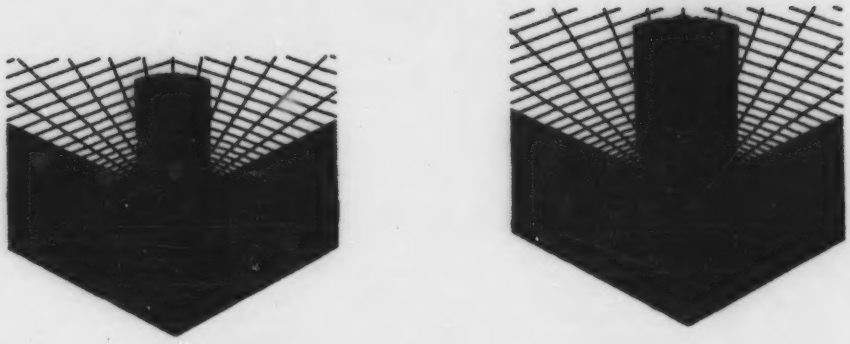

(a) 1.1 g FSP (b) 2.8 g FSP

Figure 4.2: Close-up of the impact area and FSPs used in simulations of the TNO series.

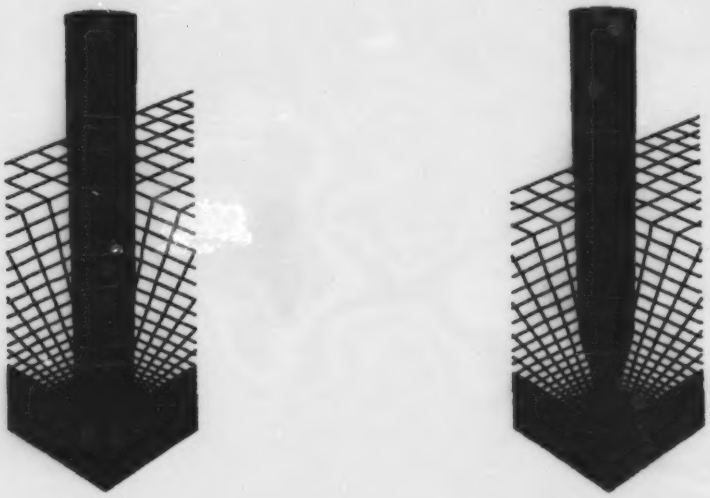

(a) flat-nose projectile (b) sharp-nose projectile

Figure 4.3: Close-up of the impact area and FSPs used in simulations of the UBC series.

4.1.2 Material Properties

Initial numerical simulations using the material properties given in Tables 2.4 and 2.5 and the measured impact velocities resulted in predictions of complete perforation of the panel mesh in all cases. However, in the experiments, complete perforation did not occur in the TNO series and only occurred in some tests in the UBC series. The quasi-static nature of the adopted material properties was considered to be the cause of this discrepancy between the experimental and numerical results.

Unfortunately, high-strain rate data on Kevlar composites are rare and difficult to obtain experimentally. The approach used in this report was to modify some of the material properties in the numerical model to account for the strain-rate effects. This approach was adopted to "calibrate" the model response, recognising that high strain-rate data was not available and that it was beyond the scope of the current study to generate this data.

The numerical material parameters were modified for one specific impact condition. The impact of a 1.1 g FSP on a Kevlar panel at 586 m/s was chosen for this purpose. Based on the results of the parametric study presented in Section 2.6, it was determined that by doubling the through-thickness shear strengths, S_{23} and S_{31}, and halving the through-thickness shear moduli, G_{23} and G_{31}, the numerical model was capable of giving reasonably accurate predictions of the measured data.

Further, the in-plane tensile strengths, S_{11} and S_{22}, were modified to obtain a failure strain $\epsilon_{f_{11,22}} = 0.03$, which is similar to the fibre breakage strain for Kevlar-29 presented in Table 2.1. The adopted values for the final material properties used in the simulations of the ballistic impact tests are summarised in Tables 4.1 and 4.2.

Table 4.1: Elastic properties adopted for woven Kevlar in numerical model

$E_{11,22}$ [GPa]	E_{33} [GPa]	ν_{21} [-]	$\nu_{31,32}$ [-]	G_{12} [GPa]	$G_{23,31}$ [GPa]	ρ [g/cm^3]
18.5	6.0	0.25	0.33	0.77	2.715	1.23

Table 4.2: Strength properties adopted for woven Kevlar in numerical model

$S_{11,22}$ [MPa]	S_{33} [MPa]	S_{12} [MPa]	$S_{23,31}$ [MPa]	S_n [MPa]	S_s [MPa]
555.0	1200.0	77.0	1086.0	34.5	9.0

In order to assess the predictive nature of the model, the properties given in Tables 4.1 and 4.2 were held fixed in simulations of the other ballistic impacts. In this manner, the modified material properties used in the 1.1 g model could be assessed for these rather different impactor masses and geometries.

4.2 Simulation of TNO Series

The following presents the results from simulations of the ballistic impact tests performed at TNO. The results from the simulations were compared with the measurements from the IMAX and VISAR systems, presented in Section 3.3. The impacts using 1.1 g and 2.8 g FSPs are presented separately in Sections 4.2.1 and 4.2.2, respectively.

4.2.1 1.1 g FSP

Figure 4.4 shows a sequence of deformed mesh plots obtained from the simulation of the ballistic experiment on the Kevlar panel at an impact velocity of 586 m/s. The plot at t=10 μs shows the initial stage of the penetration process, in which the projectile forms a crater in the panel by either through-thickness compressive or shear failure. Crater formation is modelled through deletion or "erosion" of elements meeting these failure criteria. The tip of the FSP model was found to deform slightly during the initial stage of the penetration process.

Delaminations are predicted both adjacent to and ahead of the advancing projectile. The delaminations ahead of the projectile were thought to be caused by stress waves preceding the FSP. The plot at t=75 μs shows the model at maximum backplane deformation, indicating extensive delamination and substantial backplane deformation. The plot at t=200 μs shows the mesh at the end of the simulation, after the projectile has been pushed back upwards by the elastic springback of the backplane.

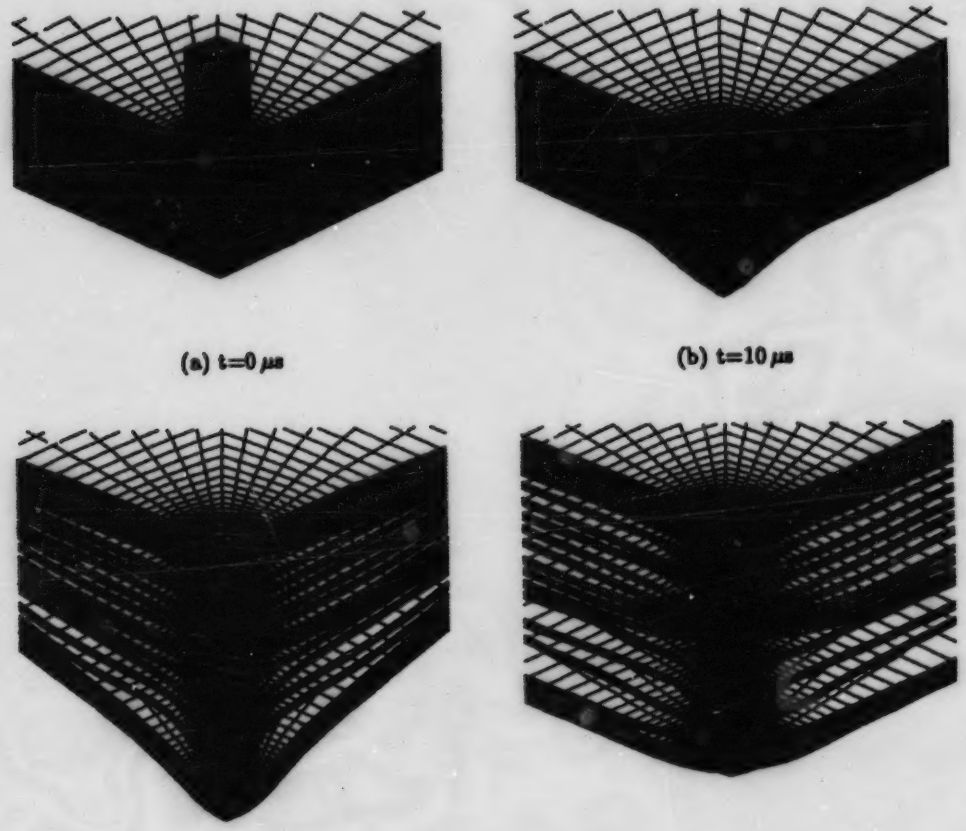

(a) t=0 μs (b) t=10 μs

(c) t=75 μs (d) t=200 μs

Figure 4.4: Sequence of deformed mesh plots of a 1.1 g FSP impacting a Kevlar panel at 586 m/s.

The measured and simulated backplane displacement time-histories for Kevlar panels impacted by 1.1 g FSPs are presented in Figure 4.5. The simulation data shown in Figure 4.5(a) result from the "calibration" of the numerical material properties. These properties were then held constant for the simulations with the other impact velocities to determine the predictive ability of the model using a constant material description.

The figure shows that the numerical model provided a reasonably accurate prediction of the maximum backplane displacement in most cases. The numerical data followed the trends obtained from the IMAX measurements, with sharp rises in displacement as the push out of the backplane initiates. The reason for the difference in time for the onset of backplane motion between the numerical and experimental data is unclear.

This difference could be attributed to a lack of strain-rate sensitivity in the numerical model, but possibly is also due to experimental error. It is often difficult to temporally resolve measurements on the backface of a target with the moment of initial impact. The graphs in Figure 4.5 show that this difference in time of initial backplane motion is quite variable. Furthermore, the initial slopes of the predicted and measured displacement versus time histories agree well, suggesting that the model does predict the deceleration of the FSP accurately and that this difference is likely an experimental issue.

The predicted pull-back of the backplane in Figure 4.5(d) was higher than observed in the experiments. This difference perhaps indicates an inadequate loss of strength and stiffness in the predicted post-failure response.

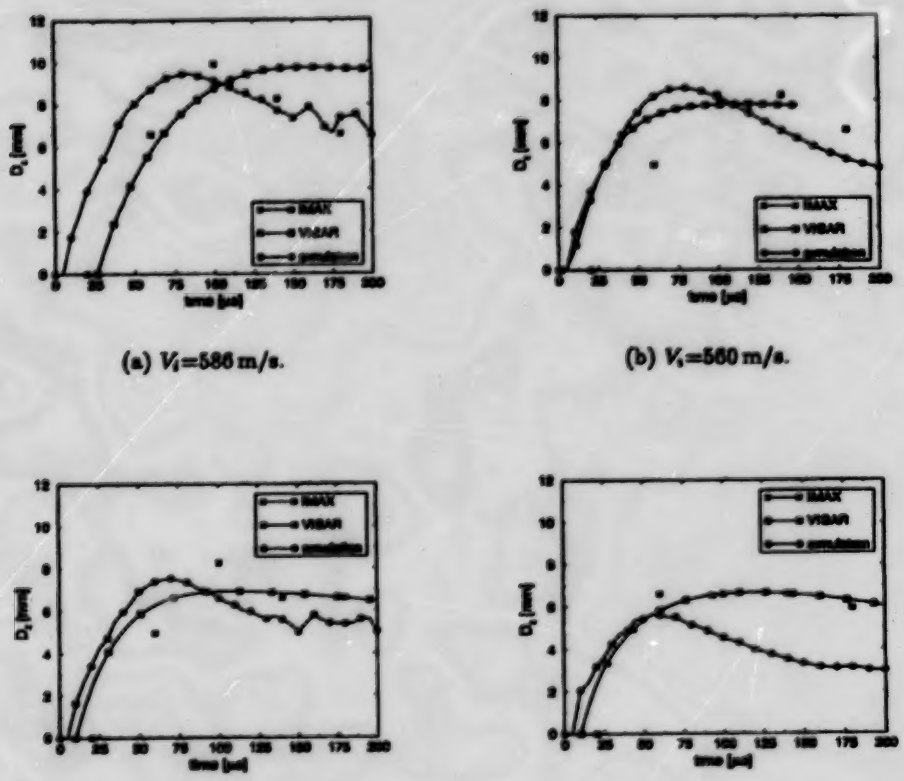

(a) V_i=586 m/s. (b) V_i=560 m/s.

(c) V_i=545 m/s. (d) V_i=483 m/s.

Figure 4.5: Simulated and measured backplane displacement-time histories for Kevlar panels impacted by a 1.1 g FSPs.

The measured and simulated maximum backplane displacement as a function of the FSP impact velocity are presented in Figure 4.6. The figure reiterates the good agreement between the model and the experiments, particularly when one considers the challenges in obtaining accurate and reproducible results for ballistic impact tests.

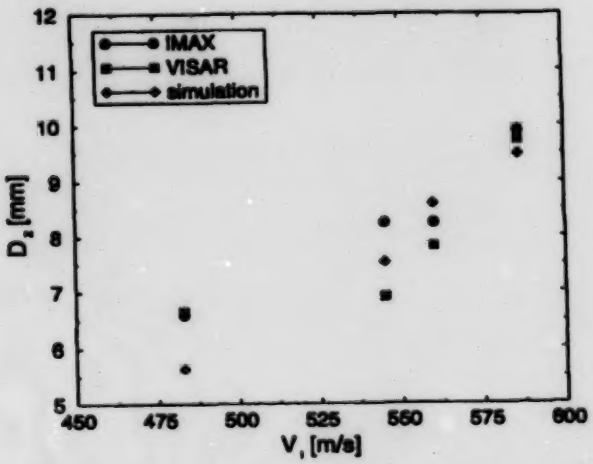

Figure 4.6: Simulated and measured maximum backplane displacement versus impact velocities for Kevlar panels impacted by 1.1 g FSPs.

4.2.2 2.8 g FSP

Figure 4.7 shows a sequence of deformed mesh plots obtained from the simulation of a 2.8 g FSP impacting the Kevlar panel at a velocity of 511 m/s. Similar to the case with the 1.1 g FSP shown in Figure 4.4, the plot at t=10 μs shows the initial stage of the penetration process, at which point a crater was formed by deletion of elements that failed in either the through-thickness compressive or shear damage mode. Delaminations occurred both adjacent to and ahead of the advancing projectile.

The plot at t=125 μs shows the model at maximum backplane deformation, indicating excessive delamination and substantial backplane displacement. Comparing Figure 4.7(c) with Figure 4.4(c), shows that the amount and the extent of delamination failure was more severe for the panel impacted by the 2.8 g FSP. The plot at t=200 μs shows the mesh at the end of the simulation, where the projectile was pushed back upwards by the elastic springback of the backplane. The bottom layers of the backplane were found to continue to separate further from the remainder of the panel after the projectile started to move back upwards. A possible explanation for this would be that the predicted stiffness decrease induced by the damage inside the backplane was too large, so that the bottom layers of the backplane did not springback elastically. Figure 4.7(d) also shows that elements outside the crater area were deleted, probably through shear failure.

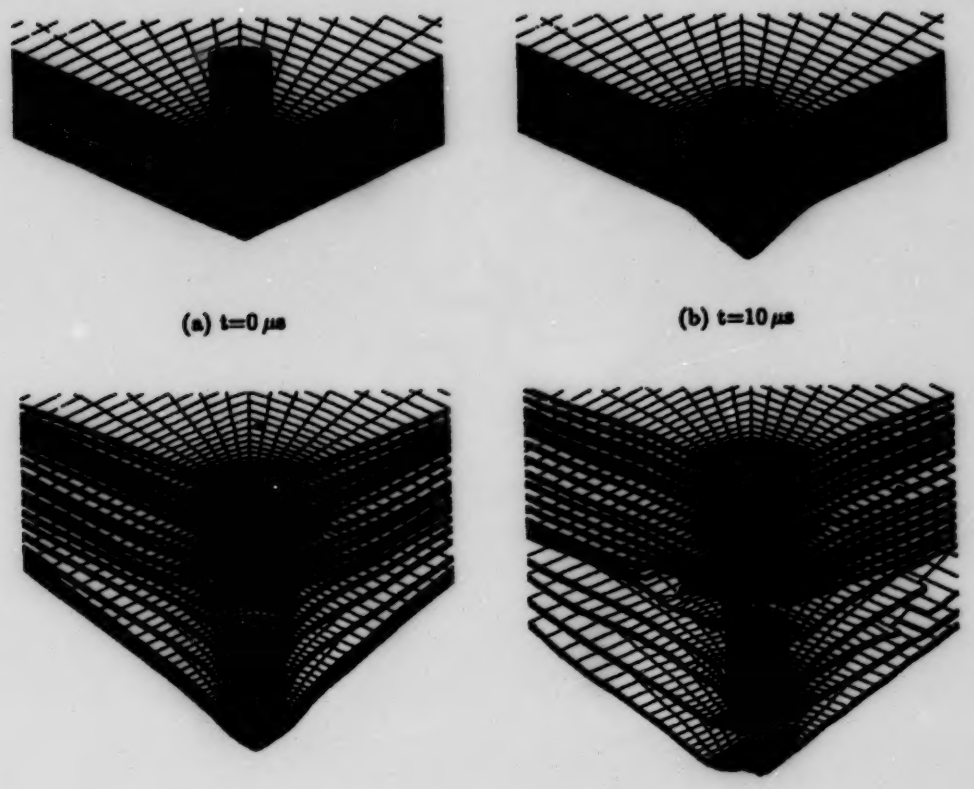

(a) t=0 μs (b) t=10 μs

(c) t=125 μs (d) t=200 μs

Figure 4.7: Sequence of deformed mesh plots of a 2.8 g FSP impacting a Kevlar panel at 511 m/s.

The measured and numerically predicted backplane response of a Kevlar panel impacted by 2.8 g FSPs is shown in Figure 4.8. In general, the model agreement with experiment is quite good; the predicted maximum backplane deformation falling either above or below the measured values, often lying between the VISAR and IMAX values. In most cases, the predicted maximum displacement was within 2 mm of the measured values. The figure further shows that the lower impact velocity measurements also exhibit the pull-back of the backplane at late times as seen in the model predictions for all velocities. The close agreement between the measured and simulated maximum backplane displacement is displayed in Figure 4.9.

Figure 4.8(a) shows that the model overpredicts the measured backplane displacement for the 511 m/s impact velocity. The panel used in the experiment showed extensive delamination and a considerable amount of residual backplane deformation, as was shown in Figures 3.7 and 3.10. However, based on the overprediction of the backplane displacement, the delamination and backplane response in the experiment were probably not as severe as observed in the model in Figure 4.7.

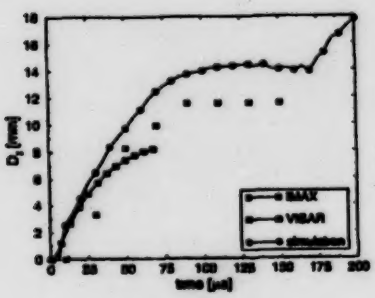

(a) V_i=511 m/s.

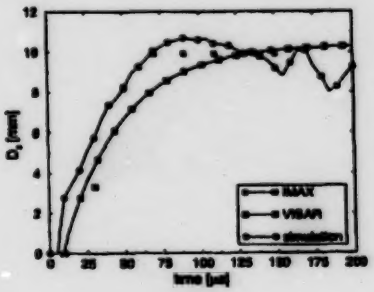

(b) V_i=461 m/s.

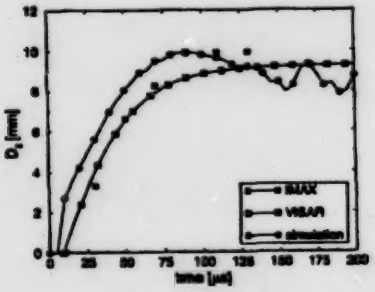

(c) V_i=446 m/s.

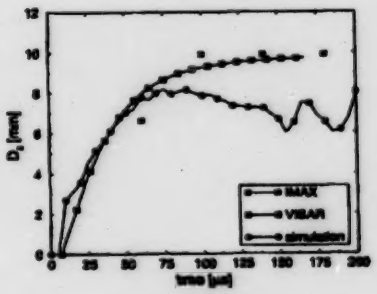

(d) V_i=398 m/s.

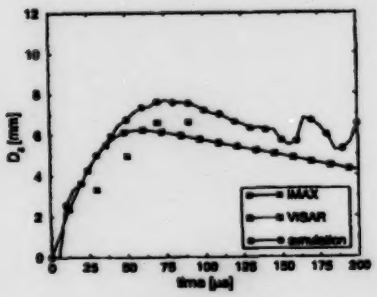

(e) V_i=386 m/s.

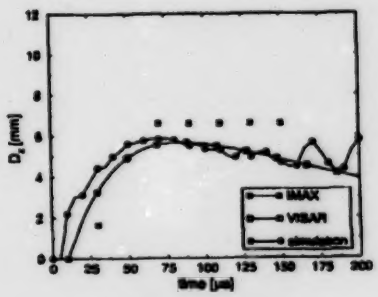

(f) V_i=321 m/s.

Figure 4.8: Simulated and measured backplane displacement-time histories for Kevlar panels impacted by 2.8g FSPs.

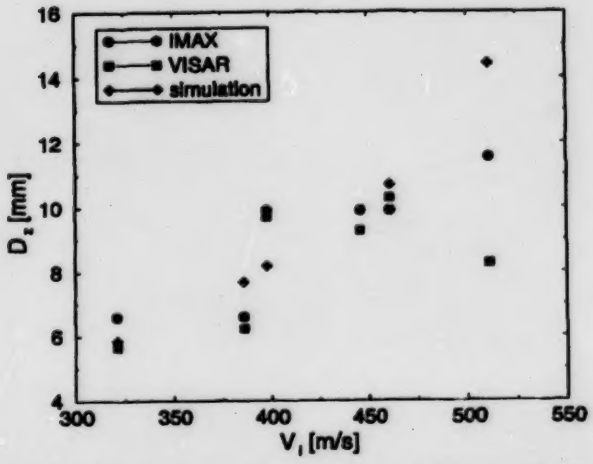

Figure 4.9: Simulated and measured maximum backplane displacement versus impact velocities for Kevlar panels impacted by 2.8 g FSPs.

4.3 Simulation of UBC Series

The following presents the results from simulations of the ballistic impact tests performed at UBC, using the cylindro-conical projectiles. The numerical results were compared with the experimental data obtained from the ELVS System (Section 3.2.1), which was presented in Section 3.4. The results from the tests performed with the flat-nose and sharp-nose cylindro-conical projectiles are presented separately.

4.3.1 Flat-Nose Projectiles

Perforating Shots

Figure 4.10 presents the measured and simulated projectile and backplane response for all flat-nose cylindro-conical projectiles fired at velocities sufficient to cause complete perforation. It was noted in Section 3.4 that the ELVS data analysis software did not compute the correct moment of impact for most cases. The data presented in Section 3.4 was re-analysed to obtain a more accurate moment of impact. The corrected moment of impact was determined as the time at which the measured projectile velocity started to decrease. The experimental curves in Figure 4.10 were obtained by aligning the experimental data so that it started at the corrected moment of impact.

Very good agreement was found between the measured and simulated projectile response, both for the displacement- and velocity-time histories. The backplane displacement was not directly measured during the ballistic tests. The close agreement between the measured and simulated projectile kinematics indicates that the predicted backplane displacement is also accurate.

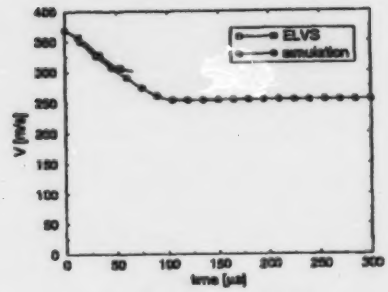

(a) V_i=369 m/s, velocity.

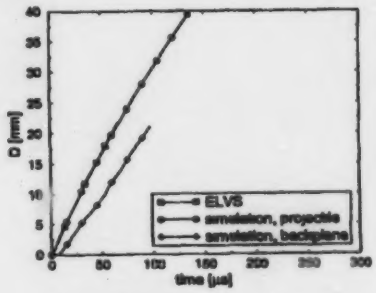

(b) V_i=369 m/s, displacement.

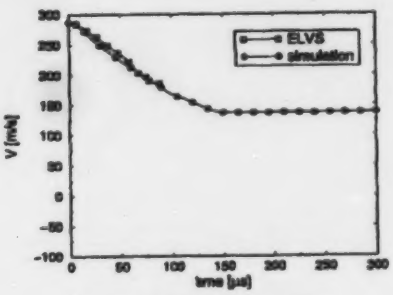

(c) V_i=287 m/s, velocity.

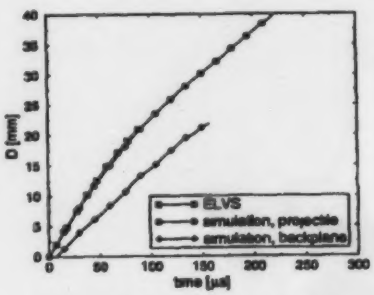

(d) V_i=287 m/s, displacement.

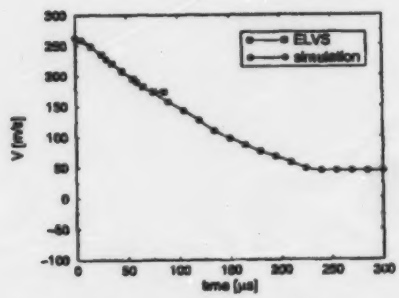

(e) V_i=263 m/s, velocity.

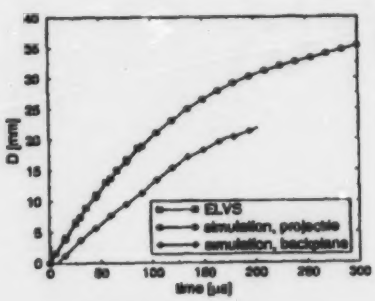

(f) V_i=263 m/s, displacement.

Figure 4.10: Simulated and measured response of flat-nose cylindro-conical projectiles impacting Kevlar panels: perforating shots.

Figure 4.11 shows the measured and simulated exit velocity as function of the impact velocity for flat-nose cylindro-conical projectiles impacting the Kevlar panels. The experimental and numerical data agree fairly well, especially for the higher impact velocities. However, it should be noted that the experimental exit velocity is the velocity at which the projectile exits the ELVS laser beam. For the lower impact velocities, this is not necessarily the velocity at which the projectile exits the panel. At these velocities, the backplane deformation may be sufficiently large that the projectile exits the ELVS laser beam before it perforates the backplane fully. The predicted exit velocity in Figure 4.11 is the velocity at which the projectile exits the panel mesh.

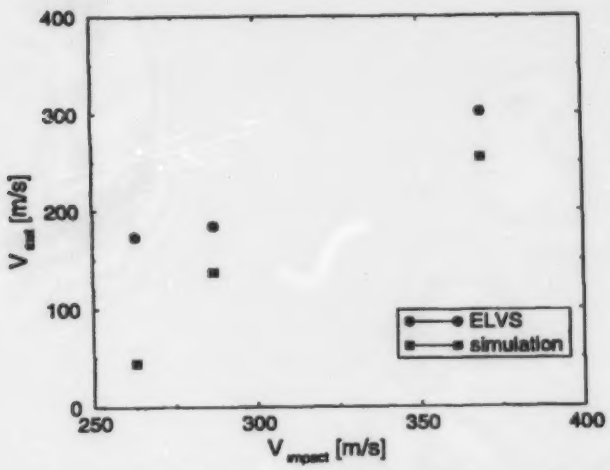

Figure 4.11: Simulated and measured exit velocities versus impact velocities for flat-nose cylindro-conical projectiles impacting Kevlar panels.

Non-Perforating Shots

Figure 4.12 shows the deformed mesh plots obtained from the simulation of the flat-nose cylindro-conical projectile impacting a Kevlar panel at 251 m/s. The plot at t=30 μs shows the initial penetration process with crater formation and initial delamination growth. At t=120 μs, the projectile has perforated most of the panel and the delamination damage is extensive. The plot at t=240 μs shows the mesh just prior to complete perforation of the backplane. In the experiment, the projectile was observed to puncture, but not completely perforate the backplane.

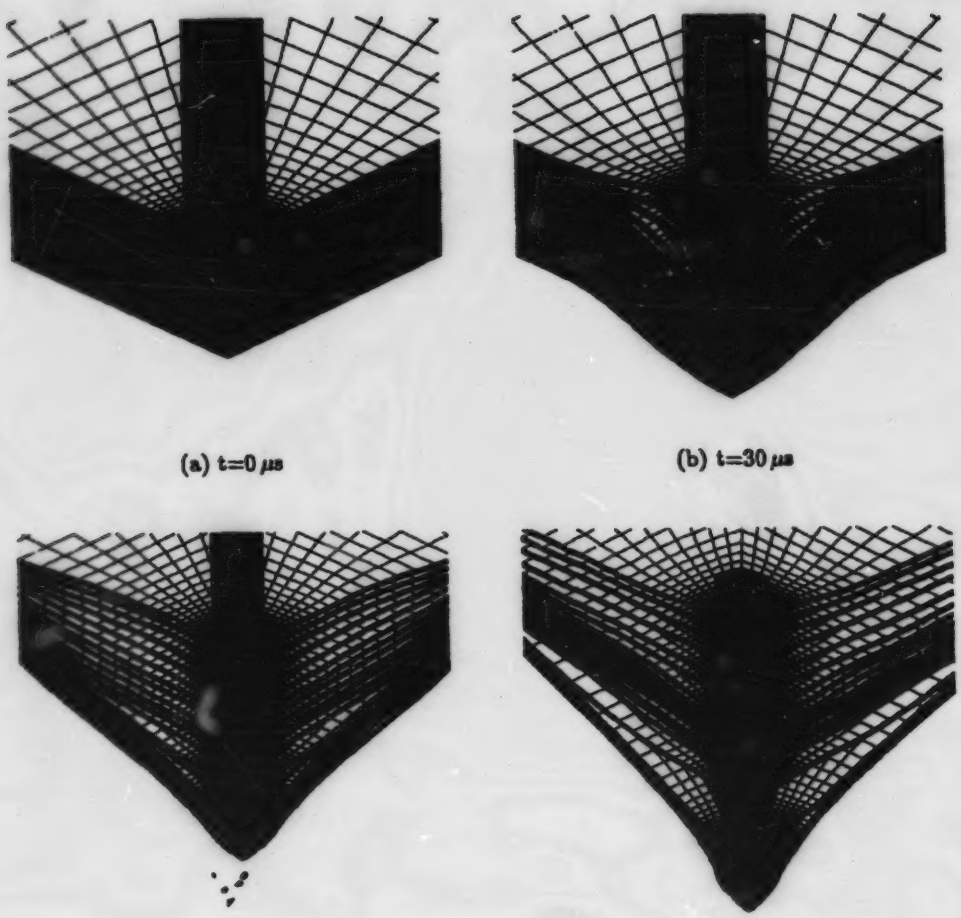

(a) t=0 μs (b) t=30 μs

(c) t=120 μs (d) t=240 μs

Figure 4.12: Sequence of deformed mesh plots for a flat-nose cylindro-conical projectile impacting a Kevlar panel at 251 m/s.

The measured and predicted response of flat-nose cylindro-conical projectiles impacting Kevlar panels is presented in Figures 4.13 and 4.14. Similar to Figure 4.10, a time offset was applied to the experimental data to compensate for the inaccuracy in the moment of impact determined by the ELVS system.

Complete backplane perforation was prevented in all experiments with impact velocities below 251 m/s. The same was the case for the simulations, except for the projectile impacting the panel at 251 m/s. In this case, the model predicted that the projectile exited the panel mesh with a residual velocity of 17 m/s. This is still very close to the experiment, in which the projectile punctured the backplane, but did not completely perforate it.

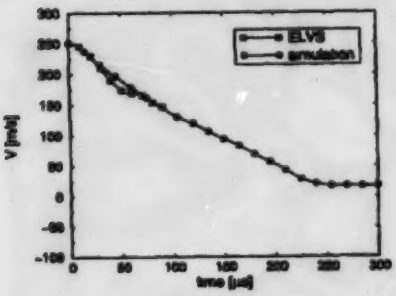

(a) V_i=251 m/s, velocity.

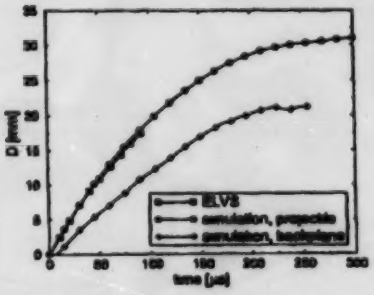

(b) V_i=251 m/s, displacement.

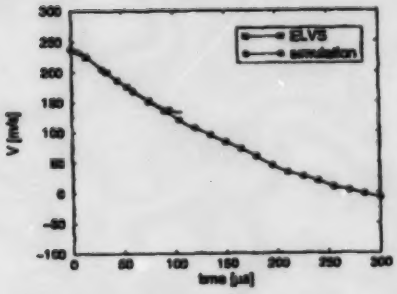

(c) V_i=238 m/s, velocity.

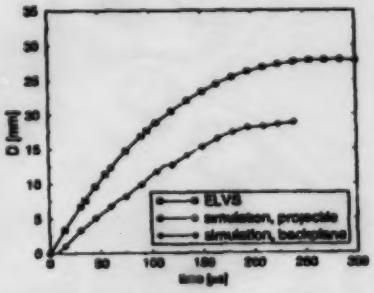

(d) V_i=238 m/s, displacement.

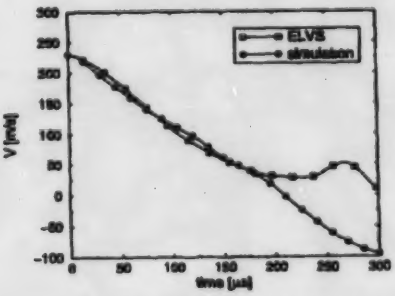

(e) V_i=230 m/s, velocity.

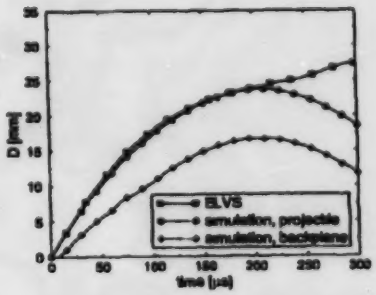

(f) V_i=230 m/s, displacement.

Figure 4.13: Simulated and measured response of flat-nose cylindro-conical projectiles impacting Kevlar panels: non-perforating shots.

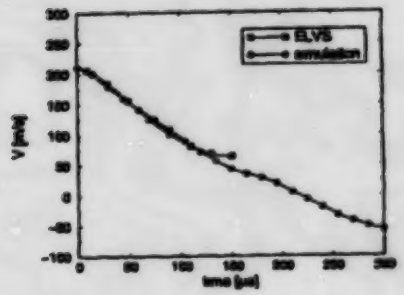

(a) V_i=211 m/s, velocity.

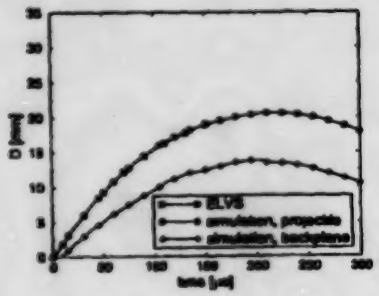

(b) V_i=211 m/s, displacement.

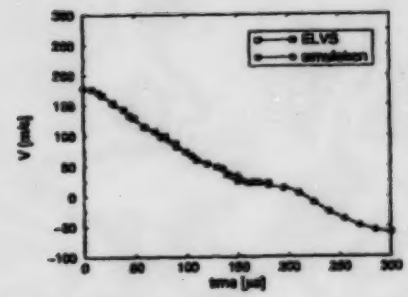

(c) V_i=178 m/s, velocity.

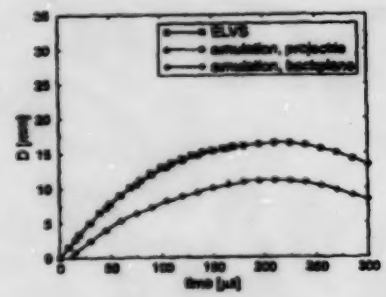

(d) V_i=178 m/s, displacement.

Figure 4.14: Simulated and measured response of flat-nose cylindro-conical projectiles impacting Kevlar panels: non-perforating shots.

The predicted and measured projectile kinematics agree very well. As a result, the backplane displacements are probably predicted with good accuracy as well. Figure 4.15 shows the predicted maximum backplane displacement as function of the impact velocity.

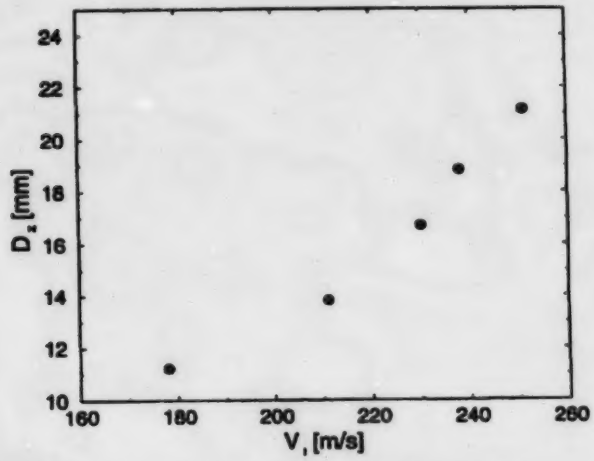

Figure 4.15: Predicted maximum backplane displacement versus impact velocity for flat-nose cylindro-conical projectiles impacting Kevlar panels.

4.3.2 Sharp-Nose Projectiles

Perforating Shots

The measured and simulated response for the sharp-nose cylindro-conical projectiles impacting Kevlar panels is shown in Figure 4.16. The experimental data in the figure was adjusted for the moment of impact. Complete backplane perforation was observed in all experiments and simulations presented in Figure 4.16. The model predicted the projectile kinematics very well, especially for the higher impact velocities.

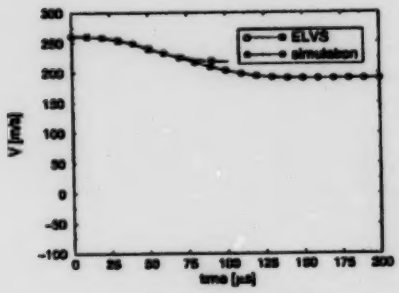

(a) V_i=262 m/s, velocity.

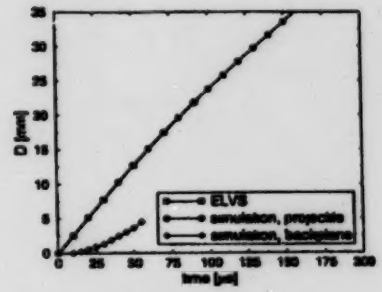

(b) V_i=262 m/s, displacement.

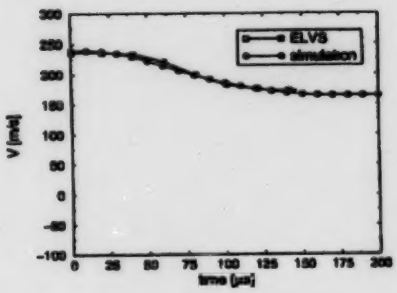

(c) V_i=236 m/s, velocity.

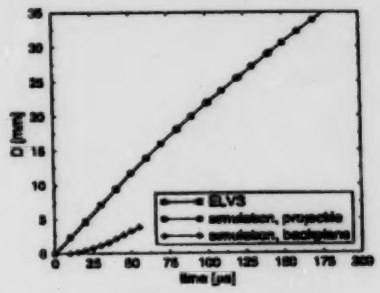

(d) V_i=236 m/s, displacement.

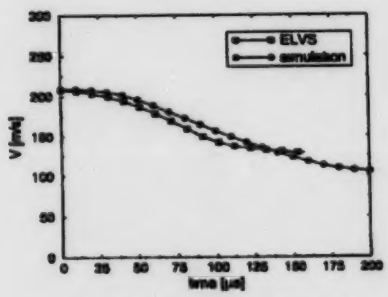

(e) V_i=207 m/s, velocity.

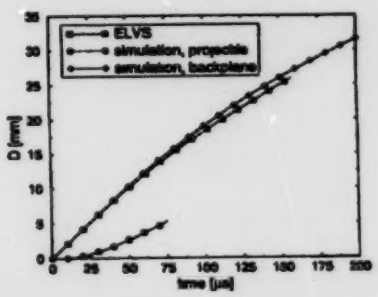

(f) V_i=207 m/s, displacement.

Figure 4.16: Simulated and measured response of sharp-nose cylindro-conical projectiles impacting Kevlar panels: perforating shots.

Figure 4.17 presents the measured and simulated projectile exit versus impact velocities. The experimental and numerical data agree fairly well. The model underpredicted the exit velocity in all cases.

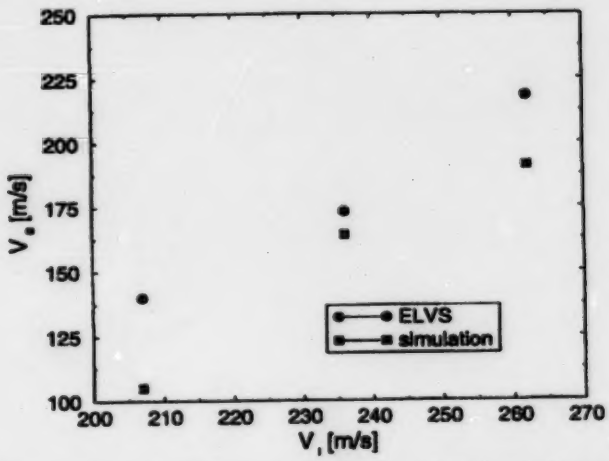

Figure 4.17: Simulated and measured exit velocities versus impact velocities for sharp-nose cylindro-conical projectiles impacting Kevlar panels.

Non-Perforating Shots

Figure 4.18 shows deformed mesh plots obtained from the simulation of a sharp-nose cylindro-conical projectile impacting a Kevlar panel at 155 m/s. The plot at t=50 μs characterises the initial penetration process, with crater formation and the initiation of delamination. Figure 4.18(c) presents the mesh just prior to the occurrence of backplane perforation. This figure also shows that up until that moment, the sharp projectile mainly caused penetration failure with little delamination. The plot at t=360 μs shows the mesh at maximum projectile penetration. The projectile was found to rebound afterwards. In the experiment, the projectile punctured the backplane, but rebounded before completely perforating the backplane. Comparing Figure 4.18(b) with Figures 4.18(c) and 4.18(d) shows that the passage of the cylindrical part of the projectile through the crater resulted in a substantial increase in the extent of delamination failure. The predicted deformation and delamination of the panel mesh was much more substantial than observed in the experiment.

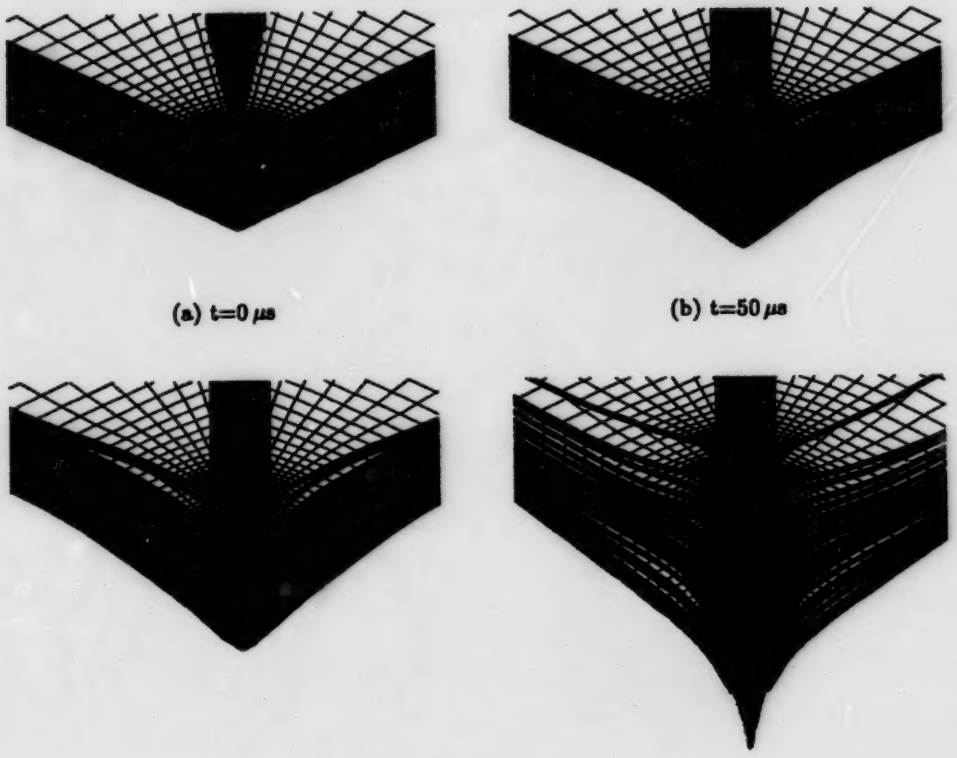

(a) t=0 μs (b) t=50 μs

(c) t=100 μs (d) t=360 μs

Figure 4.18: Sequence of deformed mesh plots from the simulation of a sharp-nose cylindro-conical projectile impacting a Kevlar panel at 155 m/s.

The measured and predicted response for the sharp-nose cylindro-conical projectile impacting a Kevlar panel at 155 m/s is presented in Figure 4.19. The data obtained from the ELVS shows that the projectile was stopped by the panel and rebounded. The model also predicted rebounding of the projectile, but the predicted projectile displacements deviate from the measurements after about 125 μs. Consequently, the predicted and measured projectile velocities differ as well. The predicted maximum projectile displacement is larger than measured with the ELVS. Overall, the agreement between the predictions and the measurements is reasonably good.

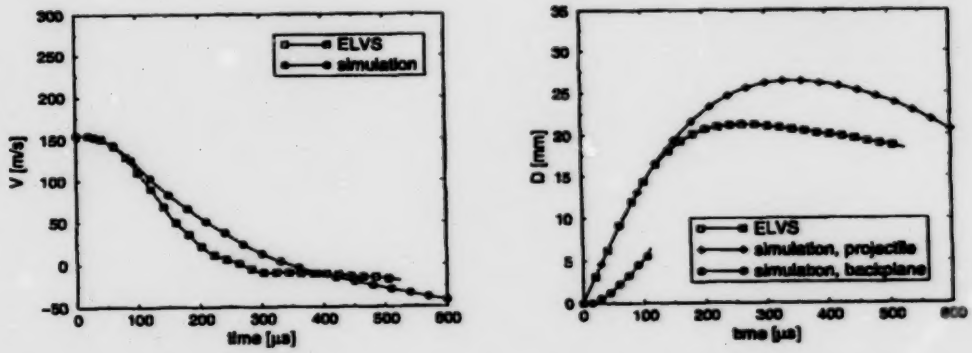

(a) V_i=155 m/s, velocity. (b) V_i=155 m/s, displacement.

Figure 4.19: Simulated and measured response of sharp-nose cylindro-conical projectiles impacting Kevlar panels: non-perforating shots.

Chapter 5

Discussion

Research into the ballistic impact response of laminated composites is still largely empirical, with the main focus on the prevention of projectile penetration. This empirical approach results in high costs involved in the design and testing of improved ballistic protection against more severe threats and in the application of new materials. Further, due to the emphasis on the penetration response of the composite, the deformation of the laminate is usually ignored.

However, in personal protective items for ballistic impact, such as vests and helmets, the deformation response of the composite is of vital importance since the protective item is positioned close to or even against the human body. The research presented in this report has focused on the deformation response of the ballistic helmet, for which the impact of the delaminated backplane with the head is considered to be a possible cause of skull fracture and underlying brain damage.

A numerical model was developed as part of this research to provide a fast and relatively inexpensive means of gaining insight into the parameters governing the penetration and deformation response of laminated helmets subjected to ballistic impact. The model can be used to further assess the degree of improvement in performance of current ballistic protection offered by design changes and the use of new materials.

5.1 Numerical Parameters

The effects of the various model parameters on the predicted ballistic response were evaluated extensively. It was found that the use of a post-failure approach led to a more realistic and numerically more stable response than when an instantaneous failure model was used. The through-thickness shear properties used in the numerical model were found to have a large effect on the predicted ballistic response.

The numerical simulations exhibited a considerable degree of hourglassing and the stiffness hourglass control proved to be the most efficient way of controlling this numerical artifact. However, stiffness hourglass control also stiffened the response of the model, resulting in smaller backplane predictions.

The numerical predictions were highly sensitive to the applied mesh definition. Increases in both the in-plane and through-thickness mesh density resulted in substantial changes in the predicted response. Doubling the number of through-thickness elements per ply also significantly reduced the degree of hourglassing. The post-failure model was found to be less mesh-sensitive than the instantaneous failure model.

5.2 Simulation of Ballistic Impact Tests

A number of ballistic impact tests were performed to evaluate the accuracy and limitations of the numerical model. In these tests, woven Kevlar laminated panels were impacted by different types of projectiles with a range of impact velocities. Initially, material properties obtained from quasi-static tests presented in the literature were utilised in the numerical model. However, the use of these material properties resulted in large discrepancies between the numerically predicted and measured ballistic response of the panels. The quasi-static nature of many of the adopted material properties was considered to be the cause of this discrepancy.

As described in Section 4.1.2, dynamic data on Kevlar composites is rare and difficult to measure. As an interim solution for the purpose of this research, it was decided to modify some of the material properties in the numerical model to obtain a closer agreement between simulations and experiments. In the future, however, the dynamic response of the woven Kevlar material needs to be characterised experimentally and strain rate effects need to be accounted for in the numerical model.

The numerical material model was "calibrated" for one particular impact condition, namely a 1.1 g FSP impacting a Kevlar panel at 586 m/s. The results of the parametric study presented in Section 2.6 were used to guide the changes in the numerical material properties in order to obtain a closer agreement between the model and the experiments. It was found that changing the through-thickness shear properties and using more realistic values for the in-plane tensile strengths resulted in accurate predictions for the 1.1 g FSP impacting at 586 m/s.

These "calibrated" numerical material properties were held constant and used in the simulations of the other ballistic impacts. In this manner, the choice of the modified numerical material parameters could be assessed for a range of impactor masses, geometries, and impact velocities. For the panels impacted by the four types of projectiles considered in this study, the model predicted the measured maximum backplane displacement accurately. When the experimental data obtained from the impacts was adjusted for the moment of impact, the numerical predictions and experimental data agreed very well, especially when one considers the limited accuracy and reproducibility associated with ballistic impact testing.

5.3 Trends in Measurements and Predictions

Figure 5.1 presents the measured and predicted maximum backplane displacement as function of the incident energy for the range of projectiles used in this study. No backplane displacements were measured during the UBC Series, since the ELVS only captured the response of the projectile during the impact. Further, the simulations with the sharp-nose cylindro-conical projectiles resulted in complete perforation of the panel mesh in all simulated cases. Consequently, the only results related to the UBC Series in Figure 5.1 are the predicted maximum backplane displacements of the non-perforating shots with the flat-nose cylindro-conical projectiles.

For interpretation purposes, a line was fit through the numerical results in Figure 5.1. Two measurements are plotted for each FSP, obtained from the IMAX and the VISAR systems. The figure shows that the scatter in the three sets of measured data is smaller for the 1.1 g FSPs than for the 2.8 g FSPs. Figure 5.1 also indicates that the relation between the maximum backplane displacement and impact energy can be approximated to be nearly linear for each projectile type, at least within

the range of impact energies used in this report. The figure further shows that the global agreement between the measured and predicted data is good.

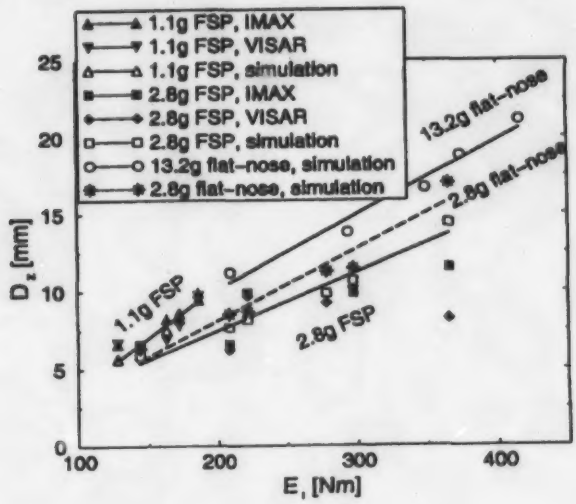

Figure 5.1: Measured and predicted maximum backplane displacement as function of incident energy for a range of projectiles.

The different trends observed for each type of projectile in Figure 5.1 are likely due to the differences in the projectile characteristics. The characteristic measurements of the projectiles are summarised in Table 5.1.

Table 5.1: Projectile Characteristics

	Mass [g]	Diameter [mm]	Length [mm]
1.1 g FSP	1.1	5.46	6.35
2.8 g FSP	2.8	7.52	8.84
flat-nose	13.2	7.56	46

Figure 5.1 shows that for the same level of incident energy, the 1.1 g FSP results in a higher maximum backplane displacement than the 2.8 g FSP. The shape of the impacting ends of these two types of FSPs are the same, but Table 5.1 shows that the 2.8 g FSP is heavier and has a larger diameter. Figure 5.1 also shows that for the same levels of incident energy, the flat-nose cylindro-conical projectiles cause higher backplane displacements than the 2.8 g FSPs. It can be observed from Table 5.1 that the diameter of the flat-nose cylindro-conical projectile and the 2.8 g FSP are similar, but that the flat-nose cylindro-conical projectile has a much higher mass. Further, the impacting end of the flat-nose cylindro-conical projectile is sharper than for the 2.8 g FSP.

The differences in the backplane response between the various projectiles indicates that the amount of backplane displacement is probably mainly dependent on the projectile mass and on the profile of the projectile tip. Within the context of this report, the projectile tip profile is defined by the projected surface area of the projectile tip and the gradient of the projected surface area over the length of the tip. The projected surface area is defined as the surface area of the largest cross-section of the projectile that has penetrated the target. A smaller projected surface area facilitates the penetration process, resulting in a thinner backplane. A thinner backplane is more flexible and, therefore, results in a higher backplane displacement. A gradual change in the projected surface area as the projectile tip penetrates the target also decreases the penetration resistance, resulting in a thinner backplane and a higher backplane displacement.

For the FSPs, the impacting surface is fairly flat and changes only a little over the length of the projectile tip. The 1.1 g FSP has a smaller diameter than the 2.8 g FSP, resulting in a smaller projected surface area. Figure 5.1 shows that the smaller projected surface area of the 1.1 g FSP resulted in a higher maximum backplane

displacement. The 2.8 g FSP and flat-nose cylindro-conical projectile had different masses and different tip profiles. The effects of the projectile mass and the tip profile were differentiated by simulating the impact of a flat-nose conical projectile with the same mass and impact velocities as the 2.8 g FSPs. No experimental data was available to support these simulations, but since the experiments and simulations presented in this report agreed very well, the model was considered to be capable of accurately predicting the 2.8 g flat-nose impact.

The results obtained from the simulated impacts with the 2.8 g flat-nose projectile are also shown in Figure 5.1. The figure shows that at equal mass and impact velocity, the flat-nose projectile resulted in higher maximum backplane displacements than the 2.8 g FSP. The sharp tip of the flat-nose projectile has a smaller initial projected surface area and a more gradual increase in the projected surface area as the projectile penetrates the panel than the FSP. This results in a lower penetration resistance for the flat-nose projectile, which yields a thinner backplane with a larger deflection. The lines fit through the predictions for the 13.2 g and 2.8 g flat-nose projectiles indicate that an increase in projectile weight results in a linear shift in the maximum backplane displacement, with the heavier projectile causing the largest backplane displacements.

If one extrapolates the line fit through the 1.1 g FSP data, a higher backplane displacement will be found for the 1.1 g FSP than for the flat-nose cylindro-conical projectile, at the same level of incident energy. This is in agreement with the above statement, since the diameter of the 1.1 g FSP is smaller than for the flat-nose cylindro-conical projectile, resulting in a smaller projected surface area for the 1.1 g FSP. For the cylindro-conical projectiles, the change in the projected surface area is directly related to the conical angle. The smaller conical angle for the sharp-nose cylindro-conical projectile results in a smaller increase in the projected impacting

surface area with further penetration of the cone than is the case for the flat-nose projectile. The gradual increase in projected surface area facilitates the penetration of the projectile, which explains why the Kevlar panels had problems stopping the sharp-nose cylindro-conical projectiles.

5.4 Current Limitations of the Model

The extent of delamination in the numerical simulations was in some cases much larger than observed in the experiments. This can be partly attributed to the quasi-static nature of the applied delamination strength data in the numerical model. However, the choice of mesh definition also plays an important role in determining the predicted extent of delamination. A fan-mesh was utilised to accommodate a high mesh density in the crater area together with larger elements outside the crater, to reduce the computational time. Consequently, the mesh size differed considerably over the radius of a delamination. The observed strong mesh-sensitivity of the simulations indicates that delamination growth will also depend upon the size of the delaminating elements.

The discrete delamination interface is based on a strength of materials approach, predicting failure by relating the interfacial stresses to critical values. However, it was noted in Section 1.5.1 that the strength of materials approach is only suitable to predict delamination initiation. A fracture mechanics approach would be more suitable to predict delamination growth. However, the extensive amount of work involved in the implementation of a fracture mechanics approach in the current numerical model, together with the problems related to numerical fracture mechanics mentioned in Section 1.6.2 prevented further research in this direction. Nevertheless, a fracture mechanics approach to predict delamination growth should be considered

in the future.

Both non-destructive and destructive techniques have been applied to visualise the amount and extent of damage within the impacted panels. However, none of these efforts were successful. Non-invasive techniques, such as ultra-sound and X-ray, could not provide a clear picture of the extent of delamination inside the panels. Cutting the panels in the crater area resulted in irregular surfaces due to the frayed fibres and it was not clear if all of the internal damage was caused by the impact or partially by the cutting of the panel. On the other hand, the numerical model could be easily modified to output the required data for damage visualisation. The experimental characterisation of damage needs to be further explored, so that the model can be validated for its capacity to predict the damage state of the laminates. To this end, other material systems, with better defined delamination planes, should be considered in future work.

Chapter 6

Conclusions

The following conclusions can be reached from the work presented in this report:

1. The numerical model was capable of accurately predicting the penetration and backplane response of ballistically impacted composites. Good agreement was found between the predicted and measured response of woven Kevlar-29 laminated panels, using different types of projectiles with a range of impact velocities.

2. The experimental and numerical results indicate that the relationship between the maximum backplane displacement and the impact energy is nearly linear, at least within the range of impact energies considered.

3. It proved necessary to modify several quasi-static material parameters obtained from the literature in order to obtain better agreement between the numerical and experimental results. Doubling the through-thickness shear strengths ($S_{23,31}$) and halving the through-thickness shear moduli ($G_{23,31}$) resulted in close agreement between the predictions and measurements for the range of projectiles and impact velocities considered.

4. A parametric study, in which the characteristics of the model were varied, revealed that the through-thickness material properties ($G_{23,31}$, $S_{23,31}$) of the model had the largest effect on the predicted ballistic response.

5. Post-failure modelling was found to substantially improve the accuracy and reduce the mesh-sensitivity of the numerical model, compared to the use of an instantaneous failure model.

6. The mesh sensitivity of the numerical predictions remains an issue to be addressed in future work.

Chapter 7

Recommendations

The present research has provided a thoroughly evaluated numerical model for the prediction of the ballistic response of laminated composites. Despite the good agreement between the numerical predictions and the experimental data, there exists a need for further research in this area.

Because of their quasi-static nature, the material parameters applied in the numerical model had to be adjusted to obtain closer agreement between the numerical predictions and the measured response of ballistically impacted laminates. In the future, the dynamic response of the woven Kevlar material needs to be characterised and strain rate effects need to be accounted for in the numerical model.

Despite the observations made in Section 1.4 that delaminations are closely related to matrix cracking, coupling effects between matrix cracking and delamination were not accounted for in the numerical model. Therefore, the numerical model should be extended to accommodate direct coupling between matrix cracks that extend all the way to ply interfaces and the initiation of delamination.

Further, the application of a fracture mechanics approach to simulate delamination growth would likely improve the accuracy of the predicted extent of the delaminations. However, care should be taken regarding the mesh-sensitivity of the delamination growth criteria (Section 1.6.2).

Since the numerically predicted response was found to be affected by the applied mesh definition, a non-local damage approach should be applied to decrease the mesh-sensitivity of the simulations. The purpose of introducing a nonlocal concept for damage is to limit the localisation of strain softening to a zone of a certain minimum size that is a material property (Pijaudier-Cabot and Bažant, 1987). The size of the strain softening zone is represented by a characteristic length scale and the damage in the elements inside this length scale is smeared out using a weighted averaging technique.

Even though the experimental data presented in this report is valuable, a few modifications can be recommended for future testing. The impacts close to the ballistic limits for the various projectiles showed delaminations extending to the edges of the panel. This indicates that the support conditions influenced the measured backplane deformation. This was particularly noticeable for the panels impacted by the flat-nose cylindro-conical projectiles, where the backplane deformation was observed to have been restricted by the support conditions.

The ELVS measurements only provided information on the projectile response. In general, the projectiles exited the ELVS laser beam before the backplane reached its maximum deformation. Consequently, limited information on the backplane deformation could be obtained from these tests. In the future, an ELVS system should be positioned both in front and behind the panel, so that measurements can be made of both the projectile and backplane kinematics.

The limited resolution in the IMAX images resulted in a limited amount of data with questionable accuracy. For future purposes, a regular IMACON or any other high-speed camera would probably result in a more accurate visualisation of the backplane deformation.

The main focus of the current study was develop to a numerical model capable of predicting the backplane response of laminated ballistic helmets. This report has shown that the model accurately predicts ballistic response of laminated panels. Planned follow-on work to this research will involve the simulation of ballistic impacts on helmets. The curved shaped of the helmets will definitely have an effect on the deformation and backplane response of the laminate.

Simulations of ballistic impacts on helmeted heads are also to be performed. Figure 7.1 shows the model that will be used for these simulations, which incorporates a detailed model of the human skull and brain. This model will eventually permit prediction of trauma due to impact of the backplane with the head.

Figure 7.1: Helmet model developed at Carleton University together with ESI Head Model.

References

Abdel-Rahman, N., Starratt, D., Pageau, G., Zhang, Y., Vaziri, R., and Poursartip, A., 1998, "Experimental and Theoretical Investigation of the Ballistic Impact of Textile Materials," in: *Proceedings of the Personal Armour Systems Symposium 1998*, Colchester, UK, pp. 213–222.

Abrate, S., 1991, "Impact on laminated composite materials," *Applied Mechanics Review*, Vol. 44, No. 4, pp. 155–90.

Agarwal, B. and Broutman, L., 1990, *Analysis and Performance of Fiber Composites*, 2nd edn., John Wiley and Sons, Inc., New York, New York.

Allix, O. and Ladevèze, P., 1992, "Interlaminar interface modeling for the prediction of delamination," *Composite Structures*, Vol. 22, pp. 235–42.

Allix, O., Ladevèze, P., and Corigliano, A., 1995, "Damage analysis of interlaminar fracture specimens," *Composite Structures*, Vol. 31, No. 1, pp. 61–74.

Allix, O., Ladevèze, P., and Vittecoq, E., 1994, "Modeling and identification of the mechanical behavior of composite laminates in compression," *Composites Science and Technology*, Vol. 51, No. 1, pp. 35–42.

Anderson, C. and Bodner, S., 1998, "Ballistic impact: the status of analytical and numerical modelling," *International Journal of Impact Engineering*, Vol. 7, No. 1, pp. 9–35.

Andrews, M., Lu, D., and Young, R., 1997, "Compressive properties of aramid fibres," *Polymer*, Vol. 38, No. 10, pp. 2379–2388.

ASTM D 2344-84, 1997, *Annual Book of ASTM Standards*, Vol. 15.03, Chap. Standard Test Method for Apparent Interlaminar Shear Strength of Parallel Fiber Composites by Short-Beam Method, American Society for Testing and Materials, Philadelphia, PA, pp. 43–45.

ASTM D 5528-94a, 1997, *Annual Book of ASTM Standards*, Vol. 15.03, Chap. Standard test method for mode I interlaminar fracture toughness of unidirectional fiber-reinforced polymer matrix composites, American Society for Testing and Materials, Philadelphia, PA, pp. 280–9.

Atallah, K. and Galiotis, C., 1993, "Fibre strain mapping in aramid/epoxy microcomposites," *Composites*, Vol. 24, No. 8, pp. 635–42.

Audoin, B. and Baste, S., 1994, "Ultrasonic evaluation of stiffness tensor changes and associated anisotropic damage in a ceramic matrix composite," *Journal of Applied Mechanics*, Vol. 61, pp. 309–16.

Barsoum, R., 1989, "Finite element application in the fracture analysis of composite materials - Delamination," *Key Engineering Materials*, Vol. 37, pp. 35–57.

Bolotin, V., 1996, "Delaminations in composite structures: its origin, buckling, growth and stability," *Composites: Part B*, Vol. 27B, pp. 129–145.

Brewer, J. and Lagace, P., 1988, "Quadratic Stress Criterion for Initiation of Delamination," *Journal of Composite Materials*, Vol. 22, pp. 1141–51.

Briscoe, B., Court, R., and Williams, D., 1993, "The effects of fabric weave and surface texture on the interlaminar fracture toughness of aramid/epoxy laminates," *Composites Science and Technology*, Vol. 47, pp. 261–270.

Briscoe, B. and Williams, D., 1993, "Interlaminar fracture toughness of aramid/epoxy laminates," *Composites Science and Technology*, Vol. 46, pp. 277–86.

Brown, J. and Mathys, Z., 1997, "Plasma surface modification of advanced organic

fibres. Part V Effects on the mechanical properties of aramid/phenolic composites," *Journal of Materials Science*, Vol. 32, pp. 2599–2604.

Cepuš, E., Shahkarami, A., Vaziri, R., and Poursartip, A., 1999, "Effect of Boundary Conditions on the Ballistic Response of Textile Structures," in: *Proceedings of the 12th International Conference on Composite Materials*, Vol. Composite Structures - Characterisation, Paris, FR.

Chang, F.-K. and Chang, K.-Y., 1987a, "Post-failure analysis of bolted composite joints in tension or shear-out mode failure," *Journal of Composite Materials*, Vol. 21, pp. 809–33.

Chang, F.-K. and Chang, K.-Y., 1987b, "A progressive damage model for laminated composites containing stress concentrations," *Journal of Composite Materials*, Vol. 21, pp. 834–55.

Charalambides, M. and Williams, J., 1995, "Fracture Toughness Characterization of Phenolic Resin and Its Composites," *Polymer Composites,*, Vol. 16, No. 1, pp. 17–28.

Chen, H. and Jang, B., 1995, "Failure Mechanisms of 2-D and 3-D Woven Fiber Reinforced Polymer Composites," *Polymer Composites*, Vol. 16, No. 2, pp. 125–34.

Choi, H. and Chang, F., 1992, "A model for predicting damage in graphite/epoxy laminated composites resulting from low-velocity impact," *Journal of Composite Materials*, Vol. 26, No. 14, pp. 2134–69.

Choi, H., Downs, R., and Chang, F., 1991a, "A new approach toward understanding damage mechanisms and mechanics of laminate composites due to low-velocity impact: Part I – Experiments," *Journal of Composite Materials*, Vol. 25, pp. 992–1011.

Choi, H., Downs, R., and Chang, F., 1991b, "A new approach toward understanding damage mechanisms and mechanics of laminate composites due to low-velocity

impact: Part II – Analysis," *Journal of Composite Materials*, Vol. 25, pp. 1011–38.

Chu, S. and Hong, C., 1990, "Application of the J_k integral to mixed mode crack problems for anisotropic composite laminates," *Engineering Fracture Mechanics*, Vol. 35, pp. 1093–103.

Coleman, B. and Gurtin, M., 1967, "Thermodynamics with internal variables," *Journal of Chemistry and Physics*, Vol. 47, pp. 597–613.

Critescu, N., Malvern, L., and Sierakowski, R., 1975, "Failure mechanisms in composite plates impacted by blunt-ended penetrators," in: *Foreign Object Impact Damage to Composites*, American Society for Testing and Materials, pp. 159–172.

Daniel, I. and Wooh, S.-C., 1990, "Deformation and damage of composite laminates under impact loading," *American Society of Mechanical Engineers*, Vol. ASME AMD 116, pp. 11–26.

Daudeville, L., Allix, O., and Ladeveze, P., 1995, "Delamination analysis by damage mechanics: Some applications," *Composites Engineering*, Vol. 5, No. 1, pp. 17–24.

Dobyns, A., 1980, "Analysis of Simply-Supported Orthotropic Plates Subject to Static and Dynamic Loads," in: *Proceedings of the 21st Structural Dynamic Materials Conference*, Seatle, WA, USA, pp. 201–209.

Dost, E., Ilcewics, L., and Gosse, J., 1988, "Sublaminate stability based modelling of impact-damaged composite laminates," in: *Proceedings of the American Society for Composites 3rd Technical Conference on Composite Materials*, pp. 334–41.

Edlund, A., 1993, "Finite Element Modelling of Low Velocity Impact Damage in Composite Laminates," in: *Proceedings of the 9th International Conference on Composite Materials*, pp. 334–41.

Frissen, R., Govaert, L., and Peijs, T., 1995, "Modelling of the Ballistic Impact Behaviour of Polyethylene-Fibre Reinforced Composites," in: *Proceedings of ICCM-*

10, Whistler, BC, Canada, pp. V759–766.

Fuoss, E., 1996, "Effects of stacking sequence on the impact resistance of composite laminates," M.S. Thesis, Carleton University, Ottawa, On., Canada.

Galasso, F., 1989, *Advanced Fibers and Composites*, Gordon and Breach Science Publishers, New York.

Galbraith, C., 1998, *Sheet Metal Forming Simulation Using LS-DYNA*, Metal Forming Analysis Corporation.

Garg, A., 1988, "Delamination – A damage mode in composite structures," *Engineering Fracture Mechanics*, Vol. 29, pp. 557–84.

Germain, P., Ngyuen, Q., and Suquet, P., 1983, "Continuum Thermodynamics," *Journal of Applied Mechanics*, Vol. 50, pp. 1010–20.

Goldsmith, W., Dharan, C., and Chang, H., 1995, "Quasi-static and ballistic perforation of carbon fiber laminates," *International Journal of Solids and Structures*, Vol. 32, No. 1, pp. 89–103.

Gosse, J. and Mori, P., 1988, "Impact damage characterization of graphite/epoxy laminates," in: *Proceedings of the Review of Progress in Quantitative Nondestructive Evaluation*, pp. 1651–1655.

Gosse, J., Mori, P., and Avery, W., 1988, "The relationship between impact-induced stress states and damage initiation and growth in composite plates," in: *Proceedings of the 20th International SAMPE Technical Conference*, pp. 187–193.

Gosse, J. and Sorscher, S., 1988, "An Integrated Damage Analysis of Laminated Composite Plates," in: *Proceedings of the American Society for Composites 3rd Technical Conference on Composite Materials*, pp. 344–53.

Griffith, A., 1920, "The phenomenon of rupture and flow in solids," *Philosophical Transactions of the Royal Society*, Vol. A-221, pp. 163–97.

Hahn, H., 1983, "A mixed mode fracture criterion for composite materials," *Com-*

posites Technology Review, Vol. 5, pp. 26–9.

Hallquist, J., 1993, *LS-DYNA THEORETICAL MANUAL, Rev. 2*, Livermore Software Technology Corporation.

Hansen, N. and Schreyer, H., 1994, "A thermodynamically consistent framework for theories of elastoplasticity coupled with damage," *International Journal of Solids and Structures*, Vol. 3, pp. 359–89.

Hashin, Z., 1980, "Failure criteria for unidirectional fiber composites," *Journal of Applied Mechanics*, Vol. 47, pp. 329–34.

Hill, R. and Okoroafor, E., 1994, "Surface conditions of Kevlar and glass and mechanical properties studied by Weibull statistics and acoustic emission," *Composites*, Vol. 25, No. 10, pp. 913–916.

Hitchings, D., Robinson, P., and Javidrad, F., 1994, "A finite element model for delamination propagation in composites," *Computers and Structures*, Vol. 60, No. 6, pp. 1093–1104.

Hong, S. and Liu, D., 1989, "On the Relationship between Impact Energy and Delamination Area," *Experimental Mechanics*, Vol. 29, pp. 115–120.

Hull, D. and Shi, Y., 1993, "Damage mechanism characterization in composite damage tolerance investigations," *Composite Structures*, Vol. 23, pp. 99–120.

Hung, K.-S., Nilsson, L., and Zhong, Z.-H., 1995, "Numerical studies on the delamination mechanism in laminated composites under impact," in: *Proceedings of ICCM-10*, Whistler, BC, Canada, pp. 623–30.

I-DEAS Master Series 6, 1998, *I-DEAS Master Series 6*, Structural Dynamics Research Corporation.

Jensen, H., 1993, "Numerical method for delamination in composites," *Computational Materials Science*, Vol. 1, No. 3, pp. 319–24.

Jih, C. and Sun, C., 1994, "Prediction of delamination in composite laminates

subjected to low velocity impact," *Journal of Composite Materials*, Vol. 27, No. 7, pp. 684–701.

Jirasek, M. and Bažant, Z. P., 1994, "Localization Analysis of Nonlocal Model Based on Crack Interactions," *Journal of Engineering Mechanics*, Vol. 120, No. 7, pp. 1521–1542.

Jones, R., 1975, *Mechanics of Composite Materials*, Hemisphere Publishing Co., New York.

Joshi, S. and Sun, C., 1987, "Impact-induced fracture in a quasi-isotropic laminate," *Journal of Composite Technology and Research*, Vol. 9, No. 2, pp. 40–46.

Jurf, R. and Pipes, R., 1983, "Interlaminar fracture of composite materials," *Journal of Composite Materials*, Vol. 16, pp. 6260–70.

Kachanov, L., 1958, "On creep rupture time," *Izv. Acad. Nauk SSSR, Otd. Techn. Nauk*, Vol. 8, pp. 26–31.

Kachanov, L., 1986, *Introduction to continuum damage mechanics*, Martinus Nijhoff Publishers, Dordrecht, The Netherlands.

Kamel, A., Worswick, M., and Nandlall, D., 1998, "Effect of nonlocal damage treatment on dynamic fracture predictions," in: *ASME Pressure Vessels and Piping Conference, Structures Under Extreme Loading Conditions*, San Diego, CA, USA, pp. 195–201.

Kestin, J., 1992, "Local-Equilibrium Formalism Applied to Mechanics of Solids," *International Journal of Solids and Structures*, Vol. 29, pp. 1827–36.

Kim, C., 1991, "Finite element modelling of 2-D delamination growth in laminated composite plates," in: *Proceedings of the American Society for Composites, Sixth Technical Conference*, pp. 105–14.

Kim, R. and Soni, S., 1984, "Experimental and analytical studies on the onset of delamination in laminated composites," *Journal of Composite Materials*, Vol. 18,

pp. 70–80.

Kim, R. and Soni, S., 1986, "Delamination of composite laminates stimulated by interlaminar shear," *ASTM-STP*, Vol. 893, pp. 286–307.

Krajcinovic, D., 1983, "Constitutive equation for damaging materials," *Journal of Applied Mechanics*, Vol. 50, pp. 355–60.

Krajcinovic, D., 1996, *Damage Mechanics*, Vol. 41 of *Applied Mathematics and Mechanics*, Elsevier, Amsterdam, The Netherlands.

Krajcinovic, D. and Lemaitre, J., 1987, *Continuum Damage Mechanics, Theory and Applications*, Springer-Verlag, Wien, Austria.

Ladevèze, P. and Le Dantec, E., 1992, "Damage modelling of the elementary ply for laminated composites," *Composites Science and Technology*, Vol. 43, No. 3, pp. 257–67.

Lagace, P., 1993, "Delamination: From initiation to final failure," in: *Proceedings of the 9th International Conference on Composite Materials*, pp. 120–2.

Lagace, P. and Bhat, N., 1993, "On the prediction of delamination initiation," in: *Advanced Composites '93, International Conference on Advanced Composite Materials*, eds. T. Chandra and A. Dhingra, The Minerals and Materials Society, pp. 335–41.

Lammerant, L. and Verpoest, I., 1996, "Modelling of the Interaction between Matrix Cracks and Delaminations during Impact of Composite Plates," *Composites Science and Technology*, Vol. 56, pp. 1171–1178.

Langlie, S. and Cheng, W., 1989, "Numerical Simulation of High Velocity Impact on Fibre-Reinforced Composites," in: *ASME Pressure Vessels and Piping Conference*, Honolulu, HI, USA, pp. 51–64.

Lee, B., Song, J., and Ward, J., 1994, "Failure of Spectra Polyethylene fiber-reinforced composites under ballistic impact loading," *Journal of Composite Mate-*

rials, Vol. 28, No. 13, pp. 1202–1226.

Lee, S.-W. and Sun, C., 1993, "Dynamic Penetration of Graphite/Epoxy Laminates Impacted by a Blunt-Ended Projectile," *Composites Science and Technology*, Vol. 49, pp. 369–380.

Lemaitre, J., 1985, "A continuous damage mechanics model for ductile fracture," *Journal of Engineering Materials and Technology*, Vol. 107, pp. 83–87.

Lemaitre, J., 1992, *A Course on Damage Mechanics*, Springer-Verlag, Berlin, Germany.

Lin, H. and Lee, Y., 1990, "Impact-induced fracture in laminated plates and shells," *Journal of Composite Materials*, Vol. 24, pp. 1179–1199.

Lin, L. and Bhatnagar, A., 1992, "Ballistic Energy Absorption of Composites - III," in: *24th International SAMPE Technical Conference*, pp. T291–T306.

Liu, S., 1993, "Delamination and matrix cracking of cross-ply laminates due to a spherical indenter," *Composite Structures*, Vol. 25, pp. 257–265.

LS-DYNA3D, 1997, *LS-DYNA USERS'S MANUAL (Nonlinear Dynamic Analysis of Structures in Three Dimensions), Version 940*, Livermore Software Technology Corporation.

Lu, X. and Liu, D., 1991, "Finite element analysis of strain energy release rate at delamination rate at delamination front," *Journal of Reinforced Plastics and Composites*, Vol. 10, No. 3, pp. 279–29.

Lubliner, J., 1972, "On the thermodynamic foundations of nonlinear solids mechanics," *International Journal of Non-Linear Mechanics*, Vol. 7, pp. 237–54.

Lubliner, J., 1990, *Plasticity Theory*, Macmillan, New York, USA.

Majeed, O., 1995, "Numerical modelling of transverse impact on composite coupons," M.S. Thesis, Carleton University, Ottawa, On., Canada.

Majeed, O., Worswick, M., Straznicky, P., and Poon, C., 1994, "Numerical mod-

elling of transverse impact on composite coupons," *Canadian Aeronautics and Space Journal*, Vol. 40, No. 3, pp. 99–106.

Martin, R., 1996, "Interlaminar fracture characterization," *Key Engineering Materials*, Vol. 120-121, pp. 329–46.

Matzenmiller, A., Lubliner, J., and Taylor, R., 1995, "A constitutive model for anisotropic damage in fiber-composites," *Mechanics of Materials*, Vol. 20, pp. 125–52.

Maugin, G., 1992, *The Thermodynamics of Plasticity and Fracture*, Cambridge University Press, Cambridge, UK.

Nath, R. and Fenner, D., 1996, "Elasto-plastic finite element modelling of interfacial failure in model Kevlar 49 fibre-epoxy composites," *Composites: Part A*, Vol. 27A, pp. 821–832.

Needleman, A. and Tvergaard, V., 1994, "Mesh Effects in the Analysis of Dynamic Ductile Crack Growth," *Engineering Fracture Mechanics*, Vol. 47, No. 1, pp. 75–91.

O'Brien, T., 1982, "Characterization of delamination onset and growth in a composite laminate," *Damage in Composite Materials*, Vol. ASTM STP 775, pp. 140–67.

O'Brien, T. and Elber, W., 1993, "Delamination and Fatigue of Composite Materials: A Review," in: *Proceedings of the 9th International Conference on Composite Materials*, pp. 2.1–2.11.

O'Brien, T. and Martin, R., 1993, "Results of ASTM round robin testing for mode I interlaminar fracture toughness of composite materials," *Journal of Composites Technology and Research*, Vol. 15, No. 4, pp. 269–81.

Paul, P., Staff, C., Sanger, K., Mahler, M., Kan, H.-P., and Kautz, E., 1992, "Analysis and test techniques for composite structures subjected to out-of-plane loads," in: *Composite Materials: Testing and Design (Tenth Volume)*, ASTM, pp. 238–52.

Peijs, T., Smetts, E., and Govaert, L., 1994, "Strain rate and temperature effects on energy absorption of polyethylene and carbon fibres," *Advanced Composite Materials*, Vol. 1, No. 1, pp. 35–54.

Pijaudier-Cabot, G. and Bažant, Z., 1987, "Nonlocal Damage Theory," *Journal of Engineering Mechanics*, Vol. 113, No. 10, pp. 1512–1533.

Pijaudier-Cabot, G. and Bodé, L., 1995, "Arbitrary Lagrangian-Eulerian Finite Element Analysis of Strain Localization in Transient Problems," *International Journal for Numerical Methods in Engineering*, Vol. 38, pp. 4171–4191.

Pipes, R. and Pagano, N., 1970, "Interlaminar stresses in Composite Laminates under uniform axial extension," *Journal of Composite Materials*, Vol. 4, pp. 538–48.

Poon, C., Bellinger, N., Xiong, Y., and Gould, R., 1993, "Edge Delamination of Composite Laminates," in: *Proceedings of the 9th International Conference on Composite Materials*, pp. 12.1–12.13.

Poon, C., Komorowski, J., Gould, R., and Chapman, C., 1991, "Quantitative assessment of impact damage in composites," in: *Proceedings of the International Conference on Aircraft Damage Assessment and Design*, pp. 54–8.

Raju, I., Crews, Jr., J., and Aminpour, M., 1988, "Convergence of strain energy release rate components for edge-delaminated composite laminates," *Engineering Fracture Mechanics*, Vol. 30, pp. 383–96.

Rice, J., 1968, "A path independent integral and the approximate analysis of strain concentration by notches and cracks," *Journal of Applied Mechanics*, Vol. 35, pp. 379–86.

Robinson, P., Javidrad, F., and Hitchings, D., 1995, "Finite element modelling of delamination growth in the DCB and edge delaminated DCB specimens," *Composite Structures*, Vol. 32, No. 1, pp. 275–85.

Russell, A. and Street, K., 1984, "Factors affecting the interlaminar fracture energy

of graphite/epoxy laminates," in: *Proceedings of the 4th International Conference on Composite Materials*, pp. 279–86.

Rybicki, E. and Kanninen, M., 1977, "A Finite element calculation of stress intensity factors by a modified crack closure integral," *Engineering Fracture Mechanics*, Vol. 9, pp. 931–8.

Rybicki, E., Schmeuser, D., and Fox, J., 1977, "An energy release rate approach for stable crack growth in the free-edge delamination problem," *Journal of Composite Materials*, Vol. 11, pp. 470–87.

Salpekar, S. and O'Brien, T., 1991, "Analysis of matrix cracking and local delamination in $(0/\theta/-\theta)_s$ graphite epoxy laminates under tension load," in: *Proceedings of the Eight International Conference on Composite Materials*, pp. 28G1–28G14.

Schellekens, J. and de Borst, R., 1991, "Numerical simulation of free edge delamination in graphite epoxy specimen under axial extension," in: *Sixth International Conference on Conference Structures*, pp. 647–657.

Segal, C., 1991, "High-Performance Organic Fibers, Fabrics, and Composites for Soft and Hard Armor Applications," in: *23rd International SAMPE Technical Conference*, pp. 651–660.

Sela, N. and Ishai, O., 1989, "Interlaminar fracture toughness and toughening of laminated composite materials: A review," *Composites*, Vol. 20, No. 5, pp. 423–435.

Sih, G., 1981, "Cracks in Composite Materials," in: *Mechanics of Fracture*, eds. G. Sih and E. Chen, Martinus Nijhoff Publishers, The Hague, pp. xv–lxxxi.

Sjöblom, P., Hartness, J., and Cordell, T., 1988, "On low-velocity impact testing of composite materials," *Journal of Composite Materials*, Vol. 22, pp. 30–52.

Srinivasan, K., Jackson, W., and Hinkley, J., 1992, "Characterization of damage modes in impacted thermoset and thermoplastic composites," *Journal of Reinforced Plastics and Composites*, Vol. 11, No. 11, pp. 1111–26.

Starratt, D., Sanders, T., Cepuš, E., Poursartip, A., and Vaziri, R., 1998, "An Efficient Method for Continuous Measurement of Projectile Motion in Ballistic Impact Experiments," *International Journal for Impact Engineering*, Vol. submitted June 1998.

Straznicky, P., Poon, C., Worswick, M., Fuoss, E., Majeed, O., and Vietinghoff, H., 1995, "Damage resistance in composite materials," in: *Proceedings of the Tenth International Conference on Composite Materials*, pp. V 607–14.

Sun, C. and Jih, C., 1990, "Mechanics of delamination in composite laminates subjected to low velocity impact," *American Society of Mechanical Engineers ASME AMD*, Vol. 116, pp. 1–10.

Talreja, R., 1985, "A continuum damage characterization of damage in composite materials," *Proceedings of the Royal Society of London*, Vol. A 399, pp. 195–216.

Talreja, R., 1989, "A damage mechanics analysis of interlaminar cracking in composites," *Key Engineering Materials*, Vol. 37, pp. 21–34.

Talreja, R., ed., 1994, *Damage Evolution in Laminates*, Chap. 3: Basic Principles, by D.H. Allen, Elsevier Science B.V., Amsterdam, The Netherlands, pp. 1–51.

Tsamasphyros, G., 1989, "Path-independent integrals in anisotropic media," *International Journal of Fracture*, Vol. 40, pp. 203–19.

Tvergaard, V. and Needleman, A., 1995, "Effects of Nonlocal Damage in Porous Plastic Solids," *International Journal of Solids and Structures*, Vol. 32, No. 8/9, pp. 1063–1077.

van der Heiden, N. and van Bree, J., 1995, "Evaluation of the Behaviour of a Copper Liner for Indentation Response Analyses in Composite Helmets under FSP Impact," Tech. Rep. TNO-report PML 1994-A86, TNO Prins Maurits Laboratory, Rijswijk, The Netherlands.

Vietinghoff, H., 1993, "Compression-after-impact strength of carbon fibre rein-

forced plastic laminates," M.S. Thesis, Carleton University, Ottawa, On., Canada.

Vinson, J. and Walker, J., 1995, "Ballistic Impact into Composite Material Structures," in: *Proceedings of the 36th AIAA/ASME/ASCE/AHS/ASC Structures, Structural Dynamics, and Materials Conference*, New Orleans, LA, pp. 1924–1931.

Wang, A., 1980, "Initiation and growth of transverse cracks and edge delamination in composite laminates, Part 1 An energy method," *Journal of Composite Materials*, Vol. 14, pp. 71–87.

Wang, A., 1989, "Fracture analysis of interlaminar cracking," in: *Chapter 2 in Composite Materials Series 5, Interlaminar Response of Composite Materials*, ed. N. Pagano, Elsevier, Amsterdam, The Netherlands, pp. 69–109.

Wang, S., 1983, "Fracture mechanics for delamination problems in composite laminates," *Journal of Composite Materials*, Vol. 16, pp. 386–94.

Wang, S., Yau, J., and Corten, H., 1980, "A mixed-mode crack analysis of rectilinear anisotropic solids using conservative laws of elasticity," *International Journal of Fracture*, Vol. 16, pp. 247–59.

Wang, Y., Li, J., and Zhao, D., 1995, "Mechanical properties of fiber glass and Kevlar woven fabric reinforced composites," *Composites Engineering*, Vol. 5, No. 9, pp. 1159–1175.

Whitney, J., 1989, "Experimental characterization of delamination fracture," in: *Chapter 4 in Composite Materials Series 5, Interlaminar Response of Composite Materials*, ed. N. Pagano, Elsevier, Amsterdam, The Netherlands, pp. 161–250.

Whitney, J., Browning, C., and Hoogsteden, W., 1982, "A double cantilever beam test for characterizing mode I delamination of composite materials," *Journal of Reinforced Plastics and Composites*, Vol. 1, pp. 297–313.

Whitney, J. and Nuismer, R., 1974, "Stress fracture criteria for laminated composites containing stress concentrations," *Journal of Composite Materials*, Vol. 8,

pp. 253–65.

Williams, K. and Vaziri, R., 1995, "Finite element analysis of the impact response of CFRP composite plates," in: *Proceedings of ICCM-10*, Whistler, BC, Canada, pp. 647–54.

Wu, E. and Chang, L.-C., 1995, "Woven glass/epoxy laminates subject to projectile impact," *International Journal of Impact Engineering*, Vol. 16, No. 4, pp. 607–619.

Wu, E., Tsai, C.-Z., and Chen, Y.-C., 1994, "Penetration into glass/epoxy composite laminates," *Journal of Composite Materials*, Vol. 28, No. 18, pp. 1783–1802.

Young, R., Andrews, M., and Rallis, N., 1996, "Deformation micromechanics in high volume-fraction aramid/epoxy composites," *Composites: Part A*, Vol. 27A, pp. 889–894.

Zee, R. and Shieh, C., 1993, "Energy loss partitioning during ballistic impact of polymer composites," *Polymer Composites*, Vol. 14, No. 3, pp. 265–71.

Zhu, G., Goldsmith, W., and Dharan, C., 1992b, "Penetration of laminated Kevlar by projectiles - I. Experimental investigation," *International Journal of Solids and Structures*, Vol. 29, No. 4, pp. 399–420.

Zhu, G., Goldsmith, W., and Dharan, C., 1992a, "Penetration of laminated Kevlar by projectiles - II. Analytical model," *International Journal of Solids and Structures*, Vol. 29, No. 4, pp. 421–436.

Appendix A

TNO Series IMAX Images

A.1 1.1 g FSP

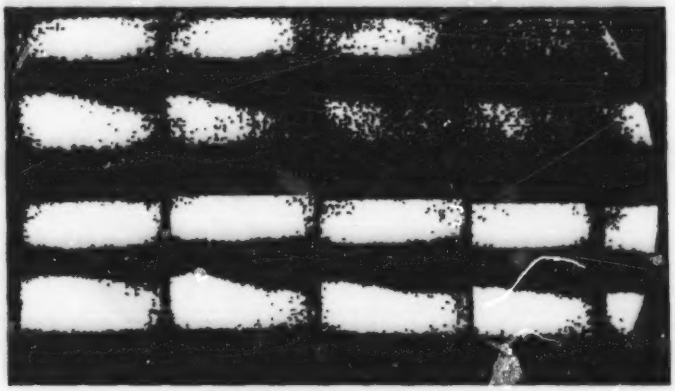

Figure A.1: IMAX image of a Kevlar panel impacted by a 1.1 g FSP at 560 m/s.

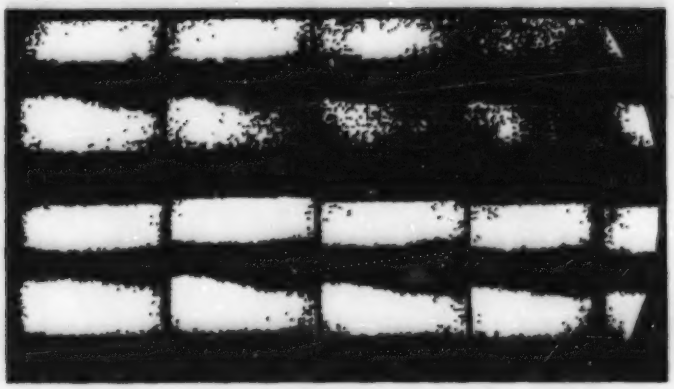

Figure A.2: IMAX image of a Kevlar panel impacted by a 1.1 g FSP at 545 m/s.

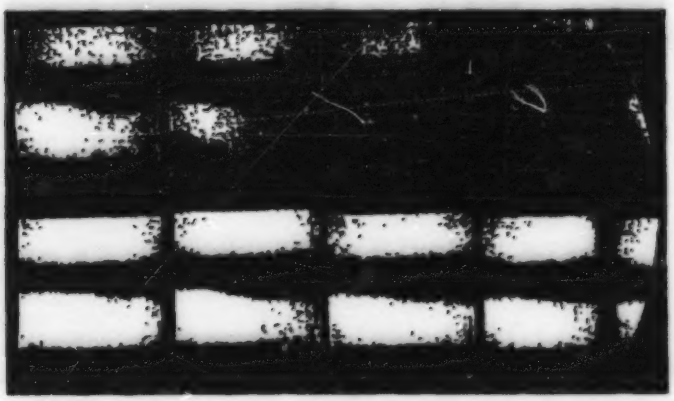

Figure A.3: IMAX image of a Kevlar panel impacted by a 1.1 g FSP at 4835 m/s.

A.2 2.8 g FSP

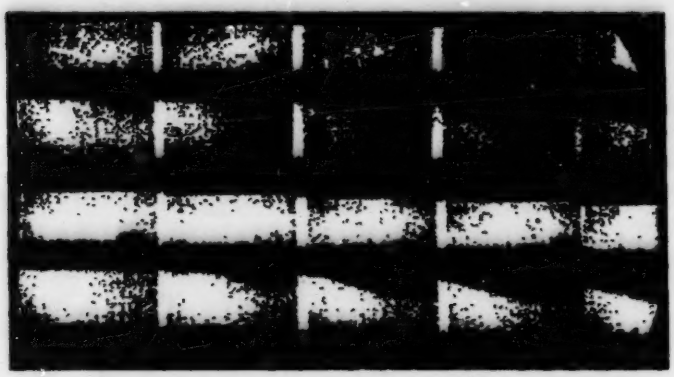

Figure A.4: IMAX image of a Kevlar panel impacted by a 2.8 g FSP at 461 m/s.

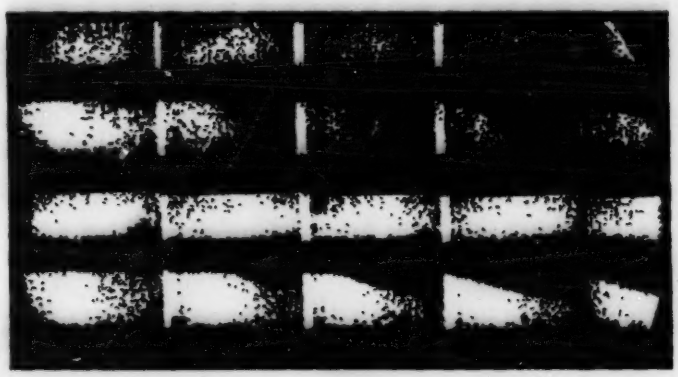

Figure A.5: IMAX image of a Kevlar panel impacted by a 2.8 g FSP at 446 m/s.

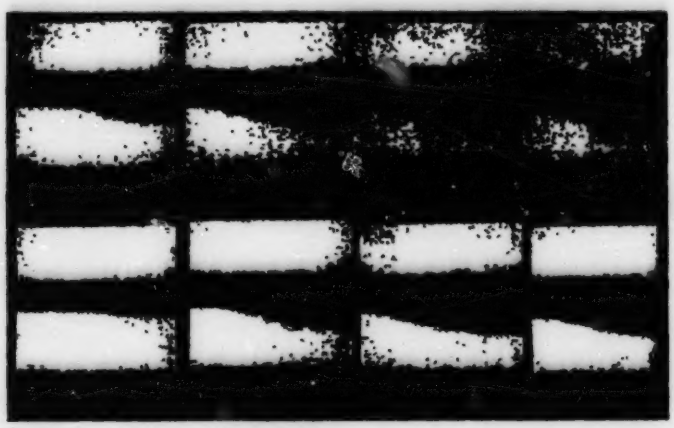

Figure A.6: IMAX image of a Kevlar panel impacted by a 2.8 g FSP at 398 m/s.

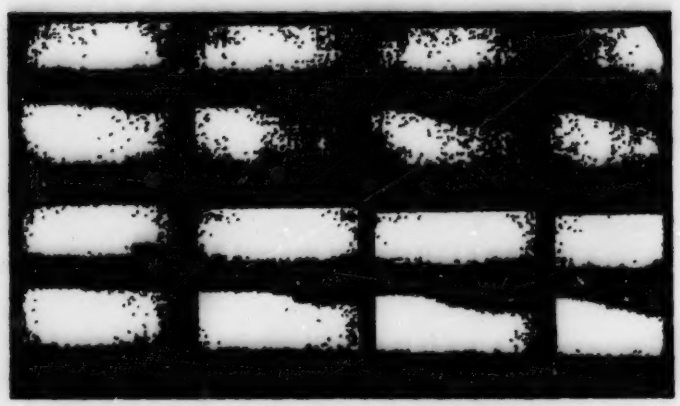

Figure A.7: IMAX image of a Kevlar panel impacted by a 2.8 g FSP at 386 m/s.

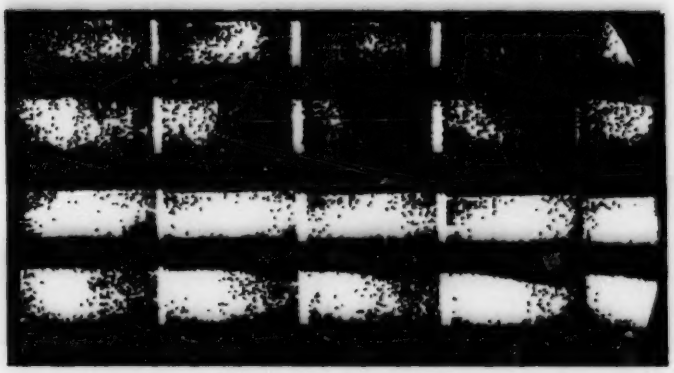

Figure A.8: IMAX image of a Kevlar panel impacted by a 2.8 g FSP at 321 m/s.

INTERNAL DISTRIBUTION

1 –Director General
1 – Deputy Director General
1 – Chief Scientist
1 – Head, Weapon Effects Section
6 – Document Library
1 – Dr. K. Williams
1 – Dr. D. Nandlall
1 – Dr. G. McIntosh
1 – Mr. M. Szymczak
1 – Mr. G. Pageau
1 – Mr. Y. Baillargeon
1 – Mr. J. Tremblay

EXTERNAL DISTRIBUTION

1 – DRDCIM
1 – DRDCIM (unbound copy)

1 – DRDB

1 – DSAL
1 – DSAL 2

1 – DCIEM
Attn: Dr. Frim

1 – DLR 5

1 – DSSPM 8

1 – DRES
Attn: Dr. Chris Weickert

1 – National Library of Canada
1 – CISTI
1 – DTIC

1 – DERA Fort Halstead
Mechanical Sciences Sector
Structural Materials Centre
Sevenoaks
Kent TN14 7BP
United Kingdom
Attn: Prof. M.J. Hinton

1 – DSTO
Terminal Effects
Weapon Systems Division
PO Box 1500
Salisbury 5108
SA, Australia
Attn: Dr. Alexander Krstic

1 – DGA
Centre d'Etudes du Bouchet - BP 3
91710 vert-le-Petit
France
Attn: Mr. J. P. Caillou

DOCUMENT CONTROL DATA

1 ORIGINATOR (name and address)
J van Hoof, M.J Worswick, and P V. Straznicky
Department of Mechanical and Aerospace Engineering
Carleton University
Ottawa, Ontario

2 SECURITY CLASSIFICATION
(Including special warning terms if applicable)
UNCLASSIFIED

3 TITLE (Its classification should be indicated by the appropriate abbreviation (S, C, R or U)
Simulation of the Backplane Response of Composite Helmet Materials Under Ballistic Impact – Final Report

4. AUTHORS (Last name, first name, middle initial. If military, show rank, e.g. Doe, Maj John E.)
van Hoof, J., Worswick, M J , and Straznicky, P.V.

5. DATE OF PUBLICATION (month and year)	6a NO. OF PAGES	6b. NO. OF REFERENCES
October, 1999	199	142

7 DESCRIPTIVE NOTES (the category of the document, e.g technical report, technical note or memorandum. Give the inclusive dates when a specific reporting period is covered.)
Contract Final Report

8. SPONSORING ACTIVITY (name and address)
DRDB

9a. PROJECT OR GRANT NO. (Please specify whether project or grant)	9b. CONTRACT NO.
Work Unit 2cb15	W7701-5-1203/01-XSK

10a. ORIGINATOR'S DOCUMENT NUMBER	10b OTHER DOCUMENT NOS
	N/A

11 DOCUMENT AVAILABILITY (any limitations on further dissemination of the document, other than those imposed by security classification)

- [x] Unlimited distribution
- [ ] Contractors in approved countries (specify)
- [ ] Canadian contractors (with need-to-know)
- [ ] Government (with need-to-know)
- [ ] Defense departments
- [ ] Other (please specify)

12. DOCUMENT ANNOUNCEMENT (any limitation to the bibliographic announcement of this document. This will normally correspond to the Document Availability (11). However, where further distribution (beyond the audience specified in 11) is possible, a wider announcement audience may be selected)
Same as 11

13. ABSTRACT (a brief and factual summary of the document. It may also appear elsewhere in the body of the document itself. It is highly desirable that the abstract of classified documents be unclassified. Each paragraph of the abstract shall begin with an indication of the security classification of the information in the paragraph (unless the document itself is unclassified) represented as (S), (C), (R), or (U). It is not necessary to include here abstracts in both official languages unless the text is bilingual)

Even though delamination is generally acknowledged as one of the main damage mechanisms in ballistically impacted laminates, information on the evolution of delaminations under ballistic conditions is scarce. The research presented in this report focuses on the deformation response of materials used in ballistic helmets, for which the impact of the delamination backplane with the head is considered to be a possible cause of skull fracture and underlying brain damage.

A numerical model was developed as part of this research to gain insight into the parameters governing the penetration and deformation response of laminated composites subjected to ballistic impact. The effects of the various model parameters on the predicted ballistic response were evaluated extensively. Both instantaneous and post-failure approaches were used. It was found that the use of a post-failure approach led to a more realistic and numerically more stable response than when an instantaneous failure model was used. The through-thickness shear properties used in the numerical model were found to have a large effect on the predicted ballistic response.

A number of ballistic impact tests on woven laminated Kevlar-29 composites panels were performed to evaluate the accuracy and limitations of the numerical model. Different types of projectiles with a range of impact velocities were used. The initial quasi-static material properties for the numerical model, obtained from the literature, were "calibrated" for one specific impact condition to obtain close agreement between simulations and measurements. The "calibrated" numerical material properties were then held constant in simulations of the other ballistic impact tests.

For the panels impacted by the four types of projectiles considered in this study, the model predicted the measured maximum backplane displacement accurately. Comparing the measured and predicted responses for all projectiles used in this study, it was found that the maximum backplane displacement increased nearly linearly with increased impact energy, at least within the range of impact energies used in this research.

14. KEYWORDS, DESCRIPTORS or IDENTIFIERS (technically meaningful terms or short phrases that characterize a document and could be helpful in cataloguing the document. They should be selected so that no security classification is required. Identifiers, such as equipment model designation, trade name, military project code name, geographic location may also be included. If possible keywords should be selected from a published thesaurus, e.g. Thesaurus of Engineering and Scientific Terms (TEST) and that thesaurus-identified. If it is not possible to select indexing terms which are Unclassified, the classification of each should be indicated as with the title.)

Numerical Simulation
Finite Element
Hydrocode Simulation
LS-DYNA3D
Helmet
Kevlar
Backplane Deformation
Ballistic Response

514326